Student Research Accomplishments 2004 – 2005

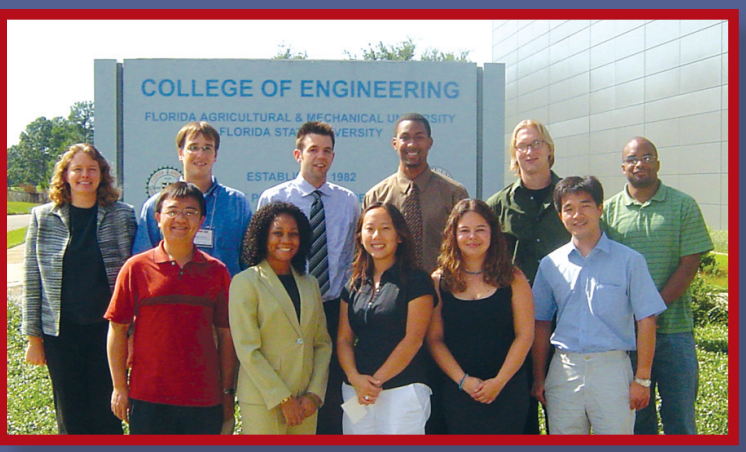

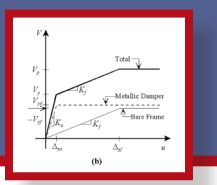

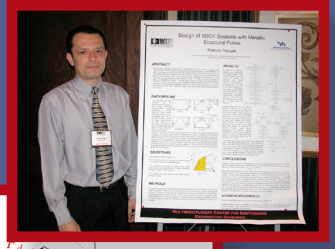

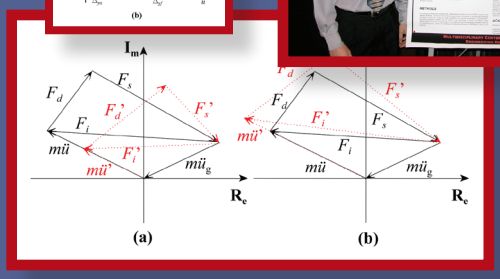

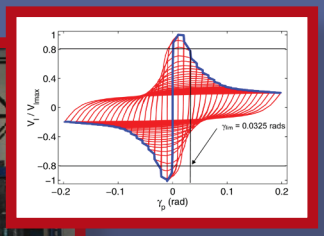

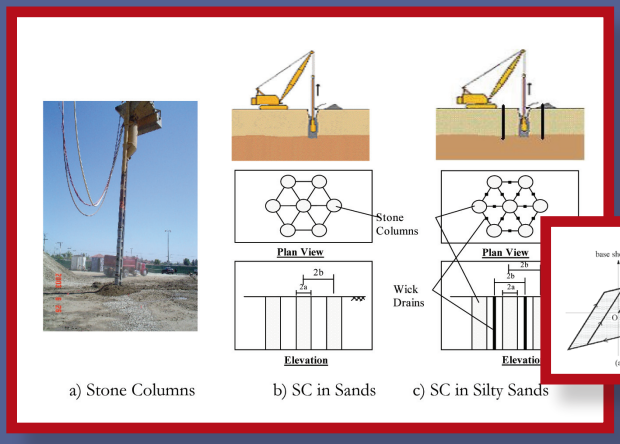

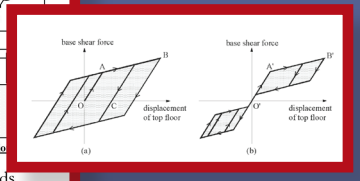

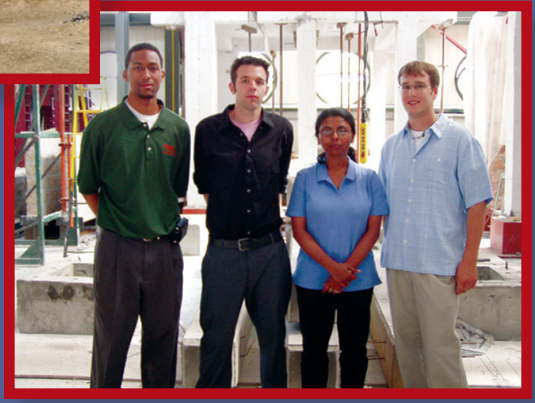

MCEER
MULTIDISCIPLINARY CENTER FOR EARTHQUAKE ENGINEERING RESEARCH
A National Center of Excellence in Advanced Technology Applications

May 2006

The Multidisciplinary Center for Earthquake Engineering Research

The Multidisciplinary Center for Earthquake Engineering Research (MCEER) is a national center of excellence in advanced technology applications that is dedicated to the reduction of earthquake losses nationwide. Headquartered at the University at Buffalo, State University of New York, the Center was originally established by the National Science Foundation (NSF) in 1986, as the National Center for Earthquake Engineering Research (NCEER).

Comprising a consortium of researchers from numerous disciplines and institutions throughout the United States, the Center's mission is to reduce earthquake losses through research and the application of advanced technologies that improve engineering, pre-earthquake planning and post-earthquake recovery strategies. Toward this end, the Center coordinates a nationwide program of multidisciplinary team research, education and outreach activities.

Funded principally by NSF, the State of New York and the Federal Highway Administration (FHWA), the Center derives additional support from the Federal Emergency Management Agency (FEMA), other state governments, academic institutions, foreign governments and private industry.

Student Research Accomplishments

2004-2005

Multidisciplinary Center for Earthquake Engineering Research
University at Buffalo, State University of New York

Edited by Navid Haji Allahverdi Pur

May 2006

MCEER-06-SP04

Red Jacket Quadrangle, Buffalo, New York 14261
Phone: (716) 645-3391; Fax: (716) 645-3399
E-mail: *mceer@mceermail.buffalo.edu*
World Wide Web: *http://mceer.buffalo.edu*

Foreword

The Student Leadership Council (SLC) is a formal incarnation of the students who are involved in performing MCEER research under a faculty advisor. Since its inception, MCEER has included and encouraged student efforts throughout its research program and in all of the disciplinary specialties concerned with earthquake engineering.

Throughout the years, students have been an integral component in advancing research in earthquake hazard mitigation. Many former students are now employed in academia, professional practice or government agencies, applying knowledge gained during their exposure to MCEER research. While associated with MCEER, students participate in Center annual meetings, attend conferences, workshops and seminars, and have the opportunity to make presentations at these events. The SLC was formed in the year 2000 to formalize these programs and to afford students from many different institutions the opportunity to meet with each other and develop/improve interaction.

The idea for the *Student Research Accomplishments* was conceived by the SLC and features the work of MCEER's current students. Topics range from traditional civil and lifeline engineering to applications of advanced technologies to social impacts and economic modeling.

This volume was coordinated and edited by Navid Haji Allahverdi Pur, Ph.D. Candidate, New Jersey Institute of Technology. Previous editors were Amanda Bonneau, from Cornell University, Ramiro Vargas, Benedikt Halldorsson, and Diego Lopez Garcia, all from the Department of Civil, Structural and Environmental Engineering, University at Buffalo, and Gauri Guha, Department of Energy, Environmental and Mineral Economics, the Pennsylvania State University.

All papers included in this volume were entered into MCEER's *Best Student Article Competition*. Members of MCEER's Industry Advisory Board (IAB) and other faculty judged the 10 submissions, and selected a winner and two honorable mentions. The winner of this year's competition is Ramiro Vargas, University at Buffalo, and honorable mentions were awarded to T. Shenthan and Dong Wang, both also from the University at Buffalo, for their outstanding efforts. The winner of the Best Paper Award was invited to present his research at the 2006 MCEER Annual Meeting. Our thanks go to Steve Eder, Facility Risk Consultants, Inc., Andy Taylor, KPFF Consulting Engineers, Doug Taylor, Taylor Devices, Inc., Walterio Lopez, Rutherford and Chekene, and Ali Porbaha, California State University, for their reviews and recommendations.

Finally, MCEER wishes to extend its thanks to the Student Leadership Council for its endeavors, and in particular to Michael Pollino, current president, and Jeffrey Berman, and A. Natali Sigaher, past presidents, for their able guidance of the SLC.

Best Student Article Competition: 2005

Winner

Ramiro Vargas

Ph.D. Student, Department of Civil, Structural & Environmental Engineering, University at Buffalo
Research Supervisor: Michel Bruneau, Professor and Director of MCEER

Seismic Response of Hybrid Systems with Metallic and Viscous Dampers page 1

Honorable Mentions

Thevachandran Shenthan

Ph.D. Student, Department of Civil, Structural & Environmental Engineering, University at Buffalo
Research Supervisor: Sabanayagam Thevanayagam, Associate Professor and MCEER Director of Education

Soil Densification Using Vibro-Stone Columns Supplemented with Wick Drains page 9

Dong Wang

Ph.D. Student, Department of Civil, Structural & Environmental Engineering, University at Buffalo
Research Supervisor: Andre Filiatrault, Professor and Deputy Director of MCEER

Seismic Response of Steel Framed Hospital Buildings with Self-Centering Systems page 17

Contents

1

Seismic Response of Hybrid Systems with Metallic and Viscous Dampers

Ramiro E. Vargas

Graduate Student, Department of Civil, Structural and Environmental Engineering, University at Buffalo

Research Supervisor: Michel Bruneau, Professor and MCEER Director

Summary

Metallic dampers can enhance structural performance by reducing seismically induced lateral displacements, and by reducing inelastic behavior of beams and columns. Limiting story drift also indirectly allows for mitigation of damage to nonstructural components that are sensitive to lateral deformations. However, many nonstructural elements and components are vulnerable to excessive accelerations. Therefore, in order to protect these components, floor accelerations in buildings should be kept below certain limits. In this perspective, this paper investigates the seismic performance of single-degree-of-freedom (SDOF) systems with metallic and viscous dampers installed in parallel, to determine the effectiveness or appropriateness of using metallic dampers to mitigate lateral displacements, simultaneously with viscous dampers to reduce acceleration demands. Parametric analyses investigate the effectiveness of adding various levels of viscous damping on the equivalent hysteretic damping and on the spectral floor acceleration for short, intermediate, and long period structures.

Introduction

Metallic dampers (a.k.a. hysteretic dampers), especially designed to behave as passive energy dissipation (PED) devices, have been thoroughly studied in the past to enhance structural performance by reducing seismically induced structural damage. In this sense, metallic dampers have been implemented primarily in flexible framing systems (e.g., moment frames) to reduce interstory drifts, and eliminate (or at least reduce) inelastic behavior in beams and columns (Bruneau et al., 1998). Limiting story drift allows mitigation of damage to nonstructural components that are sensitive to lateral deformations (i.e., elements that are generally attached to consecutive floors). However, many nonstructural elements and equipment are attached to a single floor, and can lose their functionality due to excessive sliding, overturning, or damage to their internal components due to severe floor vibrations.

Although metallic dampers have been shown to be effective in reducing interstory drifts, some studies have found that, in many cases, the use of metallic dampers may cause increases in floor accelerations due to the added stiffness, which may negatively affect seismic behavior of nonstructural components (e.g., Iwata, 2004; Mayes et al., 2004; Tong et al., 2004, to name a few). This suggests that it may be desirable to use metallic dampers to mitigate lateral displacements, along with viscous dampers to reduce acceleration demands. In this perspective, this paper investigates

the seismic performance of single-degree-of-freedom (SDOF) systems with metallic and viscous dampers installed in parallel.

Equivalent Viscous Damping (Hysteretic Damping)

In many structural analyses such as the Nonlinear Static Procedure (FEMA 356), the dynamic characteristics of a structure having metallic dampers are transformed to an effective period, T_{eff}, which is obtained from the secant or effective stiffness, K_{eff}, of the combined system (i.e., bare frame plus dampers) to the point of maximum displacement as illustrated in Figure 1a, and an equivalent viscous damping (a.k.a. hysteretic damping), ξ_h, also determined from specific hysteresis loops at the point of maximum displacement. Generally, the hysteretic damping for a metallic damper is obtained by setting the area within a hysteresis loop equal to the area within a viscous damper cycle, provided that the area contained within one cycle of motion is the energy dissipated per cycle (Hanson and Soong, 2001).

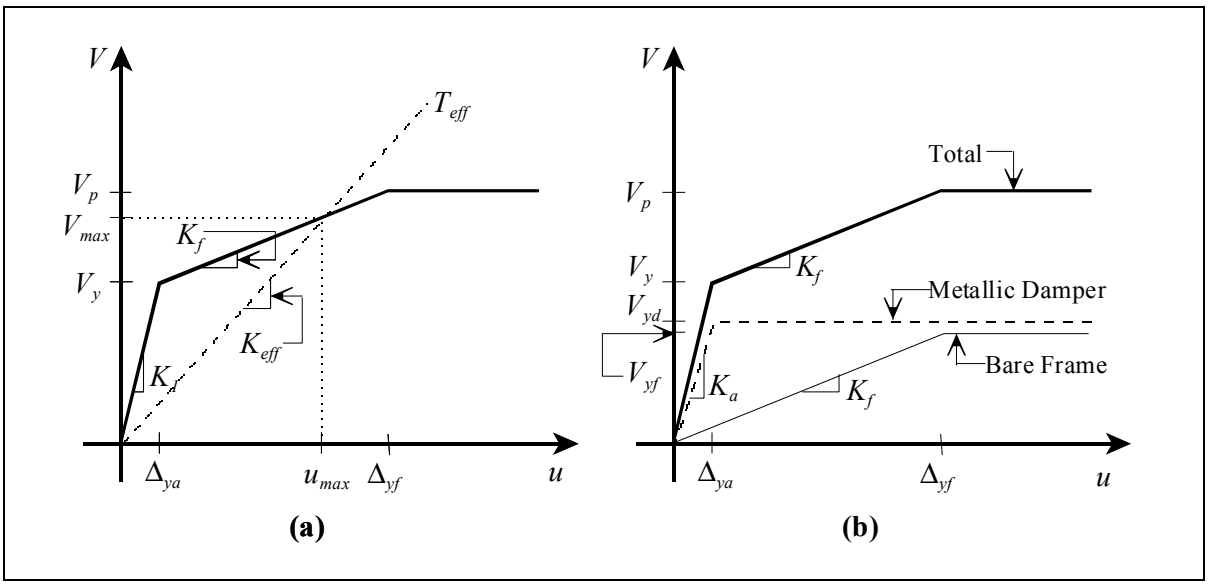

Figure 1. General pushover curve: (a) Effective stiffness and period; (b) Bare frame and metallic damper contribution to the total base shear capacity

The set of parameters used in this study are obtained from Figure 1b: the stiffness ratio, α, the maximum displacement ductility, μ_{max}, and the strength-ratio, η. The stiffness ratio, α, is the relation between the frame stiffness, K_f, and the total initial stiffness, K_1 which can be calculated as:

$$\alpha = \frac{1}{1 + K_a / K_f} < 1.0 \qquad (1)$$

The maximum displacement ductility is the maximum displacement ductility that the structure experiences before the frame undergoes inelastic deformations. This parameter can be written as:

$$\mu_{\max} = \frac{\Delta_{yf}}{\Delta_{ya}} > 1.0 \tag{2}$$

where Δ_{ya} and Δ_{yf} are the yield displacement of the metallic dampers, and the yield displacement of the frame, respectively. The strength-ratio, η, is determined as the relation between the yield strength, V_y, and the maximum ground force applied during the motion, defined as:

$$\eta = \frac{V_y}{m\ddot{u}_{g\max}} \tag{3}$$

where m is the system mass and $\ddot{u}_{g\max}$ is the peak ground acceleration. Consequently, the hysteretic damping, ξ_h, may be determined from the following expression, adapted from Ramirez et al. (2000):

$$\xi_h = \left(\frac{2}{\pi}\right)\left[\frac{\left(1-1/\mu_f\right)+\dfrac{(1-\alpha)}{\alpha\mu_{\max}}\left(1-1/\mu\right)}{1+\dfrac{(1-\alpha)}{\alpha\mu_{\max}}}\right] \geq 0 \tag{4}$$

where μ and μ_f are the global and frame ductility determined as u_{max} / Δ_{ya} and u_{max} / Δ_{yf}, respectively (see Figure 1b), and u_{max} is the system maximum lateral displacement. Note that for $\mu < 0$ (and therefore, $\mu_f < 0$), the system remains elastic, which translates into no dissipation of energy through hysteretic behavior and, therefore, no hysteretic damping is developed (i.e., $\xi_h = 0$).

Hysteretic Response

As previously mentioned, the main purpose of this paper is to investigate whether using viscous fluid dampers in parallel with metallic dampers can simultaneously reduce lateral displacements and floor accelerations. Although lateral displacement always decreases when using metallic, viscous, or both kinds of dampers acting together, it was found that floor acceleration increases in most of the considered cases, even for systems designed with large viscous damping (Vargas and Bruneau, 2005). This section focuses on studying the hysteretic response of short, intermediate, and long period systems, using the lowest and highest values of η from the set of analyses (i.e., $\eta = 0.2$ and $\eta = 1.0$), along with several levels of viscous damping (i.e., 5%, 10%, 20%, and 30%), to understand the reason for these observed increases in acceleration.

Using d'Alembert's principle, it is possible to express the equation of motion of a SDOF system as an equation of dynamic equilibrium (Clough and Penzien, 1993). Therefore, for a SDOF subjected to ground excitation, the equation of motion may be written as:

$$F_i + F_d + F_s = 0 \tag{5}$$

where F_i is the inertial force, calculated as:

$$F_i = m\left(\ddot{u}_g + \ddot{u}\right) \tag{6}$$

where $\ddot{u}_g$ and $\ddot{u}$ are the ground acceleration, and the relative floor acceleration, respectively, F_d is the viscous damper force, and F_s is the sum of the metallic damper force and the structural frame force, called here the hysteretic force, determined according to the following expression:

$$F_s = \begin{cases} K_1 u \ , & u < \Delta_{ya} \\ V_y + \alpha K_1 (u - \Delta_{ya}) \ , & \Delta_{ya} \le u < \Delta_{yf} \\ V_p \ , & \Delta_{ya} \le u \end{cases} \tag{7}$$

where all variables are defined in Figure 1. Note that for undamped systems (i.e., $F_d = 0$), the inertial and hysteretic forces must be equal and opposite to satisfy the dynamic equilibrium of Equation (5). In damped systems, increases in viscous damping result in decreases in the lateral displacement, u, and therefore, decreases in the hysteretic force, F_s, according to Equation (7) (assuming that the system is designed such that $u < \Delta_{yf}$, which is required to prevent any inelastic behavior of the frame). Consequently, acceleration demand, $\ddot{u}$, may increase (or decrease) to satisfy dynamic equilibrium. The resultant increase or decrease in the inertial force depends on the increase in F_d value relative to the decrease in the value of F_s. For instance, if $\Delta F_d > |\Delta F_s|$ then $\Delta\ddot{u} > 0$ (i.e., acceleration increases), and if $\Delta F_d < |\Delta F_s|$ then $\Delta\ddot{u} < 0$ (i.e., acceleration decreases).

Figure 2 shows some examples of the superposed hysteresis loops for the inertial force and hysteretic force normalized with respect to the yield point (V_y, Δ_{ya}). The difference between the curves is equal to the viscous damper force, F_d. Note that when the maximum displacement is reached (i.e., $\dot{u} = 0$) the values of both curves coincide (i.e., $| F_i | = | F_s |$). Maximum difference between the curves is obtained when $u = 0$ (i.e., maximum velocity), since the hysteretic force has its minimum value at this point. For elastic systems (i.e., $u < \Delta_{ya}$), when $u = 0$, $F_s = 0$, the inertial force and the damping force are equal (i.e., $| F_i | = | F_d |$).

Note that for systems that behave inelastically and for which the frame remains elastic (i.e., $\Delta_{ya} \le u < \Delta_{yf}$), the stiffness ratio, α, has a significant influence on the acceleration demand, since $F_s = V_y + \alpha K_1 (u - \Delta_{ya})$ in this region. Since $F_s \approx V_y$ in systems with small values of α, a reduction in the hysteretic force when viscous damping is added is not significant. On the other hand, F_s may be significantly reduced in systems with large values of α, when maximum displacement decreases by the addition of viscous damping. For example, in a system with $T = 0.5$ s, $\eta = 0.2$, $\alpha = 0.05$, $\mu_{max} = 10$ (Figure 2), the hysteretic force remains almost constant (i.e., $\Delta F_s \approx 0$), and the acceleration demand consequently increases by 62%, when 25% of extra viscous damping is added. For the same system, but with $\alpha = 0.50$ instead, F_s is reduced by 40% when 25% of viscous damping is added (i.e., $\Delta F_d < |\Delta F_s|$), and accordingly, the acceleration demand decreases by 26%.

Also, it may be noted in Figure 2 that for elastic systems (i.e., $F_s = K_1 u$), the displacement and acceleration demands both decrease by increasing the viscous damping, since the decrease in the hysteretic force is always larger than the increase in the viscous damper force (i.e., $\Delta F_d < |\Delta F_s|$). For example, in a system with $T = 1.50$ s, $\eta = 1.0$, $\alpha = 0.25$, $\mu_{max} = 2.5$, the hysteretic force reduces by 40% when 25% of viscous damping is added (i.e., $\Delta F_d < |\Delta F_s|$), and the acceleration demand accordingly decreases by 46%.

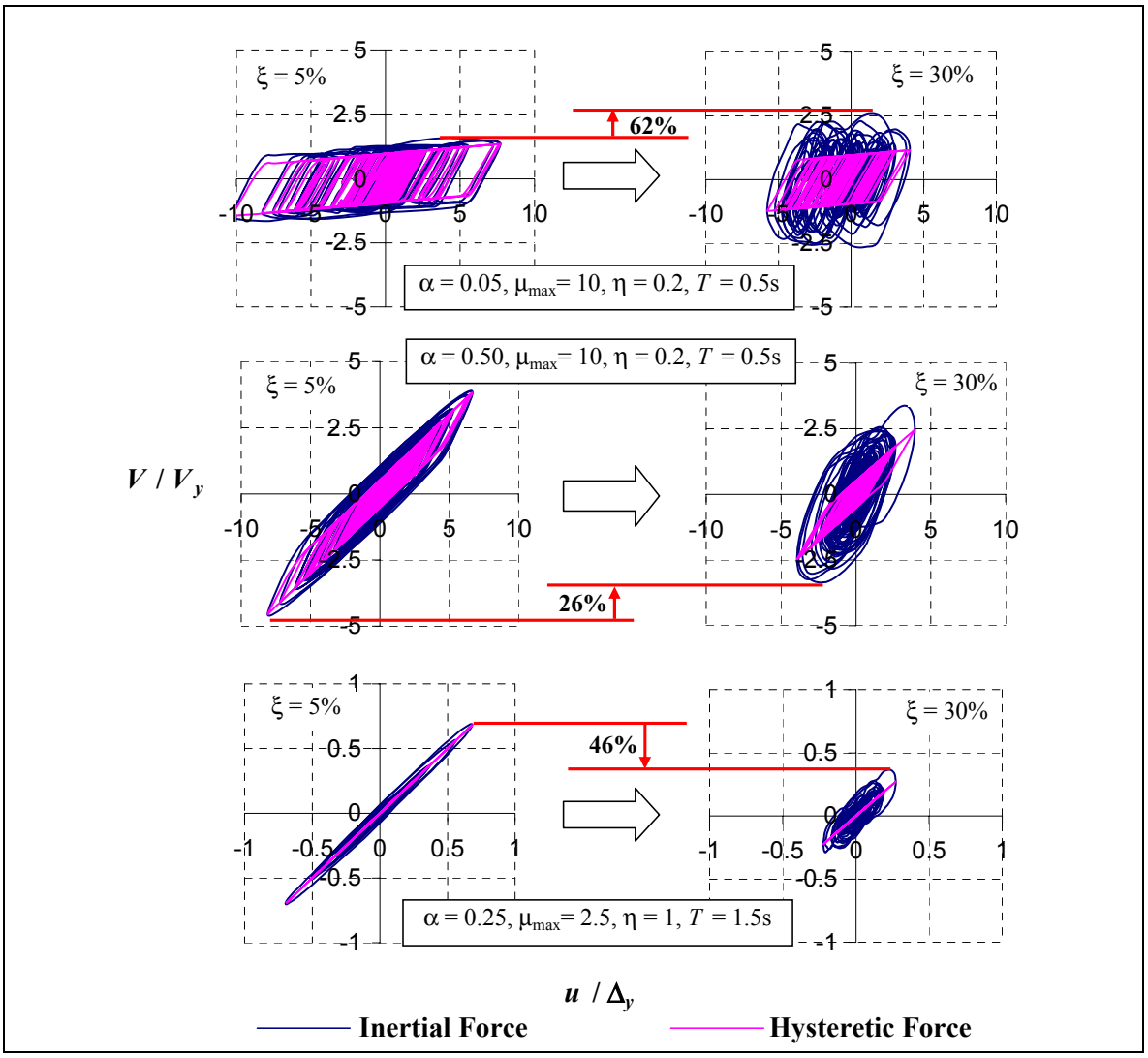

Figure 2. Normalized hysteresis loops for 5% and 30% of viscous damping

These results corroborate the fact that the addition of viscous damping is effective in reducing the displacements and acceleration demands of elastic or near-elastic (e.g., $\alpha = 0.5$) systems, but is ineffective (and in fact detrimental) for nonlinear systems. However, metallic dampers with elastic behavior are not effective, since they only provide additional stiffness to reduce lateral displacements, which is something that could be done just as well with conventional structural elements (Vargas and Bruneau, 2005).

Analysis in the Frequency Domain

Results from the previously studied systems were also analyzed in the frequency domain. Using the Fast Fourier Transform (FFT) algorithm (Cooley and Tukey, 1965), response of the systems studied parametrically here were transformed from the time domain to the frequency domain, in which inertial, viscous damper, and hysteretic forces can be represented as rotational vectors forming a closed polygon in the complex plane, as schematically shown in Figure 3 (a.k.a. Argand diagrams as

in Clough and Penzien, 1993). Figure 3a shows a representation of the equation of motion (Equation (5)) for a system with elastic behavior at a particular time during the earthquake time history. Note that increases in the viscous damper force result in substantial decreases in the hysteretic and in the inertial forces (shown as dotted lines). On the other hand, in systems with inelastic behavior (Figure 3b) an increase in the viscous damper force may result in a substantial increase in the inertial force along with a slight decrease in the hysteretic force (shown again as dotted lines).

Note that for small viscous damping (i.e., 5%), the inertial force and the hysteretic force are almost equal (see Figure 2). On the other hand, for systems with large viscous damping (i.e., 30%), the inertial force is considerably greater than the hysteretic force. This vectorial addition shows how a greater damping force can lead to the acceleration increases described in the previous section. Incidentally, this observation has been reported by some practitioners that have considered using viscous dampers to retrofit buildings in selective case studies, and have noticed increases in the floor accelerations if the structure remains inelastic after the retrofit but could not explain why (e.g., personal communication, Dr. Chris Tokas, Manager, California Hospital Seismic Retrofit Program, State of California Office of Statewide Health Planning and Development).

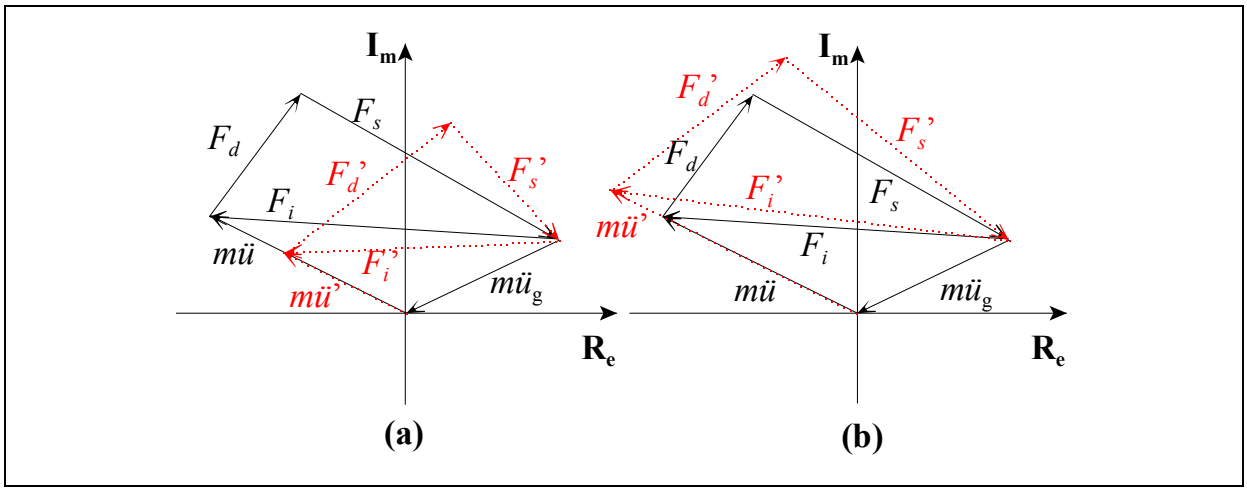

Figure 3. Schematic Representation of Inertial, Viscous Damper and Metallic Damper Forces: (a) Elastic Systems; (b) Inelastic Systems

Conclusions

Seismic response of hybrid systems having metallic and viscous dampers has been studied in this paper through parametric analyses. It was found that increases in viscous damping reduce the effectiveness of metallic dampers, since the amplitude of motion (and thus ductility demand) is reduced. In some cases, when the amplitude of motion decreases to the point where the system behaves elastically, metallic dampers only work to provide additional stiffness to the system, which may be achieved by other conventional methods (e.g., steel braces as apposed to special ductile devices).

Although viscous dampers are known to decrease both displacements and acceleration demands in structures with elastic behavior, for structural systems where metallic dampers are designed to behave inelastically (i.e., $\Delta_{ya} \leq u < \Delta_{yf}$), the floor accelerations are likely to increase if viscous

dampers are added in parallel to metallic dampers, especially for systems with small stiffness ratio (i.e., $\alpha < 0.25$). Adding such viscous dampers in parallel is therefore not only ineffective but detrimental to the seismic performance of acceleration sensitive equipment and nonstructural components. This observation would also be true for buildings that have been retrofitted with viscous dampers and whose original frame still behaves inelastically under major earthquakes. Argand diagrams in the frequency domain are successfully used to explain these observations.

Acknowledgements

This research was carried out under the supervision of Dr. Michel Bruneau, and supported by the National Science Foundation, under award number EEC-9701471 to the Multidisciplinary Center for Earthquake Engineering Research. This financial support is gratefully acknowledged.

References

Bruneau M, Uang CM, Whittaker A (1998): *Ductile Design of Steel Structures*. McGraw Hill, New York

Clough RW, Penzien J (1993): *Dynamics of Structures*. Second Edition. McGraw Hill, New York.

Cooley JW, Tukey JW (1965): An Algorithm for Machine Calculation of Complex Fourier Series. *Mathematics of Computation*, American Mathematical Society, Volume 9, No. 90, pp. 297-301.

Hanson RD, Soong TT (2001): Seismic Design with Supplemental Energy Dissipation Devices. *Monograph No. MNO-8*, Earthquake Engineering Research Institute, Oakland, California.

Iwata M (2004): Applications-Design of Buckling Restrained Braces in Japan. *13th World Conference on Earthquake Engineering*, Vancouver, Canada, 2004. Paper No.3208.

Mayes R, Goings C, Naguib W, Harris S, Lovejoy J, Fanucci J, Bystricky P, Hayes J (2004): Comparative Performance of Buckling-Restrained Braces and Moment Frames. *13th World Conference on Earthquake Engineering*, Vancouver, Canada, 2004. Paper No.2287.

Ramirez OM, Constantinou MC, Kircher CA, Whittaker AS, Johnson MW, Gomez JD, Chrysostomou CZ (2000): Development and Evaluation of Simplified Procedures for Analysis and Design of Buildings with Passive Energy Dissipation Systems. *Report No. MCEER-00-0010, Revision 1*, Multidisciplinary Center for Earthquake Engineering Research, University at Buffalo, State University of New York, Buffalo, NY.

Tokas C (2005): Personal Communication. Manager, California Hospital Seismic Retrofit Program, State of California Office of Statewide Health Planning and Development (OSHPD).

Tong M, Lee GC, Rzhevsky V, Qi J, Shinozuka M, Middleton J (2004): A Comparison of Seismic Risk of Non-structural Systems in a Hospital before and after a Major Structural Retrofit. *ATC-29-2 Seminar on Seismic Design, Retrofit, and Performance of Nonstructural Components in Critical Facilities*. Newport Beach, CA.

Vargas R, Bruneau M (2005): Investigation of the Structural Fuse Concept. *Draft Report*, Multidisciplinary Center for Earthquake Engineering Research, State University of New York at Buffalo.

2

Soil Densification Using Vibro-Stone Columns Supplemented with Wick Drains

Thevachandran Shenthan

Ph.D. Candidate, Department of Civil, Structural and Environmental Engineering, University at Buffalo

Research Supervisor: S. Thevanayagam, Associate Professor and MCEER Director of Education

Summary

Saturated loose sand and non-plastic silty sand deposits are often vulnerable to liquefaction during earthquakes. Sand deposits densified by vibro-stone column (SC) are more resistant to liquefaction, and have performed well during earthquakes. Silty sand deposits appear to perform well when improved by SC supplemented with wick drains. Wick drains aid dissipation of excess pore pressure induced during SC installation in low-permeable silty soils enhancing densification. This paper presents a numerical model to simulate, and to analyze soil densification during SC installation with and without wick drains. Design charts for SC are developed based on this work. These numerical results are compared with field test data. Design guidelines are presented based on these design charts.

Introduction

SC installation process involves a sequence of processes starting with insertion of a vibratory probe with rotating eccentric mass (FHWA 2001) (Figure 1) into the ground. Once the design depth is reached, the probe is withdrawn in lifts, backfilling the hole with gravel. During each lift the probe is then reinserted expanding the SC diameter. This process is repeated several times until a limiting condition, measured in terms of amperage drawn by the probe, is achieved. SC have been mainly designed for densification of relatively granular soils containing less than 15% non-plastic silt passing sieve #200 (74 μm) and less than 2% of clayey particles (<2 μm) (FHWA 2001). Soils containing excessive fines

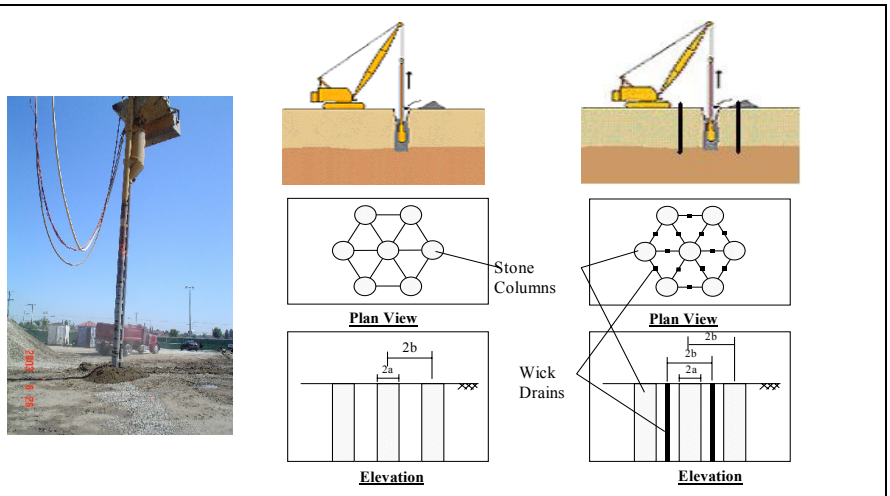

Figure 1. Vibro-stone columns (with or without wick drains)

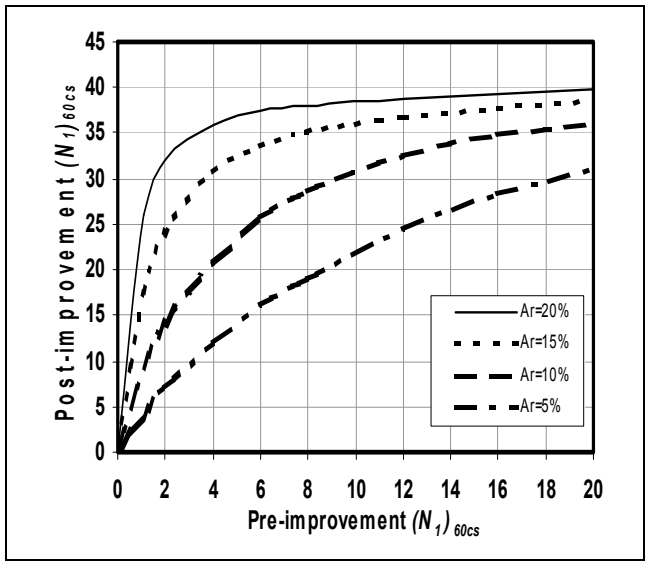

Figure 2. Pre- and post-improvement $(N_1)_{60cs}$

have been difficult to densify using SC. Current practice for design of SC for liquefaction mitigation relies on past experience, and field pilot tests. Based on pre- and post-improvement SPT and CPT data from case histories, Baez (1995) developed an empirical relationship between pre- and post-improvement equivalent clean sand SPT blow counts, $(N_1)_{60cs}$, for a set of area replacement ratios A_r of 5, 10, 15, and 20% (Figure 2) for fine to medium sand with fines less than 15% and little or no clay content. A_r is defined as the ratio of stone column area to the tributary area per stone column.

Recent case histories show that vibro-stone column technique may be effectively used to densify silty sands containing fines content exceeding 15% by using pre-installed supplementary wick drains. The supplementary drains help to relieve excess pore pressures developed during stone column installation processes (Andrews 1998, Luehring et al. 2001) and help soil densification.

For both cases, sands and silty soils, at present, there are no detailed analytical procedures available to determine the densification achievable or to analyze the effects of various field soil and SC construction parameters on the degree of improvement possible to achieve for a wide range of soils with non-plastic silt contents.

Recent work conducted by Thevanayagam and co-workers (2002, 2003) and Shenthan et al. (2004 a and b) focused on development of a simple analytical methodology to simulate soil response during SC installation, quantify soil densification in saturated sands and silty soils, and assess the effect of various construction/design choices and soil parameters on the degree of improvement achievable. Analytical results were compared with field test data. Based on this work, guidelines were developed for design of stone columns to mitigate liquefaction in silty soils. This paper presents a brief summary of these findings.

Simulation of Vibro-Stone Column

Densification of saturated loose sands and silty soils during SC installation is essentially a process involving controlled liquefaction, and consolidation of the soil leading to concurrent densification. Shenthan et al. (2004a and b) developed an analytical technique to simulate pore pressure developments in the soil due to vibratory energy imparted during installation and subsequent consolidation of the soil and densification based on the simplified methodology highlighted briefly in following sub-sections. Details are reported in Shenthan et al. (2004 a and b) and Shenthan (2005).

Dissipated Energy

Considering the energy source in the vibratory probe as a point-source and assuming that the energy propagates spherically outward, the energy loss per unit time per unit volume of soil at distance r can be approximated by,

$$w = W_0 \frac{\alpha}{2\pi r^2} Exp\left[-2\alpha\left(r - r_0\right)\right].Exp\left[-\beta\left(r_u\right)_{av}\right] \tag{1}$$

where r_0 is the radius of the probe, W_0 is the energy imparted by the probe into the soil per unit time ($= \eta_0 P_0$), P_0 is the power rating of the vibratory probe, η_0 is the probe efficiency, $(r_u)_{av}$ is the average excess pore pressure ratio within the soil surrounding the probe up to an effective radial distance r_e, which is assumed to be the same as the center to center spacing between stone columns in this study, α is the coefficient of attenuation (Richart et al. 1970, Dowding 1996), and β= a constant.

In the soil around the vibratory probe, as excess pore pressure develops due to vibration, the soil becomes weak. Since the amplitude of vibration of the probe is limited (FHWA 2001), the energy imparted to the surrounding soil would decrease, resulting in a reduced efficiency. When the pore pressures dissipate, and the soil is sufficiently densified, the energy transfer rate would increase. In this study, this phenomenon has been taken into account, considering the energy transfer rate to decay with increasing excess pore pressure, represented by the last exponential term in the above equation.

Pore pressure generation and dissipation

Based on experimental data and theoretical considerations, excess pore water pressure generated due to cyclic loading has been related to frictional energy loss in the soil by $r_u = 0.5\text{Log}_{10}[100(E_c/E_L)]$ (Thevanayagam et al. 2003), where r_u = pore pressure ratio u/σ_0', σ_0'= initial effective confining pressure, E_c = cumulative energy loss per unit volume of soil, E_L = energy per unit volume required to cause liquefaction, and $(E_c/E_L)>0.05$.

The governing equation for excess pore pressure dissipation in soil around the vibratory probe is:

$$\frac{\partial u}{\partial t} = \frac{k_h}{\gamma_w m_v}\left(\frac{\partial^2 u}{\partial r^2} + \frac{1}{r}\frac{\partial u}{\partial r} + \frac{1}{r^2}\frac{\partial^2 u}{\partial \theta^2}\right) + \frac{k_v}{\gamma_w m_v}\frac{\partial^2 u}{\partial z^2} + \frac{\partial u_g}{\partial t} \tag{2}$$

where k_h and k_v are the hydraulic conductivities of the soil in the horizontal and vertical directions, respectively; m_v is the volume compressibility of the soil; u is the excess pore water pressure at coordinates (r, θ, z); t is time; γ_w is the unit weight of water; r, z, and θ are radial, vertical, and angular coordinates, respectively; u_g is the excess pore pressure generated due to vibration of the soil during SC installation (or due to seismic excitation during an earthquake following installation of stone columns).

Design Charts

Numerical simulations were conducted for silty soils with three different pre-improvement $(N_1)_{60cs}$ (normalized clean sand equivalent SPT blow counts) of 7, 11 and 16. For each $(N_1)_{60cs}$, three different area replacement ratios (A_r = 5.6, 10, and 22.5%) were considered. For each case, simulations were done for stone column without wick drains, and with wick drains, respectively. The effect of fines

content is reflected by varying the hydraulic conductivity (k) from 10^{-4} to 10^{-8} m/s. It was assumed that the vibro-stone columns are installed at a triangular pattern with wick drains pre-installed at midpoints between stone column locations. The power rating of the vibratory probe was assumed to be 120 kW.

Figure 3 shows the simulation results for pre- and post- improvement $(N_1)_{60cs}$ for soils at a depth with effective vertical stress of 100 kPa and a range of k values. Results show that, at low area replacement ratio, the effect of supplementary wick drains is negligibly small and soil densification is primarily affected by stone columns. No significant additional densification is achieved by stone columns with wick drains compared to stone columns without wick drains in soils with hydraulic conductivities less than about 10^{-6} m/s. At high area replacement ratio of about 22.5%, wick drains significantly contribute to the drainage of excess pore pressures induced during stone column installation and soil densification. The combined system is effective for soils containing non-plastic silt and hydraulic conductivity as low as 10^{-8} m/s. However, the degree of improvement decreases with increasing silt content and decreasing hydraulic conductivity.

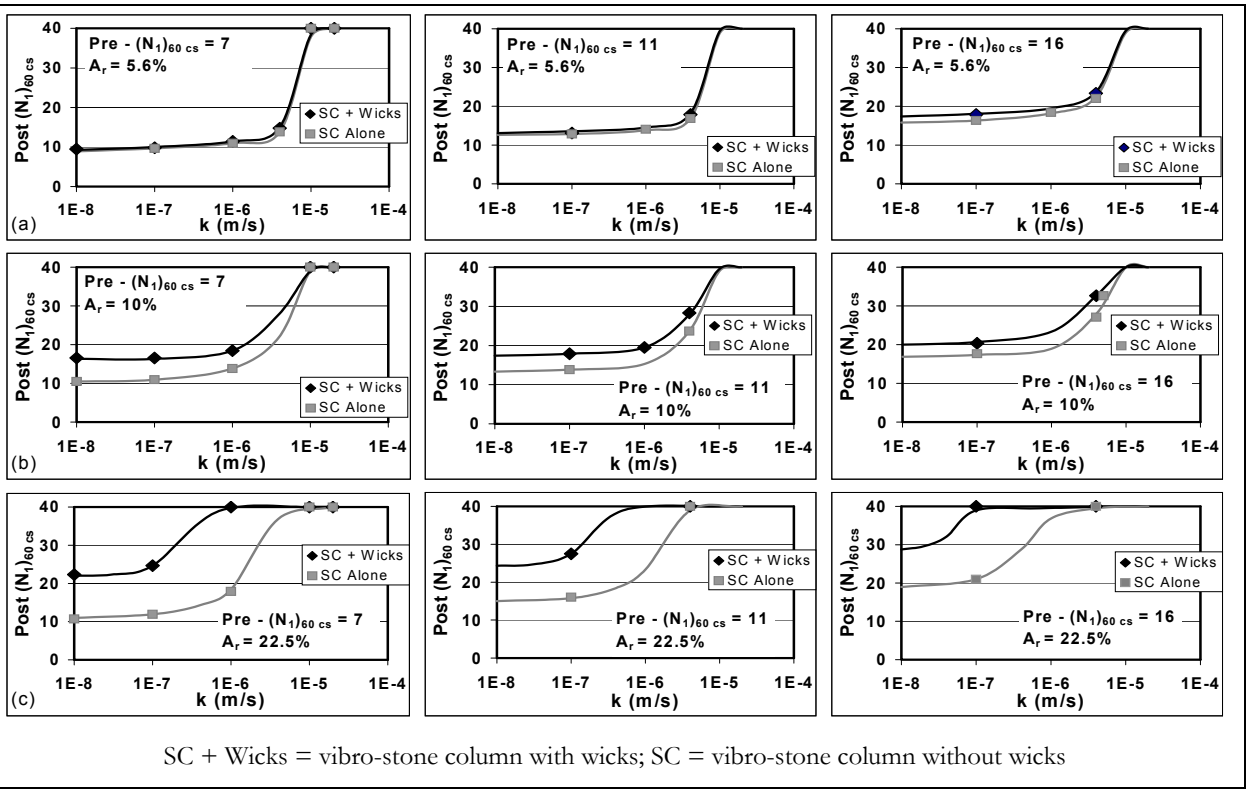

SC + Wicks = vibro-stone column with wicks; SC = vibro-stone column without wicks

Figure 3. Vibro-stone columns design charts

Field Test

Field tests were conducted, in collaboration with Hayward Baker, Inc. and Advanced Geosolutions, Inc. at a site in Marina Del Rey, CA, to assess the applicability of the above design charts for field conditions (Shenthan 2005). Figs.4a-b show a typical soil profile and pre- and post-improvement CPT profiles at the test location at the site. Liquefaction risk analysis suggested inter-bedded silty

soil layers from 2.7 m up to about 6.0 m depth were liquefiable for a design earthquake of M = 7.5 and a_{max} = 0.35 g. The silt layer to be improved at the test location has a silt content ranging from 20 to 40%. The hydraulic conductivity was estimated to be in the range of 10^{-6} to 10^{-7} m/s. Ground improvement recommendations called for SC with a diameter of 0.9 m at a spacing of 2.4 m (A_r =11%) supplemented with pre-installed wick drains (100 mm x 5 mm) at mid point between stone columns. Hayward Baker Inc. installed the stone columns. Pore pressures, ground vibrations, and energy delivered to the soil during stone column installation within a selected test section were monitored using seismic piezocones (Fugro Geosciences, Inc., CA), retrievable seismic accelerometers (www.nees.ucla.edu), and a current sensor. Three pre-improvement CPT tests and two post-improvement CPT tests were completed at the test location. A detailed analysis of these data is presented elsewhere (Shenthan 2005). Approximate average water table at the time of CPT tests and stone column installation is shown on the soil profile using dashed-line. CPT test results were interpreted following the procedures outlined by Youd et al. (2001). Normalized CPT resistance results were converted to $(N_1)_{60cs}$ using correlations recommended by Robertson and Wride (1998).

Average pre-improvement $(N_1)_{60cs}$ for the sand to silty sand to sandy silt layer (from 3.0 to 4.3m depth, Figure 4b) was estimated to be about 11, and the average post-improvement $(N_1)_{60cs}$ for this layer was estimated to be about 22. This data point is superimposed on the design chart corresponding to A_r=10%, which is the closest to the actual field A_r value. The field results are in good agreement with simulation results. Additional field data are needed to further validate the range of applicability of the simulation results.

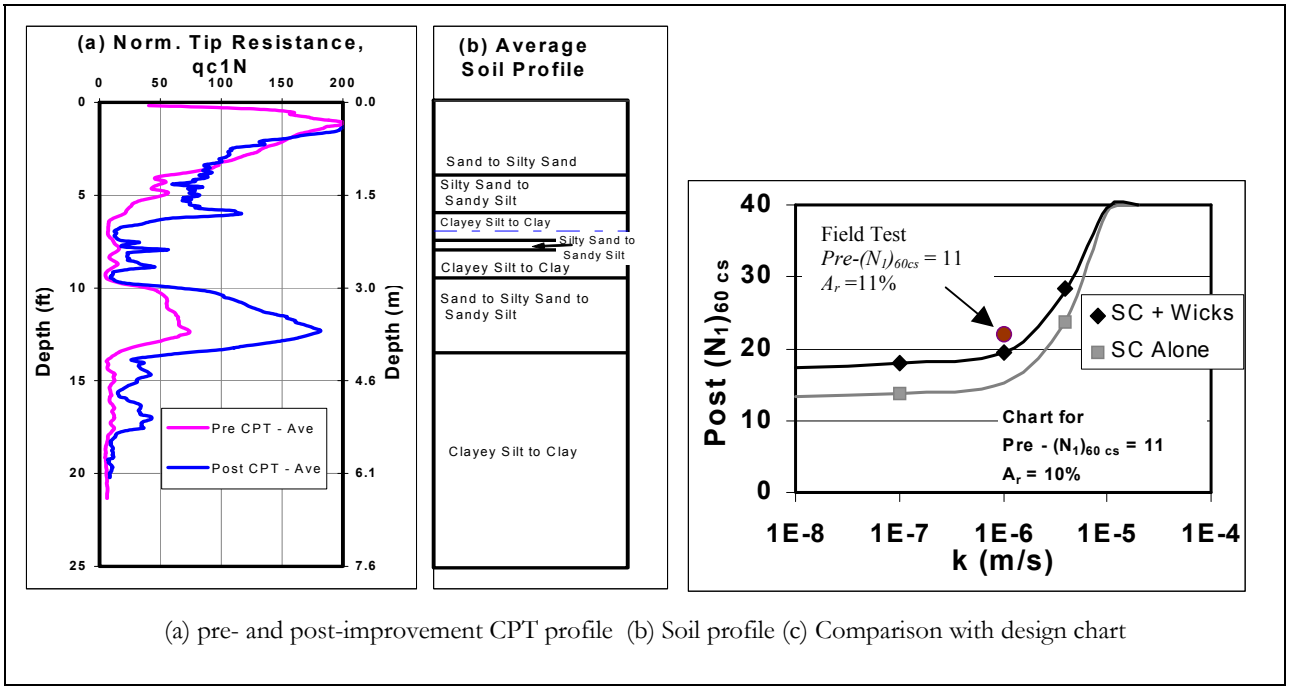

(a) pre- and post-improvement CPT profile (b) Soil profile (c) Comparison with design chart

Figure 4. Field test data

Based on the above results, a flow chart shown in Figure 5 was developed as a guideline for liquefaction mitigation design in silty soils using stone columns supplemented with pre-installed wick drains.

Concluding Remarks

Design guidelines for liquefaction mitigation of non-plastic silty soils using vibro-stone columns combined with wick drains have been presented. Field data was used to assess the applicability of these design guidelines. Results indicate that degree of improvement achievable by SC at a site depends on hydraulic conductivity and silt content. A significant increase in post-improvement $(N_1)_{60cs}$ can be achieved by vibro-stone columns combined with wick drains for soils with hydraulic conductivity as low as 10^{-7} to 10^{-8} m/s, provided that the area replacement ratio exceeds about 20%. The recommended guidelines presented herein are expected to advance the use of vibro-stone columns combined with wick drains to mitigate liquefaction potential in non-plastic silty soils, and reduce the reliance on expensive field trials as a design tool.

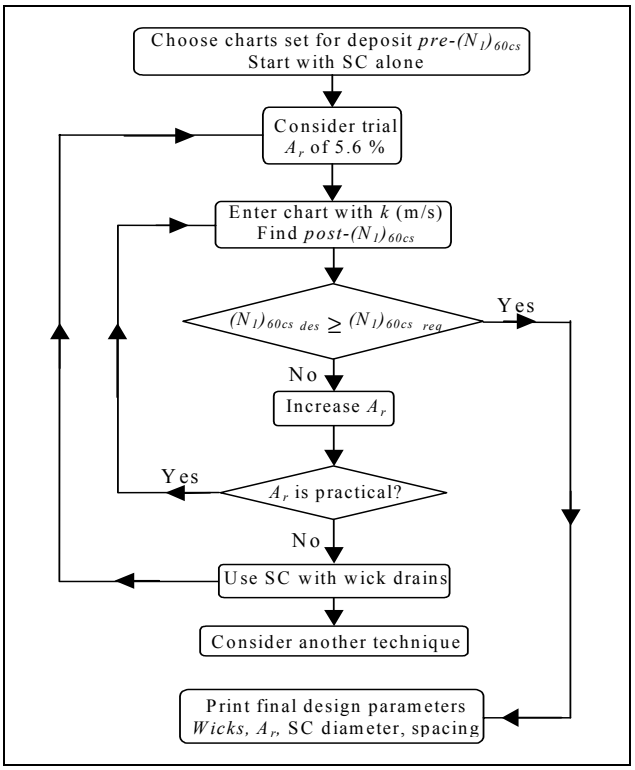

Figure 5. SC design procedure

Note: $(N_1)_{60cs,req}$ = minimum $(N_1)_{60cs}$ profile required to mitigate liquefaction at the site, obtained using a liquefaction potential analysis; pre-$(N_1)_{60cs}$ = average pre-improvement $(N_1)_{60cs}$ for the liquefiable layer at the design site; post-$(N_1)_{60cs}$ = $(N_1)_{60cs,des.}$ average post-improvement $(N_1)_{60cs}$ for the liquefiable layer at the design site obtained from the chart (Figure 3).

Acknowledgements

This research was carried out under the supervision of Dr. S. Thevanayagam, and primarily supported by FHWA, under award number DTFH61-98-C-00094 to the Multidisciplinary Center for Earthquake Engineering Research.

References

Andrews DCA (1998): Liquefaction of silty soils: susceptibility, deformation, and remediation. *Ph.D. Dissertation*, Dept. of Civil Eng., USC, CA.

Baez JI (1995): A design model for the reduction of soil liquefaction by vibro-stone columns. *Ph.D. Dissertation*, USC, Los Angeles, CA.

Dowding CH (1996): *Construction vibrations*, Prentice Hall, NJ.

FWHA (2001): Stone columns. *Ground Improvement Technical Summaries, II*, Publication No. FHWA-SA-98-086R, (7-) 1-84.

Luehring R, N Snorteland, L Mejia, and M. Stevens (2001): Liquefaction mitigation of a silty dam foundation using vibro-stone columns and drainage wicks: a case history at salmon lake dam. *Proc. 21st USSD annual meeting and lecture*, Denver, CO.

Richart FE Jr, Hall JR, Woods RD (1970): *Vibrations of soils and foundations*, Prentice-Hall, Inc., Englewood Cliffs, NJ.

Robertson PK, Wride CE (1998): Evaluating cyclic liquefaction potential using the cone penetration test. *Canadian Geotechnical Journal*, 35: 442-459.

Shenthan T, Nashed R, Thevanayagam S, Martin,G R (2004a): Liquefn. mitigation in silty soils using composite stone columns and dynamic compaction. *J. Earthq. Eng. & Eng. vibrations*, 3(1).

Shenthan T, Thevanayagam S, Martin GR (2004b): Densification of saturated silty soils using composite SC for liquefaction mitigation. *Proc., 13th WCEE*, Vancouver, BC, Canada.

Shenthan T (2005): Liquefaction mitigation in silty soils using composite stone column. *Ph.D. Dissertation*, University at Buffalo, Buffalo, NY.

Thevanayagam S, Shenthan T, Mohan S, Liang J (2002): Undrained fragility of sands, silty sands and silt. *ASCE, J. Geotech. & Geoenv. Eng.*, 128 (10), 849-859.

Thevanayagam S, Shenthan T, Kanagalingam T (2003): Role of intergranular contacts on mechanisms causing liquefaction and slope failures in silty sands. *USGS Report*, Award# 01HQGR0032 and 99HQGR0021, US Dept of Interior.

Youd et al. (2001): Liquefaction resistance of soils: summary report from the 1996 NCEER and 1998 NCEER/NSF workshops on evaluation of liquefaction resistance of soils. *J. Geot. & Geoenv. Eng.*, ASCE, 127(10): 817-33.

3

Seismic Response of Steel Framed Hospital Buildings with Self-Centering Systems

Dong Wang

Graduate Student, Department of Civil, Structural and Environmental Engineering, University at Buffalo

Research Supervisor: André Filiatrault, Professor and Deputy Director of MCEER

Summary

This paper introduces the concepts of Elasto-Plastic Systems (EPS) and Self-Centering Systems (SCS) for the seismic design of steel-framed hospital buildings. Redesign of the MCEER West Coast Demonstration Hospital with SCS is conducted using this approach. An ensemble of 25 simulated MCEER Ground Motions having a probability of exceedence of 5% in 50 years in Northridge, California is used as earthquake excitations in the seismic analysis of the building. The SCS are achieved by Post-Tensioned Energy-Dissipated (PTED) beam-to-column connections. The redesign procedure is briefly outlined. With a set of optimal design parameters for the SCS, the structural system achieves very good seismic performance. Not only are the maximum displacements reduced, but the floor accelerations are also diminished, which is rarely achieved with other passive hysteretic control systems, such as friction or metallic dampers. Also, residual drifts are largely reduced or eliminated, which will decrease the cost to repair. The improved performance obtained suggests that the implementation of SCS can lead to improved seismic behavior at a reasonable cost.

Introduction

Steel Moment Resisting Frames (SMRF) were widely used in North America and the world until the failures of brittle beam-to-column joints were observed in a large number of SMRF structures as a result of the 1994 Northridge earthquake. Before this seismic event, many practicing engineers believed for years, albeit incorrectly, that steel structures were immune to earthquake-induced damage as a consequence of the material's inherent ductile properties (Bruneau et al. 1998). However, the January 17, 1994 Northridge Earthquake (Los Angeles, CA) changed the thinking of the earthquake engineering community. Approximately 100 SMRF structures experienced beam-to-column connection fractures in the Northridge earthquake (SAC, 1995). Invisible damage to the connections was also found by ultrasonic testing method (Paret, 1999). To avoid that damage in future earthquakes, many research efforts were conducted to upgrade the earthquake codes by SAC joint venture. Other parallel research was initiated by the Federal Emergency Management Agency (FEMA). It is believed that post-Northridge buildings have better seismic performance than pre-Northridge buildings due to the current code. However, the old structures designed with pre-Northridge codes need to be redesigned. Many retrofit methods were studied to get better seismic response than that of the original buildings. The main retrofit method is passive control, including the viscous damper, friction damper, base isolation, tuned-mass damper and self-centering systems.

Concepts of Elasto-Plastic Systems (EPS) and Self-Centering Systems (SCS)

Conventional buildings are designed to have capacities of plastic deformations, ductile inelastic responses and dissipating energy during earthquakes with current codes. Such structural systems are called Elasto-Plastic Systems (EPS). Figure 1(a) indicates the idealized inelastic response of EPS during an excitation of earthquake. The shadow area represents the energy dissipated in structures. Most Steel MRF are EPS and after earthquakes, plastic rotations or local buckling developed at the ends of beams and columns, which led to much damage and cost to repair the structures and recover the normal operations. If a severe residual drift occurred, the cost of repairing the structure may be more than that of building a new one.

The idealized seismic response of Self-Centering Systems (SCS) is shown in Figure 1(b). Such a seismic response of SCS can be achieved by special energy dissipating dampers, control materials (like shape memory alloy) or special connections. The hysteretic loops in Figure 1 are different, which indicates that the energy dissipated in SCS is less than that of EPS. The reduced energy absorbed by SCS "flows" into the special devices rather than the structure itself, so the damage to the structure is diminished or eliminated. The zero residual drift in SCS can save much cost to "return" the structure to the original position compared to the large residual drift in EPS.

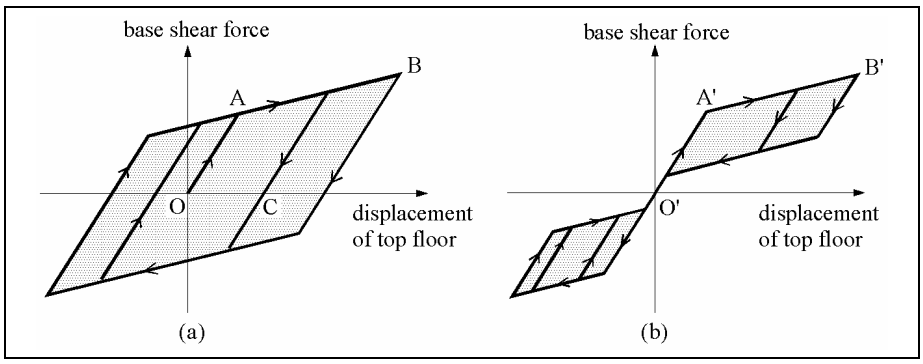

Figure 1. (a) Ideal inelastic seismic response of Elasto-Plastic Systems (EPS); (b) Ideal seismic response of Self-Centering Systems (SCS)

Control Parameters in Self-Centering Systems (SCS)

There are mainly three parameters in Self-Centering Systems: post-yielding factor α, energy dissipating factor β, strength factor η. In Figure 2, k_0 is the elastic stiffness of structures in SCS, which is same as that of EPS. And the factor α in EPS is usually equal to 0.02 which is determined by the yielding properties of structural steel. The factor α in SCS ranged from 0 to 0.35 due to the properties of special connections. The β represents the capacity of dissipating energy by SCS and is normally less than 1. The factor η is equal to the ratio of the yielding force F_Y and the gravity of structure.

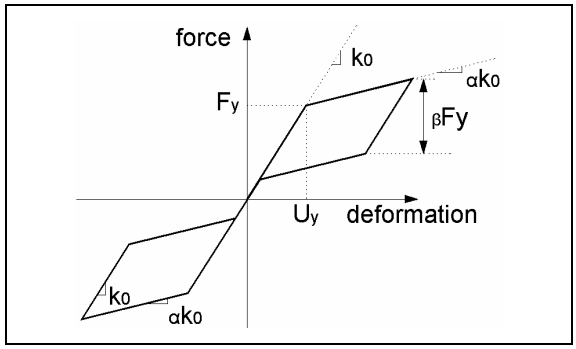

Figure 2. Parameters in Self-Centering Systems

Numerical Models

The MCEER Demonstration Hospital was constructed in early 1970s in California. Figure 3 shows the plan view of this building. More details can be found in the MCEER report by Yang et al. 2002.

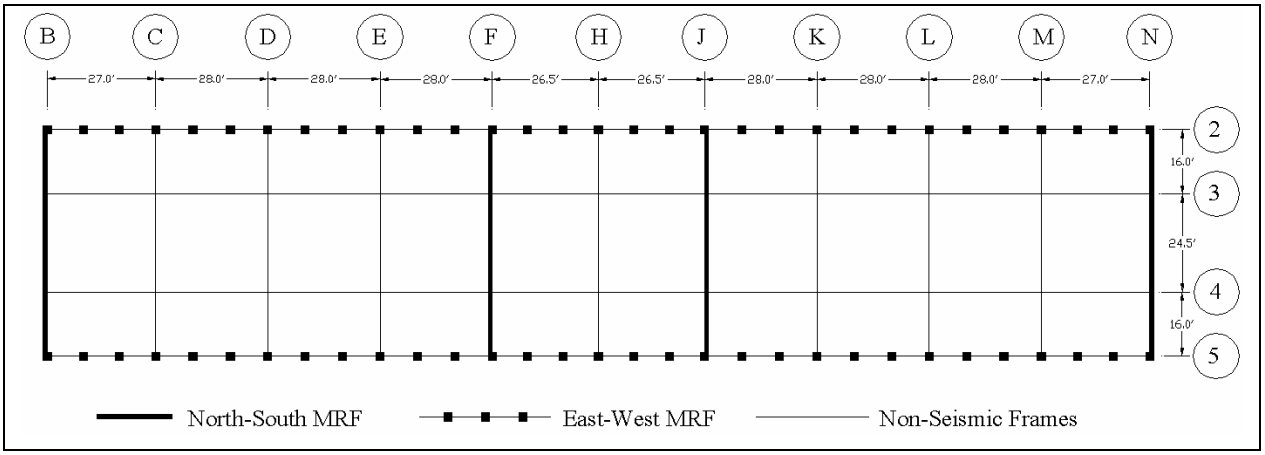

Figure 3. Plan view of MCEER Demonstration Hospital

The moment resisting system is composed by 4 North-South MRF and 2 East-West MRF. Due to the symmetry, a two-dimensional numerical model is used for modeling of the N-S MRF as shown in Figure 4. A frame element is utilized to represent all beams and columns. The inelastic response is assumed to be concentrated in the plastic hinges forming at the end of frame members. A bilinear moment-curvature hysteresis is assigned to all frame numbers. All slab contributions are neglected. The pin-ended gravity column accounts for the P-Δ effect from those non-seismic frames.

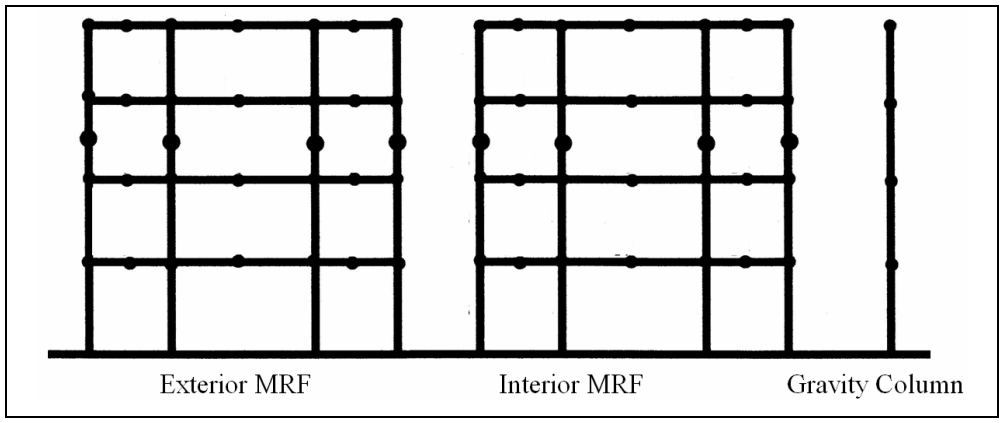

Figure 4. Two-dimensional model of the MCEER Demonstration Hospital

In order to improve the seismic performance of the original building, a Self-Centering System was used to redesign the structure by PTED beam-to-column connections. The PTED connections are shown in Figure 5. This type of connection used the post-tensioned (PT) bar to maintain the contact between beams and columns. Also, the self-centering property is conducted by the PT bar. The

energy-dissipating (ED) bar is assigned to absorb the energy and the sections of ED bars determine the shape of hysteretic loop. Shear forces are transferred by the friction between the beams and columns. The beam-to-column connections in the original building were modified by PTED connections to form a new numerical model as a Self-Centering system for seismic analysis.

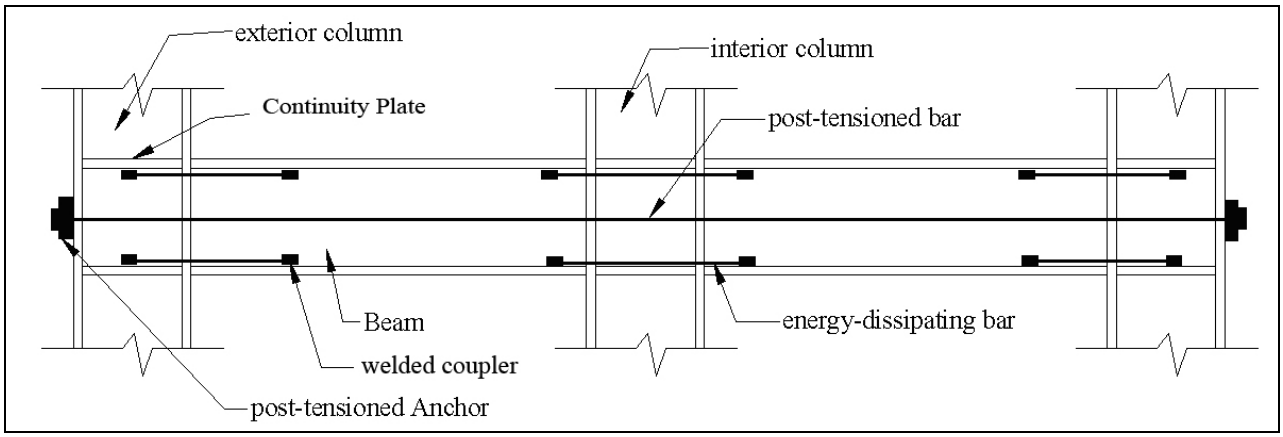

Figure 5. Post-Tensioned Energy-Dissipating (PTED) beam-to-column connections

Redesign Procedure

To redesign this MCEER hospital, the SCS is used and achieved by the Post-Tensioned Energy-Dissipating (PTED) connections (Christopoulos et al. 2002). And the MCEER West Coast Demonstration Hospital is a steel moment resisting frame and also an Elasto-Plastic system. The procedure is briefly outlined:

1) determine the properties of beam-column connections of the hospital
2) select the optimal control parameters of SCS;
3) design the post-tensioned bars and energy-dissipating bars according to selected factors
4) conduct seismic analysis of the original building and the new structure retrofitted by SCS
5) install the new connections and inspect the welded parts

More details can be found in the upcoming MCEER report by Wang, D. and Filiatrault.

Seismic Analysis of the Hospital Retrofitted with Self-Centering Systems (SCS)

Two numerical models (original EPS of the hospital and SCS of the retrofitted hospital were established and computed in RAUMOKO 2D finite element software. An ensemble of 25 simulated MCEER Ground Motions having a probability of exceedence of 5% in 50 years in Northridge, California, was used in this seismic study.

Table 1 shows the seismic responses of the original hospital and the hospital retrofitted with SCS. Comparing the responses of two systems, it is found that the maximum displacement and maximum inter-story drift are reduced in SCS. And the residual displacement and residual inter-story drift are

largely decreased. The reduced deformation response and residual drift response show that the SCS achieved better seismic performance than EPS and very small residual drift in SCS means there is much less permanent plastic deformation in structures and less damage to structural elements than EPS. By comparing the maximum absolute floor acceleration of the two systems, it is obvious that the retrofitted hospital with SCS achieved much better acceleration response and reduced the acceleration by 25%. The largely decreased acceleration response will protect the acceleration-sensitive nonstructural components. The maximum ductility of columns in SCS is reduced by approximately 30%, which largely decreased the possibility of collapse because it is known that the ductile deformation of columns is more dangerous than that of beams. The 0 max ductility of beams means the beam remains elastic and the ductile deformation was conducted by the energy-dissipating bars. So after earthquakes, only the ED bars with plastic deformation need to be renewed and the cost is much less than changing a beam with a plastic deformation or local buckling.

Table 1. Responses of seismic analysis of EPS of original hospital and SCS of retrofitted hospital

Mean Value of responses of 25 earthquakes		Original Hospital (EPS)		Retrofitted hospital (SCS) α=0.05 β=0.8 η(original)/ η(retrofit)=0.5	
	unit	mm	%	Mm	%
Max Displacement	top floor	205.46	1.32	189.14	1.22
Residual Displacement	top floor	42.47	0.27	6.17	0.04
Max Interstory Drift	1st floor	73.52	1.78	59.35	1.44
	2nd	67.14	1.76	58.71	1.54
	3rd	53.66	1.41	47.70	1.25
	4th	34.55	0.91	29.10	0.76
Residual Interstory Drift	1st	16.34	0.40	4.73	0.11
	2nd	14.15	0.37	0.88	0.02
	3rd	10.30	0.27	0.68	0.02
	4th	2.56	0.07	0.04	0.00
Acceleration Unit		g		g	
Max Absolute Floor Acceleration	1st	1.05		0.76	
	2nd	1.01		0.76	
	3rd	1.04		0.82	
	4th	1.41		1.06	
Max Ductility of Beams		5.42		0	
Max Ductility of Columns		5.23		3.69	

Conclusions

The seismic analysis indicates that the seismic performance of the MCEER demonstration hospital redesigned with Self-Centering Systems is much better than that of the original hospital. Both the maximum displacements and absolute floor accelerations are reduced, which is rarely reported in other passive control retrofit methods like viscous damper, tuned-mass damper, base isolation and friction damper. And the largely reduced or eliminated residual drifts will decrease the cost for

repairing the post-earthquake building and recovering the normal operations. Through this paper it is proved that the implementation of SCS improves the seismic performance not only from a seismic point of view but also from an economic point of view.

Acknowledgements

This study was carried out under the well-appreciated guidance of Professor André Filiatrault and was primarily supported by the Earthquake Engineering Research Centers Program of the National Science Foundation, under award number EEC-9701471 to the Multidisciplinary Center for Earthquake Engineering Research. Any opinions or conclusions presented in this paper are those of the authors and do not necessarily reflect the views of the sponsors.

References

Bruneau M, Uang CM, Whittaker A (1998): *Ductile Design of Steel Structures*. McGraw-Hill, New York, NY.

Christopoulos C, Filiatrault A, Folz B, Uang CM (2002): Post-Tensioned Energy-Dissipating Connections for Moment-Resisting Steel Frames. *ASCE Journal of Structural Engineering*, Vol. 128, No. 9, 1111-1120.

Paret TF (1999): Clarifying the Extent Northridge-Induced Weld Fracturing; Examining the Related Issue of UT Reliability. *Report No. SAC/BD-99/10*, Emeryville, CA.

SAC (1995): Steel Moment Frame Connection. Advisory No. 3, *Report No. SAC 95-01*, SAC Steel Project, Sacramento, CA.

Yang TY, Whittaker A (2002) MCEER Demonstration Hospitals. *MCEER Report Feb 2002*, Buffalo, NY.

4

Finite Element Parametric Study of Hybrid Rectangular Links for Eccentrically Braced Frames

Jeffrey W. Berman

Research Assistant, Department of Civil Structural and Environmental Engineering, University at Buffalo

Research Supervisor: Michel Bruneau, Professor and Director of MCEER

Summary

This paper describes the development and sample results of a finite element parametric study of hybrid rectangular links, involving over 200 combinations of geometries and properties. The parametric study is divided into two parts, the first part (Part 1) considers a wide range of compactnesses and link lengths to examine the difference in behavior between links satisfying and not satisfying, the proposed design requirements. The second part of the study (Part 2) involves models developed with flange compactness, web compactness, and stiffener spacings near the revised design limits, and also examines links having webs and flanges with different yield stresses (hybrid links). Links meeting the proposed design requirements were, in general, found to be able to achieve their target rotations prior to significant strength degradation from web or flange buckling.

Introduction

Hybrid rectangular links using eccentrically braced frames have been shown to be a feasible alternative for seismic protection of bridge piers for both new and retrofit construction. They are desirable in the context of bridge pier retrofit because they are self-stabilizing and do not require lateral bracing of the link, which can be difficult to provide in bridge applications. Their performance in terms of ductility, strength, and energy dissipation has been shown be similar to the levels achieved when wide-flange (WF) links are used. Rules for the design of hybrid rectangular links, including compactness requirements of webs and flanges as well as stiffener requirements and limit rotations, have been derived from various plate buckling formulations and the existing requirements for WF links (Berman and Bruneau, 2005). These proposed design rules will be compared here with the results of a finite element parametric study of hybrid rectangular links involving over 200 combinations of geometries and material properties. A general hybrid cross-section is shown in Figure 1.

The design rules proposed in Berman and Bruneau (2005) are summarized as follows:

- Plastic shear and moment for the links are given by:

$$V_p = \frac{2}{\sqrt{3}} F_{yw} t_w \left(d - 2t_f\right) \tag{1}$$

$$M_p = F_{yf} t_f (b - 2t_w)(d - t_f) + F_{yw} \frac{t_w d^2}{2} \quad (2)$$

- Flanges should have $b'/t_f \le 0.64\sqrt{E_s/F_{yf}}$, where $b' = b\text{-}2t_w$ and the limit is 15.4 for $F_{yf} = 50$ ksi and $E_s = 29000$ ksi.

- For shear links, webs should have $d'/t_w \le 1.67\sqrt{E_s/F_{yw}}$ (40.2 for $F_{yw} = 50$ ksi and $E_s = 29000$ ksi) for and webs with $d'/t_w \le 0.64\sqrt{E_s/F_{yw}}$ may be used without stiffeners, where $d' = d\text{-}2t_f$.

- Stiffeners for shear links should have a spacing, *a*, satisfying:

$$\frac{a}{t_w} + \frac{1}{8}\frac{d}{t_w} = C_B \quad (3)$$

  where C_B is 20 and 37 for anticipated maximum link rotations of 0.08 rads and 0.02 rads respectively.

- For intermediate and flexural links, webs should have $d'/t_w \le 0.64\sqrt{E_s/F_{yw}}$.

For stiffener strength and size requirements, the reader is referred to Berman and Bruneau (2005). Shear, intermediate, and flexural links are defined by the normalized link length, $\rho = M_p / V_p$, where $\rho \le 1.6$ indicates shear links with a limit rotation of 0.08 rads, $\rho > 2.6$ indicates a flexural link with a limit rotation of 0.02 rads, and values between those indicate intermediate links where their limit roation can be found via linear interpolation.

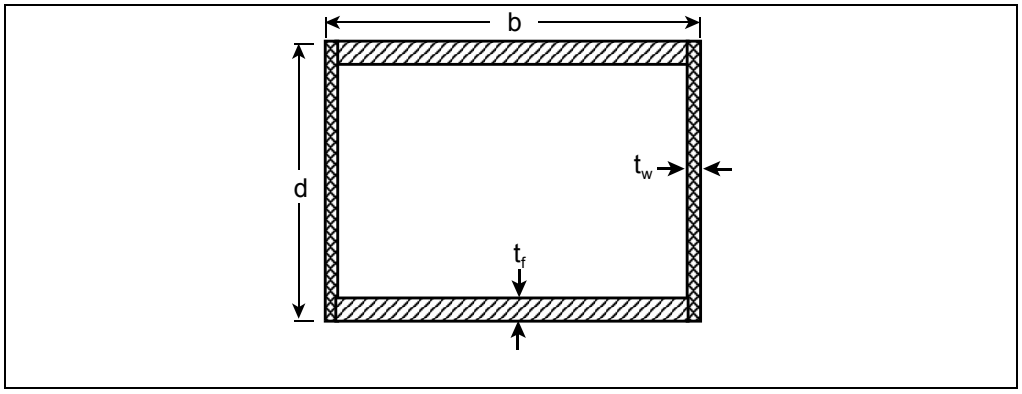

Figure 1. Hybrid rectangular link cross-section

Description of Finite Element Models

Based on the above compactness limits, models for two parts of a finite element parametric study were developed. The first part (Part 1) uses a wide range of compactnesses (both inside and outside the above limits), four normalized link lengths representing the three link types, and both stiffened and unstiffened links. This resulted in 16 different cross-sections, each of which has both stiffened

and unstiffened cases, and 128 links in total. The second part uses links with cross-sections near the proposed limits for compactnesses, four link lengths representing the three ranges of behavior, and 3 different values of both flange and web yield stress (250 MPa, 345 MPa, and 450 MPa), resulting in 18 different cross-sections and 72 total links. For both parts the normalized link lengths used were 1.2, 1.6, 2.1, and 3.0. Part 1 cross-sections are given in Table 1 and Part 2 cross-sections are given in Table 2.

Table 1. Part 1 - link dimensions

b'/t_f	8.0	17.0	24.0	40.0
b' (mm)	127	270	381	635
El. Edge-to-Thickness	1.6	1.5	1.6	1.6
d'/t_w	12.0	16.0	24.0	36.0
d' (mm)	95	127	191	286
El. Edge-to-Thickness	3.0	2.7	3.0	3.0

Table 2. Part 2 - link dimensions

Flange Dimensions			
F_{yf} (MPa)	250	345	450
b'/t_f	18.2	15.5	13.6
b' (mm)	231.1	196.9	172.7
El. Edge-to-Thickness	2.1	1.8	2.0
Unstiffened Web Dimensions			
F_{yw} (MPa)	250	345	450
d'/t_w	18.2	15.5	13.6
d' (mm)	173.4	147.6	129.5
El. Edge-to-Thickness	2.8	2.8	2.5
Stiffened Web Dimensions			
F_{yw} (MPa)	250	345	450
d'/t_w	47.5	40.3	35.4
d' (mm)	452.4	383.9	337.2
El. Edge-to-Thickness	2.7	2.6	2.6

The models were developed and analyzed in ABAQUS (HKS, 2001) using S4R four-node reduced integration shell elements. A mesh refinement analysis was performed and the element edge-to-thickness ratios given in the above tables were found to be adequate. Nonlinear material properties and nonlinear geometry were both used in the analyses. Loading corresponded to that given in the AISC Seismic Provisions (AISC, 2002) for testing link-to-column connections. Boundary conditions

were applied such that the links were restrained against all translations and rotations except at one end the translation in the link's axial direction was unrestrained and at the opposite end the vertical translation was used to apply the displacement controlled loading. These boundary conditions are similar to those used by Richards and Uang (2002) in their study of WF links and prevent the development of axial force in the link. The key parameter in the analyses is the limit rotation for each link. The limit rotation is illustrated in figure 2 and is the rotation at which the link shear degrades to below 80% of the maximum link shear achieved.

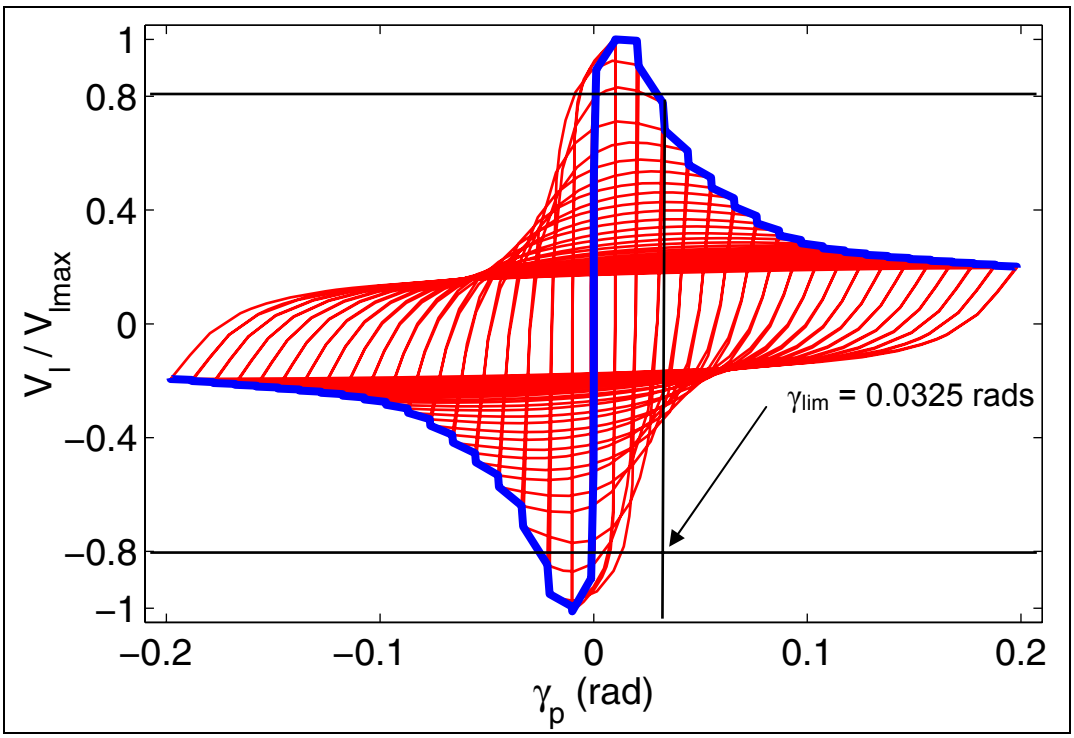

Figure 2. Evaluation of limit rotation

Example Results

An overview of results and some specific examples are provided here. For additional results, the interested reader is referred to Berman (2006). Figure 3 shows limit rotations for stiffened and unstiffened links with $b'/t_f \leq 17.0$ and $b'/t_f > 17.0$ from Part 1 of the study, versus normalized link length. It is clear from the figures that for unstiffened shear links ($\rho \leq 1.6$), the target rotation of 0.08 rads can be achieved if the flange compactness satisfies $b'/t_f \leq 17.0$ and the web compactness satisfies $b'/t_f \leq 16.0$. Stiffened shear links reach their target rotation if the flange compactness satisfies $b'/t_f \leq 17.0$ and the web compactness satisfies $b'/t_f \leq 36.0$. Example hystereses for links with flange compactness of 17.0, web compactness of 36.0 and normalized length of 1.2 are shown in Figure 4 to illustrate the effect of stiffeners for shear links with large compactnesses. Stiffeners were effective in increasing the ductility and limit rotation for this link substantially, as is the case for all shear links with large compactness.

Generally, it was found that satisfying the design requirements given in the introduction results in links that can achieve their target rotation prior to significant strength degradation from web or flange buckling. It should be noted that fracture was not included in the finite element modeling and could in certain cases occur before buckling and decrease the limit rotation below those values reported here. The results of this work will be used to design an experimental study involving twelve links to further verify the results and design recommendations.

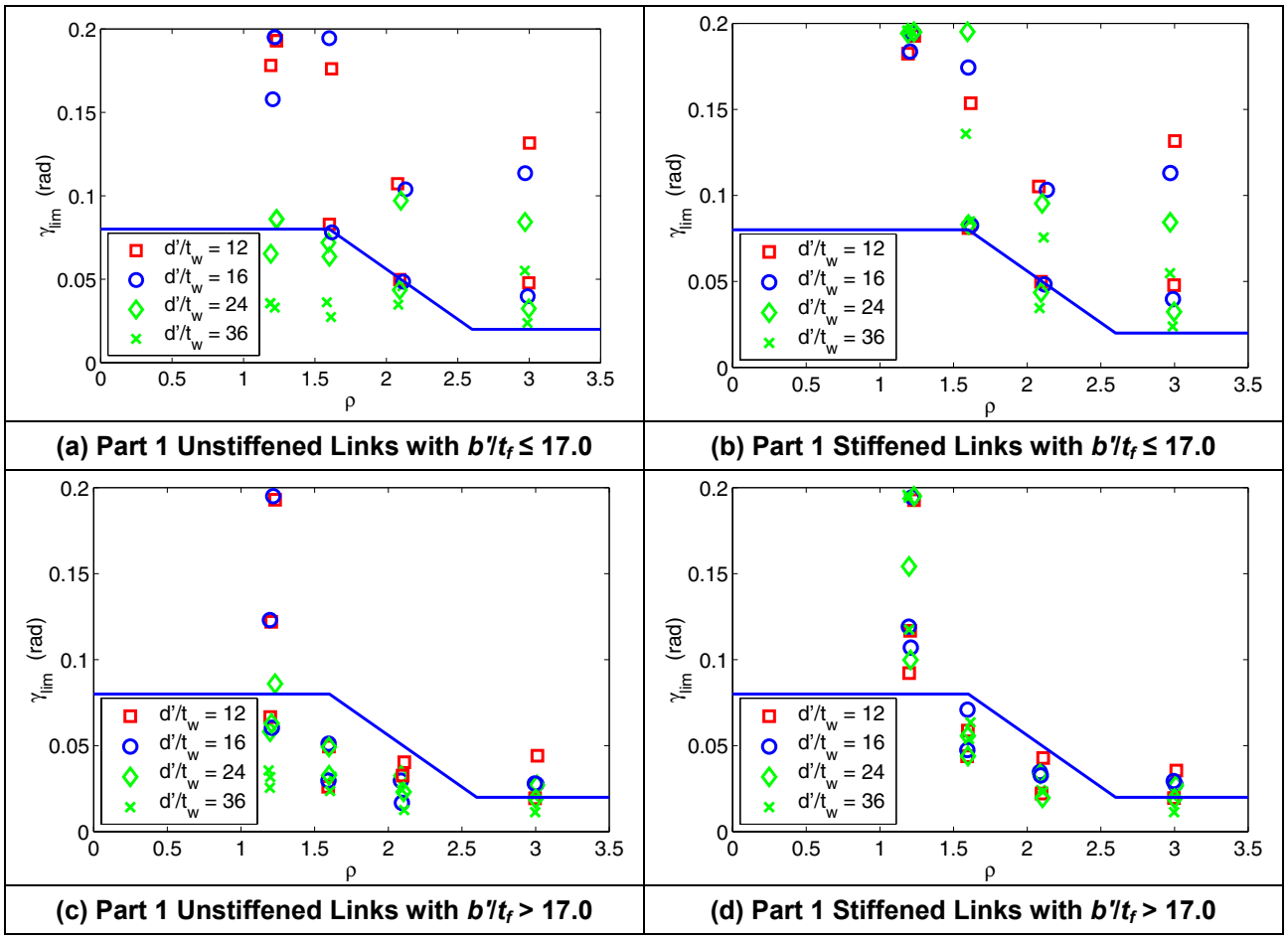

Figure 3. Limit rotations for part 1 links

Concluding Remarks

The proposed design requirements for hybrid rectangular links for eccentrically braced frames have been evaluated through a finite element parametric study. It was found that links satisfying the proposed requirements achieve their target rotations. The inclusion of stiffeners for shear links was also shown to increase ductility and limit rotation for links with large web compactness values. Results of the parametric study will also be used to design specimens for experimental work to further validate the design requirements.

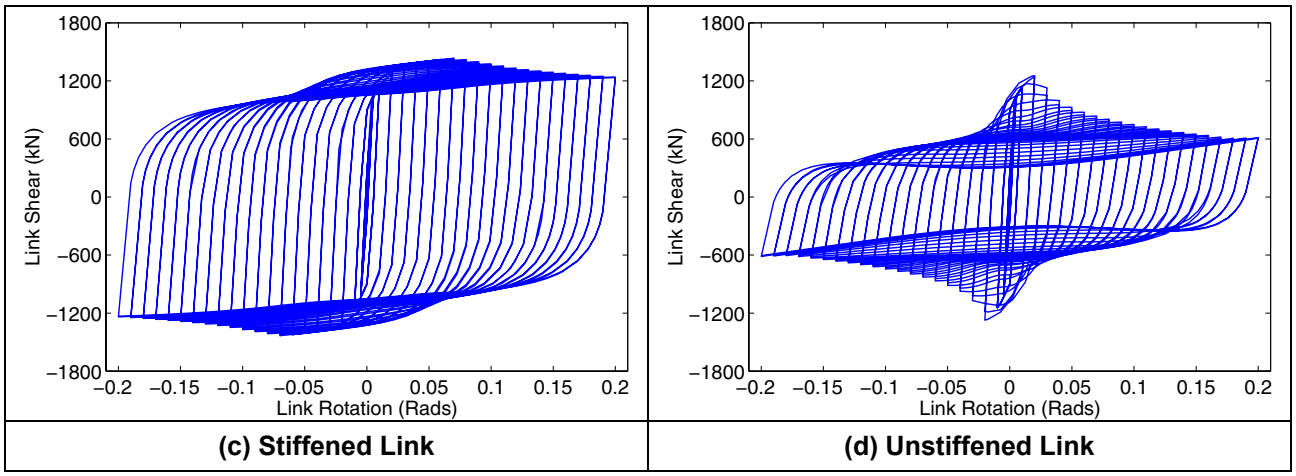

Figure 4. Hystereses for stiffened and unstiffened links with $b'/t_f = 17.0$, $d'/t_w = 16.0$, and $\rho = 1.2$

Acknowledgements

This research was carried out under the supervision of Dr. Michel Bruneau, and was supported by the Federal Highway Administration under contract number DTFH61-98-C-00094 to the Multidisciplinary Center for Earthquake Engineering Research. However, any opinions, findings, conclusions, and recommendations presented in this paper are those of the author and do not necessarily reflect the views of the sponsors.

References

AISC (2002): *Seismic Provisions for Structural Steel Buildings.* American Institute of Steel Construction, Chicago, IL.

Berman, J.W. (2006): Approaches for the Seismic Retrofit of Braced Steel Bridge Piers and the Development of Self-Stabilizing links for Eccentrically Braced Frames. (Tentative Title) Ph.D. Dissertation, State University of New York at Buffalo, Buffalo, NY (in progress – completion expected in Feb. 2006).

Berman, J. W., and Bruneau, M. (2005): Approaches for the Seismic Retrofit of Braced Steel Bridge Piers and Proof-of-Concept Testing of a Laterally Stable Eccentrically Braced Frame. *Technical Report MCEER-05-0004*, Multidisciplinary Center for Earthquake Engineering Research, Buffalo, NY.

HKS (2001): *ABAQUS Standard User's Manual.* Hibbitt, Karlsson, and Sorensen, Inc., Pawtucket, RI.

Richards, P., and Uang, C.M. (2002): Evaluation of Rotation Capacity and Overstrength of Links in Eccentrically Braced Frames. *Report No. SSRP-2002/18*, Structural Systems Research Project, Department of Structural Engineering, University of California San Diego, La Jolla, CA.

5

Seismic Resilience

Gian Paolo Cimellaro

Graduate Research Assistant, Department of Civil, Structural and Environmental Engineering, University at Buffalo

Research supervisors: Andrei M. Reinhorn, Professor and Director of SEESL

Michel Bruneau, Professor and Director of MCEER

Summary

The concepts of seismic resilience need a unified terminology and a common reference frame for quantitative evaluation of such resilience. The evaluation can be based on non-dimensional analytical functions related to loss variation within a specified "recovery period". The path to recovery usually depends on available resources and may take different shapes which can be estimated by proper recovery functions. The loss functions have uncertainties due to the nature of the earthquake, structural behavior and the description of functionality limits. Therefore losses can be described as functions of fragility of systems' components. These fragility functions can be determined through the use of multidimensional performance limit thresholds, which allow consideration of simultaneously different mechanical-physical variables. A procedure which defines resilience as function of losses and time recovery based on multidimensional fragility system is formulated and exemplified for a typical California hospital building considering direct and indirect losses in its physical system and in the population served by the system.

Introduction

Seismic resilience as defined in this paper describes the loss and loss recovery required to maintain the function of the system with minimal disruption. So while mitigation may emphasize use of new technologies and implementation of policies to reduce losses, the resilience considers also the recovery process including behavior of individuals and organizations in the face of a disaster. A wealth of information is available on specific actions, policies or scenarios that can be adopted to reduce the direct and indirect economic losses attributable to earthquakes, but there is little information on procedures on how to quantify these actions and policies. Seismic resilience can compare losses and different pre- and post- event measures verifying if these strategies and actions can reduce or eliminate disruptions in the presence of earthquake events.

Bruneau et al. (2003) offered a very broad definition of resilience to cover all actions that reduce losses from hazard, including mitigation and more rapid recovery. The authors suggested that resilience can be conceptualized along four interrelated dimensions: technical, organizational, social and economic (TOSE). They defined a fundamental framework for evaluating community resilience without any actual quantification and implementation. Chang and Shinozuka (2004) proposed a series of quantitative measures of resilience and demonstrated them in a particular case study of an actual community, the seismic mitigation of Memphis water system.

This paper attempts to provide a quantitative definition of resilience through the use of an analytical function, which allows identification of quantitative measures of resilience. More detailed information can be found in Cimellaro, Reinhorn et. al. (2006).

Definitions and Formulations

To establish a common frame of reference, the fundamental concepts of resilience are analyzed, a unified terminology is proposed and an application to health care facilities is presented:

Definition 1: *Resilience is defined as a normalized function indicating capability to sustain a level of functionality or performance for a given building, bridge, lifeline, network or community over a period of time, T_{LC}, (life cycle, life span etc.) including the recovery period after damage in an extreme event.*

The time, T_{LC}, includes the building recovery time, T_{RE}, and the business interruption time that is usually smaller compared to the other one.

Definition 2: *The recovery time, T_{RE}, is the time necessary to restore the functionality of a community or a critical infrastructure system (water supply, electric power, hospital etc.) to a desired level below, same or better than the original, allowing proper operation of the system.*

The recovery time, T_{RE} (I, location), is the most difficult quantity to predict and it typically depends on the earthquake intensities, the type of area considered and the availability of resources such as capital, materials and labor following a major seismic event. Resilience is defined graphically as the normalized shaded area underneath the function shown in Figure 1 where in the x-axis there is the time range considered to calculate resilience while in the Y-axis there is the functionality Q(t) of the system. Analytically resilience can be expressed by equation (1):

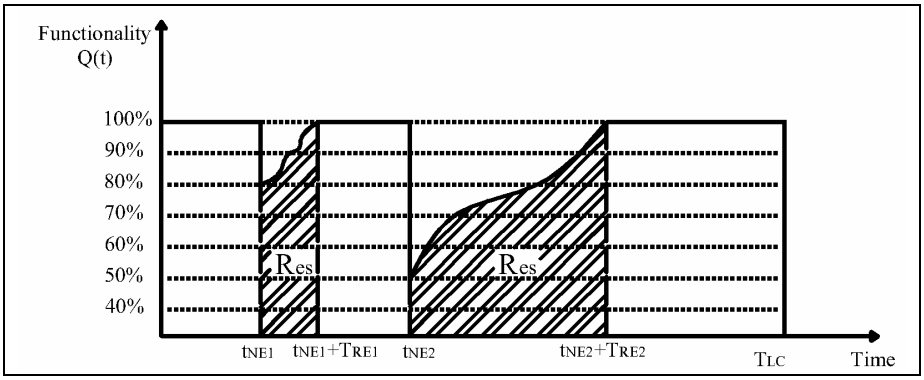

Figure 1. Uncoupled resilience

$$\bar{R}=\frac{1}{N_I}\sum_{I=1}^{N_I}\left\{\frac{1}{N_E}\cdot\sum_{E=1}^{NE}\frac{1}{T_{RE}}\cdot\int_{t_{0E}}^{t_{0E}+T_{RE}}\left\{1\text{-}L(I,T_{RE})\cdot\left[\begin{array}{l}H(t\text{-}t_{0E})+\\-H(t\text{-}(t_{0E}+T_{RE}))\end{array}\right]\cdot\right\}\cdot dt\cdot p_E(0,T_{LC})\right\}\cdot P(I) \qquad (1)$$

$$\cdot\alpha_R\cdot f_{Rec}(t,t_{0E},T_{RE})$$

Where NE is the number extreme events expected during the lifespan (or control period) T_{LC} of the system, NI is the number of different extreme events intensities expected during the lifespan (or

control period) T_{LC} of the system; T_{RE} is the recovery time from event E; t_{0E} is the time of occurrence of event E; $L(I,T_{RE})$ is the normalized loss function; f_{REC} (t,t_{0E}, T_{RE}) is the recovery function; P(I) is the Probability that an event I of given intensities happens in a given time interval T_{LC}; $pE(0,T_{LC})$ is the probability that an event happens E times in a given time interval T_{LC}; αR is a recovery factor and H(t0) is the Heaviside step function. In equation (1) there are the loss function $L(I,T_{RE})$, the recovery function f_{REC} (t,t_{0E}, T_{RE}) and the fragility function that does not appear explicitly, but it is included in the loss function that will be defined in the following section.

Loss Function

Losses associated with extreme events are highly uncertain and they are different for every specific scenario considered, but considering all the possible cases some common parameters that influence the losses can be identified. In fact, the loss function $L(I,T_{RE})$ can be expressed as a function of earthquake intensity I and recovery time T_{RE} (downtime). The losses are divided in two groups: **Structural losses** $[L_S]$ and **Nonstructural losses** $[L_{NS}]$. The nonstructural losses can be divided in four contributions: (i) Direct economic losses $L_{NS,DE}$ (Contents losses); (ii) Direct Causalities losses $L_{NS,DC}$; (iii) Indirect economic losses $L_{NS,IE}$ (Business interruption losses); (iv) Indirect Causalities losses $L_{NS,IC}$. The physical structural losses are expressed as ratio of building repair and replacement costs and it is expressed as:

$$L_S(I) = \sum_{j=1}^{5}\left[\frac{C_{S,j}}{I_S}\cdot\prod_{i=1}^{T_i}\frac{(1+\delta_i)}{(1+r_i)}\right]\cdot P_j\left(R_j \geq d.s_j / I\right) \qquad (2)$$

Where P_j is the probability of exceeding a performance limit state j conditional an extreme event of intensity I happens (the fragility function); $C_{s,j}$ are the building repair costs associate to a j damage state; I_s are the replacement building costs; r is the discount annual rate: t_i is the time range in years between the initial investments and the time occurrence of the extreme event; δ_i is the depreciation annual rate. A similar formulation is used for nonstructural direct economic losses $L_{NS,DE,k}(I)$ where an identical term to equation (2) is obtained for every nonstructural component used inside the affected system. This term can be much higher than the structural losses in essential facilities like hospitals or research laboratory.

The **direct causalities losses** L_{DC} are expressed as ratio between the number of person injured N_{in} over the total number of occupants N_{tot}:

$$L_{NS,DC}(I) = \frac{N_{in}}{N_{tot}} \qquad (3)$$

The number of injured people N_{in} in fatal and nonfatal manner depends on multiple factors like, the *time of the day of the earthquake*, *the age of the population* and the *number and proximity of available hospitals*.

The **indirect economic losses** $L_{NS,IE}(I, T_{RE})$ are time dependent compared to all the previous losses considered. They are the most difficult post-earthquake losses to quantify, because of the different forms they can assume, so at the moment there is no equation for this term. They can be generated by *business interruptions*, *relocation expenses*, *rental income losses, etc.* Finally the total direct losses $L_{NS,D}$ and the total indirect losses $L_{NS,I}$ and the total nonstructural losses L_{NS} are combined in a final term that describe the losses.

Recovery Function

Different kind of recovery functions can be chosen depending on system and society response. Three recovery functions are shown in equation (4): linear, exponential and trigonometric:

$$f_{rec}(t,T_{RE}) = \left(1 - \frac{t - t_{0E}}{T_{RE}}\right) \quad f_{rec}(t) = \exp\left[-(t-t_{0E}) * (\ln 200)/T_{RE}\right] \quad f_{rec}(t) = 0.5 * \left\{1 + \cos\left[\pi (t-t_{0E})/T_{RE}\right]\right\} \quad (4)$$

The simplest form is a linear recovery function that is generally used when there is no information regarding the society's response. The exponential recovery function is used where the society response to an extreme event is very fast, driven by an initial inflow of resources, but then the rapidity of recovery decreases. Trigonometric recovery function is used when the society response to a drastic event is very slow initially. This could be due to lack of organization and/or resources. As soon the community organizes itself, thanks for example to the help of other communities, then the recovery system starts operating and the rapidity of recovery increases.

Fragility

The calculation of seismic resilience implies the determination of fragility that explicitly appears in the expression of the loss function (2) where the normalized value of the losses is multiplied by $P_j(R_j \geq d.s_j/I)$, the probability of exceeding a given performance level conditional an event of intensity I happens. In N dimensional form can be expressed by the following equation:

$$Fragility = P\left\{R_1 \geq r_{\lim 1} \cup R_2 \geq r_{\lim 2} \ldots \cup R_N \geq r_{\lim N} / I\right\} = P\left\{\bigcup_{i=1}^{N} R_i \geq r_{\lim i} / I\right\} \quad (5)$$

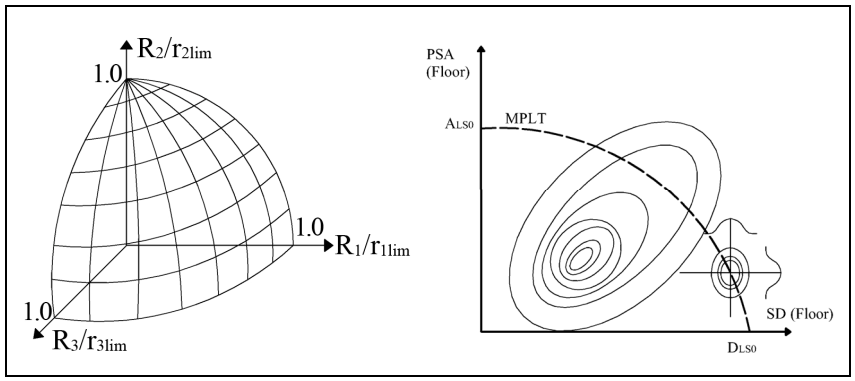

Figure 2. Multidimensional Threshold performance limit (a)3D (b)2D

Where R_i is the response parameter related to a certain quantity (deformation, force, velocity, etc.); $r_{\lim i}$ is the response threshold parameter related to a certain quantity that is correlated with the performance level. The definition of fragility in equation (5) requires implicitly the definition of the N-dimensional performance limit state thresholds Eq. (6) (Cimellaro et. al. 2005). The different limit states can be modeled as deterministic or random variables and they can be considered either linear, non linear dependent or independent using an opportune choice of the parameters.

$$L(R_1, \ldots R_n) = \sum_{i=1}^{n} \left(\frac{R_i}{r_{i\lim}}\right)^{Ni} - 1 \quad (6)$$

Case Study: Demonstration Hospital

The methodology described above has been applied to an essential facility in the San Fernando Valley in Southern California. The computer program IDARC2D (Reinhorn et al. 2004) has been used to perform the non linear time history analysis of the hospital using a bi-dimensional inelastic MDOF model. A series of 100 synthetic near fault ground motions (MCEER database), has been used to build the fragility curves of the building using the procedure described in Cimellaro et al. (2005). The structural losses for this type of building have been taken equal to 0.2%, 1.4%, 7.0% 14.0% of the building replacement costs for the case of slight, moderate, extensive and complete damage, respectively. A discount annual rate of 4% and a depreciation annual rate of 1% have been used. The nonstructural losses have been taken equal to 1.8%, 8.6%, 32.8% 86% of the building replacement costs for the same damage states. The number of people injured compared to the 4000 people assumed inside the hospital, and the 1000 outside the hospital are for different damage states equal to 0.05%, 0.23%, 1.1%, 6.02% and 75% of the occupants (FEMA 2001). Severity of the casualties was not differentiated. Other losses like the relocation costs, rental income losses and the loss of income have been also considered using the procedure described in HAZUS for this type of building. Finally, Figure 3 shows the functionality curves related to the four different hazard level considered for different types of recovery functions. The values of resilience functions for the four different hazard levels represented by probability of exceedence (PE) in 50 years are reported in Table 1. The resilience of the building is almost constant with the increase of earthquake intensity showing a good behavior of the building. If we compare the functionality values, we observe a reduction with the increase of the magnitude as expected due to the increase of the losses and consequentially, the effective recovery time.

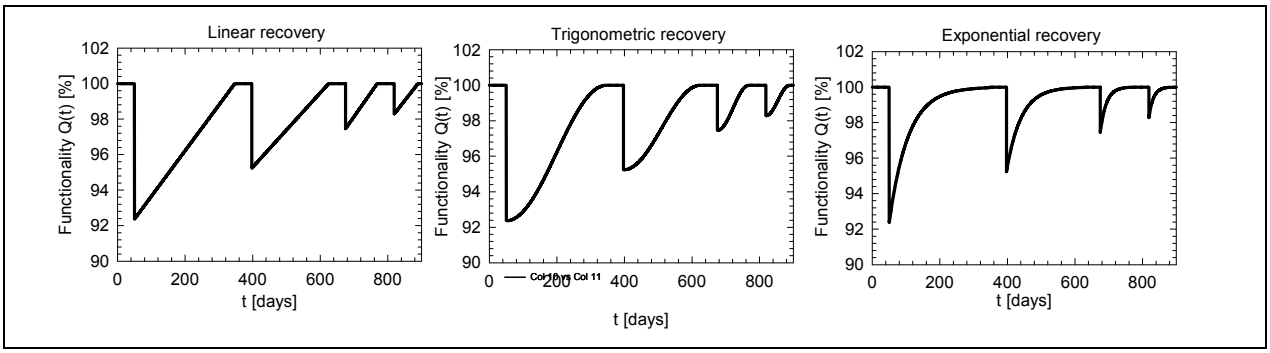

Figure 3. Functionality curves

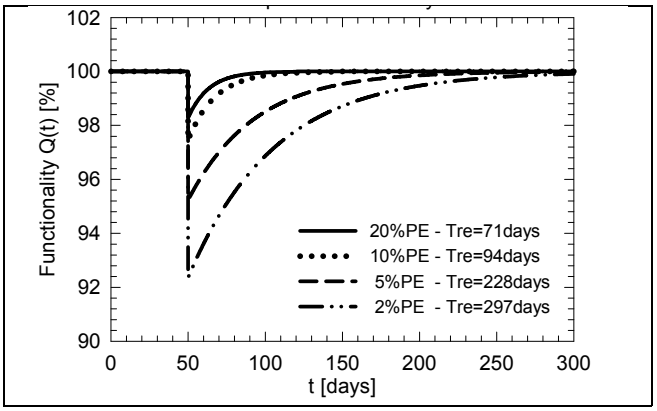

Figure 4. Comparison of functionality curves

Table 1. Seismic resilience and recovery time vs. different risk hazard levels

PE	Resilience	Tre [days]
20%	0.99178	71
10%	0.98783	94
5%	0.97699	228
2%	0.96282	297

Concluding Remarks

The definition of seismic resilience combines information from technical and organizational fields, from seismology and earthquake engineering to social science and economy. So it is clear that many assumptions and interpretations are made during the study of seismic resilience, but the final goal is to integrate the information from these fields in a unique function that reaches results that are unbiased by uninformed intuitions or preconceived notions of how large or how small the risk is. The goal of this paper is to provide a quantitative definition of resilience in a rational way through the use of an analytical function that may fit both technical and organizational issues. A common frame of reference is established for seismic resilience, a unified terminology is proposed and an application to health care facilities is presented. However, it is important to mention that the assumptions that are made for the case presented are only representative to illustrate the definitions; for other problems users calculating resilience should focus on the assumptions that most influence the problem at hand.

Acknowledgements

This research was carried out under the supervision of Andrei M. Reinhorn and primarily supported by the Earthquake Engineering Research Centers Program of the National Science Foundation under Award Number EEC-9701471 to the Multidisciplinary Center for Earthquake Engineering Research. Any opinions, findings and conclusions or recommendations expressed in this paper are those of the author(s) and do not necessarily reflect those of the National Science Foundation or New York State.

References

Bruneau M, Chang S, Eguchi R, G Lee, O'Rourke T, Reinhorn AM, Shinozuka M, Tierney K, Wallace W, Winterfelt DV (2003): A framework to Quantitatively Assess and Enhance the Seismic Resilience of Communities. *EERI Spectra Journal*, 19(4), 733-752.

Chang S, Shinozuka M (2004): Measuring Improvements in the disaster Resilience of Communities. *EERI Spectra Journal*, 20(3), 739-755.

Cimellaro GP, Reinhorn AM, Bruneau M (2006): Quantification of Seismic Resilience. *Proceedings of the 8th National Conference of Earthquake Engineering*, paper 1094, San Francisco, California, April 18-22.

Cimellaro GP, Reinhorn AM, Bruneau M: (2005), Multidimensional Fragility of Structures: Formulation and Evaluation. *MCEER Technical Report* (under review.)

Reinhorn AM, et al. (2004): IDARC2D Version 6.0 - A computer Program for the Inelastic Damage Analysis of Reinforced Concrete Buildings. latest release retrieved from *http://civil.eng.buffalo.edu/idarc2d50*, July.

Reinhorn A, Viti S, Cimellaro GP (2005): Retrofit of Structures: Strength Reduction with Damping Enhancement. *Proceedings of the37th UJNR panel meeting on wind and seismic effects*, 16-21 May, 2005, Tsukuba, Japan.

6

The Double Concave Friction Pendulum Bearing

Daniel Fenz

PhD. Candidate, Department of Civil, Structural and Environmental Engineering, University at Buffalo

Research Supervisor: Michael Constantinou, Professor

Summary

The Double Concave Friction Pendulum (DCFP) bearing is an adaptation of the well-known single concave Friction Pendulum bearing. The principal benefit of the DCFP bearing is its capacity to accommodate substantially larger displacements compared to a traditional FP bearing of identical plan dimensions. Moreover, by using concave surfaces having different radii of curvature and coefficients of friction, there is greater flexibility in design to optimize performance. This paper describes the principles of operation of the bearing and presents sample results of characterization testing.

Introduction

The Double Concave Friction Pendulum (DCFP) bearing consists of two facing concave stainless steel surfaces. The concept of a double concave bearing represents the first documented proposal for a seismic isolation system. The 1870 US patent of Jules Touaillon (1870) describes a double concave rolling ball bearing. It took nearly 130 years since then to practically implement a double concave isolation system. Hyakuda et al. (2001) presented the description and observed response of a seismically isolated building in Japan which utilized DCFP bearings with sliding surfaces having equal radii of curvature and coefficients of friction. Tsai et al. (2005) described a DCFP bearing and presented experimental and analytical results on the behavior of the bearing under conditions of concave surfaces of equal radii and equal coefficients of friction at the top and bottom sliding surfaces. This paper presents a more generalized form of the lateral force-displacement relationship that accounts for (a) the possibility of the upper and lower concave surfaces having different radii of curvature, (b) the possibility of the upper and lower concave surfaces having different coefficients of friction and (c) the effect of the height of the articulated slider on the lateral force-displacement relationship.

Principles of Operation

Figure 1 shows cross sections of the DCFP bearing at various stages of lateral movement: (a) zero displacement, (b) displaced with sliding occurring only on the bottom surface and (c) at maximum displacement. In Figure 1(a), the upper and lower concave surfaces have radii of curvature R_1 and R_2, respectively and coefficients of friction μ_1 and μ_2 respectively. The radii of curvature and coefficients of friction on the upper and lower surfaces may be different. An articulated slider separates the two surfaces. The articulation is necessary for proper distribution of pressure on the sliding surfaces and to allow for differential rotation.

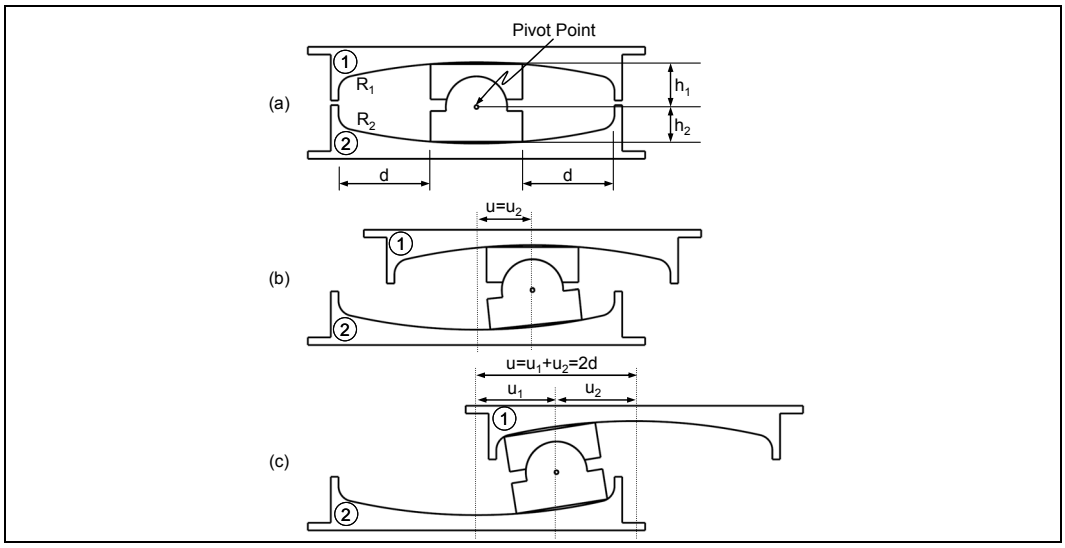

Figure 1. Cross section of DCFP bearing at various stages of lateral movement

In Figure 1(b), the bearing is shown with sliding occurring only on the lower concave surface. This is possible when the coefficient of friction on the lower concave surface is less than that on the upper surface ($\mu_2 < \mu_1$). When friction differs on the upper and lower concave surfaces, sliding initiates on the surface of least friction and is followed by sliding on both surfaces, regardless of the radii of curvature or values of the coefficient of friction on the two surfaces. This condition of sliding on only one surface occurs upon initiation or reversal of motion and is typically of small displacement amplitude.

In Figure 1(c), it is shown that the maximum displacement capacity of the DCFP bearing is 2*d*, where *d* is the maximum displacement capacity of a single concave surface. Since sliding is possible on both concave surfaces, the displacement capacity of the DCFP bearing is substantially larger than that of a traditional Friction Pendulum bearing with identical plan dimensions.

When sliding is occurring on both surfaces, the restoring force, F_r, is given by

$$F_r = \frac{W}{R_1 + R_2 - h_1 - h_2} u \tag{1}$$

Where W is the vertical compressive load on the bearing, h_1 and h_2 are the part heights of the articulated slider and u is the total displacement of the bearing (top plate with respect to bottom plate). The friction force F_f, is given by

$$F_f = \frac{\mu_1 (R_1 - h_1) W + \mu_2 (R_2 - h_2) W}{R_1 + R_2 - h_1 - h_2} \tag{2}$$

In most applications of DCFP bearing, the radii of the upper and lower concave surfaces will be equal, that is R_1-$h_1 \approx R_2$-h_2. In this case, the bearing behaves as the standard Friction Pendulum bearing with an effective coefficient of friction equal to the average of μ_1 and μ_2.

Characterization Testing

Characterization testing of a DCFP bearing was performed to confirm the theoretical predictions of behavior. Testing was performed at the University at Buffalo using the small bearing testing machine pictured in Figure 2. The machine consists of one horizontal actuator and two vertical actuators and is capable of testing bearings under controlled conditions of vertical load, lateral movement and rotational movement. Reaction forces (vertical and lateral) are measured by a load cell mounted directly beneath the bearing and lateral displacement is measured by an internally mounted LVDT on the horizontal actuator. In addition, a string pot type displacement transducer was attached to the articulated slider to allow for direct measurement of the displacement on the bottom concave surface. Therefore, the overall motion could be decomposed into the two components on the upper and lower concave surfaces.

The tested bearing had two identical concave plates having radius of curvature of 474 mm and an articulated slider with a diameter of 76 mm and a height of 68 mm. The diameter of each concave surface was 229 mm, yielding an overall displacement capacity of approximately 150 mm. A drawing of the tested bearing is shown in Figure 3. The bearing was tested under a vertical compressive load of 60 kN. A sinusoidal lateral displacement history having amplitude of 100 mm and frequency of 0.10 Hz was imposed. The results presented in this paper are for the case of different friction on the upper and lower concave surfaces. To achieve this large difference in the coefficient of friction, a silicone based lubricant was applied to the bottom face of the articulated slider.

Figure 2. Small bearing testing machine

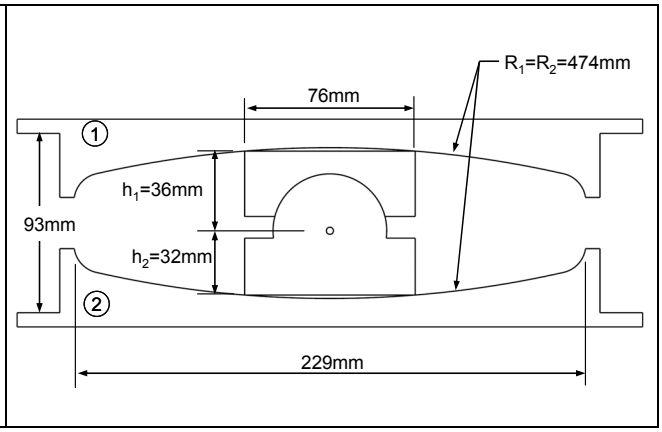

Figure 3. Dimensions of tested bearing

Results of testing are presented in Figures 4 through 6. Figure 4 shows a photograph of the bearing at maximum displacement. Figure 5 shows a comparison of normalized lateral force-displacement loops recorded during testing to the behavior predicted by equations (1) and (2). Figure 6 shows histories of bearing displacement and velocity. When friction on the two concave surfaces is different, the bearing's behavior is rigid bilinear. Upon initiation or reversal of motion, sliding occurs only on the surface of least friction. This is demonstrated by the periods of zero velocity on the upper concave surface shown in Figure 6. Accordingly, the stiffness during this period is related only to the radius of the surface upon which sliding is occurring. When sliding occurs on both surfaces, the stiffness is related to the radii of both surfaces as predicted by equation (1).

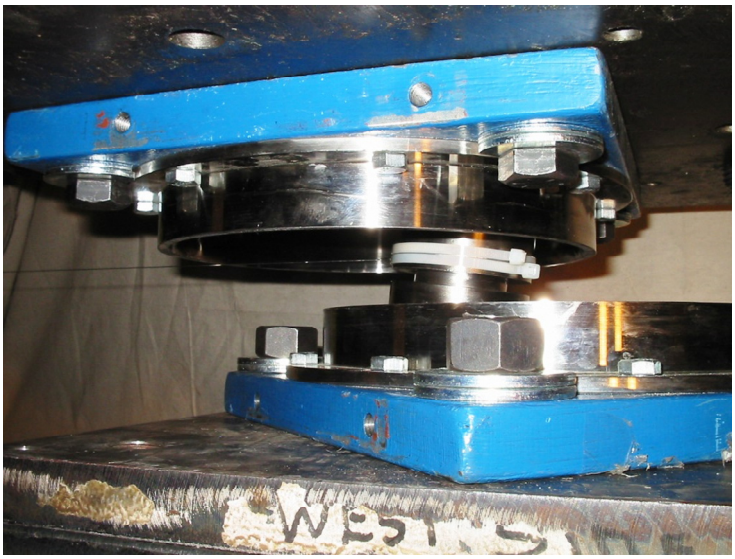

Figure 4. Photograph of the bearing at maximum displacement

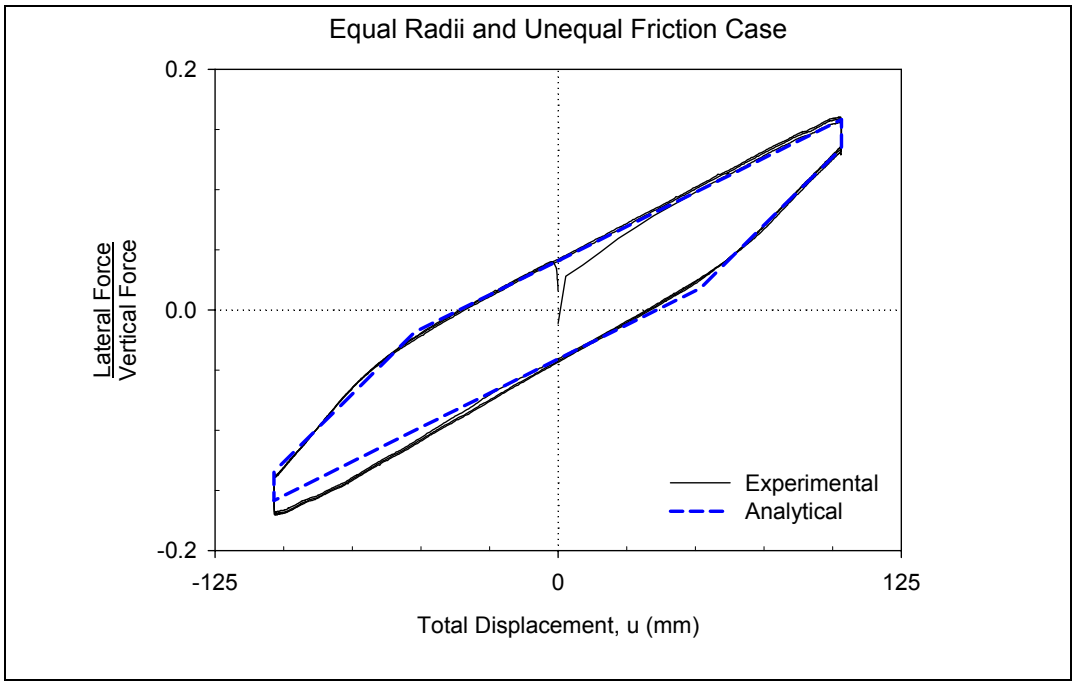

Figure 5. Normalized lateral force-displacement relationship for tested bearing

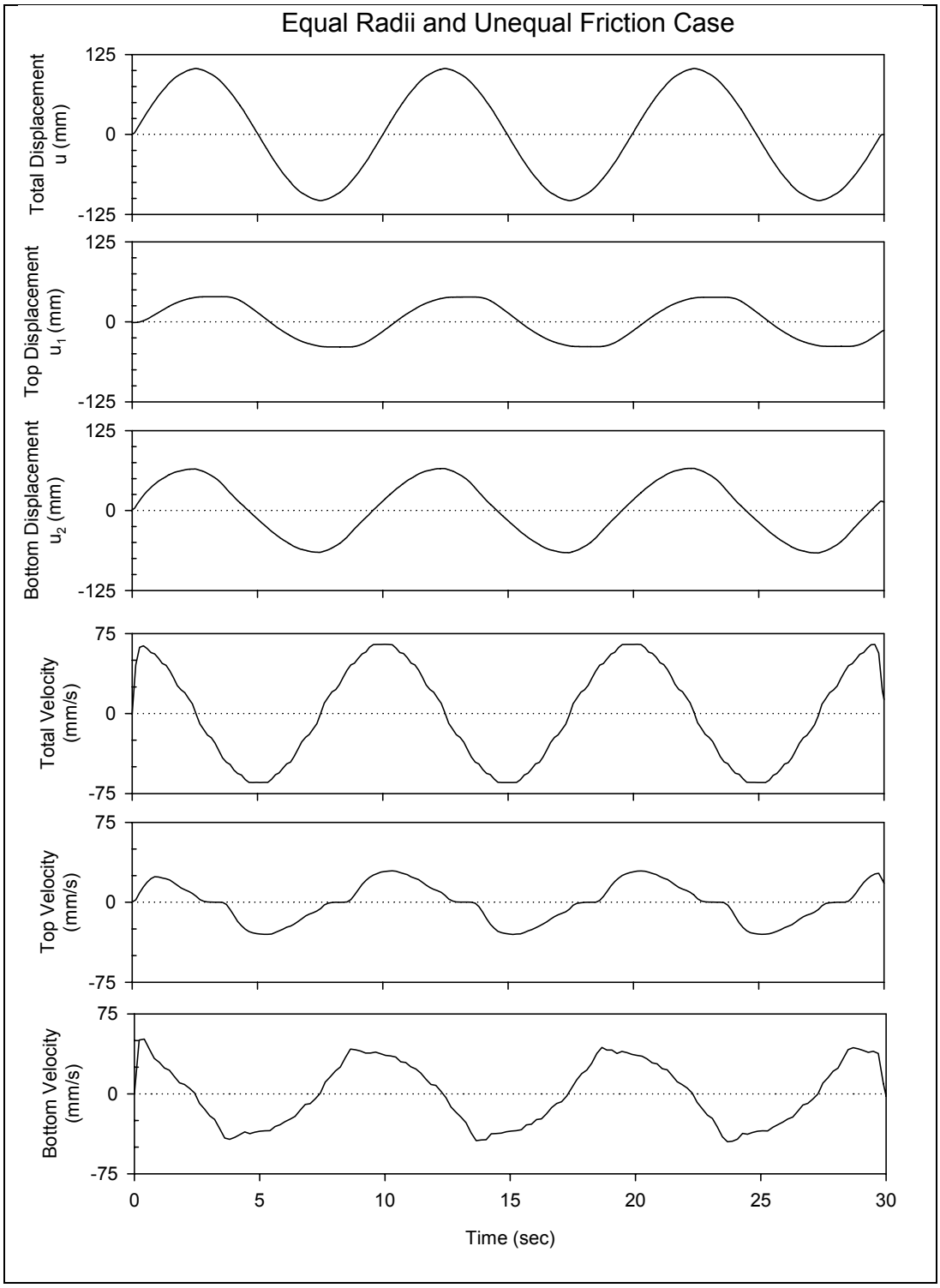

Figure 6. Histories of displacement and velocity demonstrating sliding temporarily occurring only on lower concave surface (i.e. zero velocity on top surface) upon reversal of motion

Concluding Remarks

Since sliding can occur on both the upper and lower concave surfaces, the Double Concave Friction Pendulum bearing has a displacement capacity that is substantially larger than a traditional Friction Pendulum bearing of identical plan dimensions. This key feature of the behavior results in significant savings in terms of the material cost of isolators. This may also lead to seismic isolation being a viable option in applications where very large displacement demands would have precluded its use in the past.

Moreover, there is the possibility of using upper and lower concave surfaces having different radii of curvature and coefficients of friction. There are four parameters that can be varied (R_1, R_2, μ_1 and μ_2) rather than just two (R and μ) as with the traditional Friction Pendulum bearing, thereby offering more options to optimize performance. These possibilities can be exploited to improve performance of nonstructural components or to improve performance for near source excitations. The author will examine these issues with a parametric study and shake table testing in future work.

Acknowledgements

This research was carried out under the supervision of Dr. Michael Constantinou, and primarily supported by the Earthquake Engineering Research Centers Program of the National Science Foundation, under award number EEC-9701471 to the Multidisciplinary Center for Earthquake Engineering Research. In addition, the author wishes to thank Earthquake Protection Systems Inc. for providing the tested bearing.

References

Fenz DM and Constantinou MC (2005): Behavior of the double concave Friction Pendulum bearing. Submitted for review and possible publication in *Earthquake Engineering and Structural Dynamics*.

Hyakuda T, Saito K, Matsushita T, Tanaka N, Yoneki S, Yasuda M, Miyazaki M, Suzuki A, Sawada T (2001): The structural design and earthquake observation of a seismic isolation building using Friction Pendulum system. *Proceedings, 7th International Seminar on Seismic Isolation, Passive Energy Dissipation and Active Control of Vibrations of Structures,* Assisi, Italy.

Touaillon J (1870): *Improvement in Buildings.* United States Patent Office, Letters Patent No. 99,973, February 15.

Tsai CS, Chiang TC, Chen BJ (2005): Experimental evaluation of piecewise exact solution for predicting seismic responses of spherical sliding type isolated structures. *Earthquake Engineering and Structural Dynamics*, **34**(9),1027-1046.

7

Estimation of Kinetic Friction Coefficient for Sliding Rigid Block Nonstructural Components

Cagdas Kafali

Ph.D. Candidate, School of Civil and Environmental Engineering, Cornell University

Research Supervisor: Mircea Grigoriu, Professor of Structural Engineering

Summary

The kinetic friction coefficient between a sliding rigid block and its supporting floor is estimated. The block can be used to model a broad range of nonstructural components such as free standing and unrestrained building contents, and mechanical and electrical equipments. Experimental results and theoretical considerations are used to estimate this coefficient, since the coefficient of kinetic friction cannot be measured directly. Estimates of kinetic friction coefficient are obtained using acceleration and displacement-based methods for carpet on steel interface. These estimates account implicitly for the uncertainty in experimental errors, imperfections in block-floor interfaces, and the relationship between the kinetic friction coefficient and the loading, and the block size. It is shown that most of the pairs of acceleration and displacement-based estimates of the kinetic coefficient of friction are included in the 90% probability contour of these parameters assumed to be Gaussian.

Introduction

In recent studies it has been shown that, for a facility, the financial consequences of seismic occurrences result mainly from the poor performance of its nonstructural components and systems (Gould and Griffin 2003; Kircher 2003). The seismic performance of free standing and unrestrained components, for example, mechanical and electrical equipments, depends strongly on the kinetic friction coefficient between the components and the supporting floors. However, the kinetic friction coefficients for common component-floor interfaces are not available in the literature (Soler and Singh 1984; Garcia and Soong 2003; Castiglioni 2003).

The objective of this study is to estimate the kinetic friction coefficient between a sliding rigid block and its supporting floor. The block can be used to model a broad range of nonstructural components such as mechanical and electrical equipments, free standing and unrestrained building contents. Since the coefficient of kinetic friction cannot be measured directly, experimental results and theoretical considerations are needed to estimate this coefficient. Estimates of kinetic friction coefficient are obtained for carpet on steel interface, using acceleration and displacement-based methods. It is shown that most of the pairs of acceleration and displacement-based estimates of the kinetic coefficient of friction are included in the 90% probability contour of these parameters assumed to be Gaussian random variables with the second moment properties estimated from experiments.

Dynamic Analysis of Block-Table System

Consider a free standing rigid block of mass m, which can represent a sliding nonstructural component, sitting on a shake table. Let $z(t)$ and $y(t)$ be the displacement of the shake table and of the block relative to an absolute frame whose origin corresponds to the vertical position of the block centroid, respectively, μ be the coefficient of kinetic friction between the block and the surface of the shake table, and g be the acceleration of the gravity as shown in Figure 1. Denote the displacement of the block relative to the shake table by $x(t)$, so that $y(t)=z(t)+x(t)$.

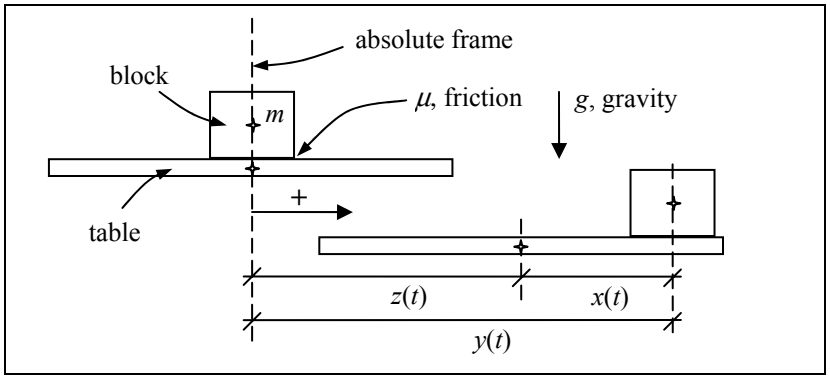

Figure 1. System of sliding block and shaking table

The equation of motion for the block is

$$\ddot{x}(t) = \begin{cases} -\ddot{z}(t) - \mu\, g\, \text{sign}(\dot{x}(t)), & \text{sliding condition} \\ 0, & \text{sticking condition} \end{cases} \tag{1}$$

where sign(b)=-1, 0, 1, for $b<0$, $b=0$ and $b>0$, respectively. The shake table acceleration used in the experiments performed at the University at Buffalo has the form

$$\ddot{z}(t) = w(t)\alpha g \sin(\upsilon t), \quad t \in [0, t_f] \tag{2}$$

where $w(t)$ is a modulation function increasing to 1 and starting at $w(0)=0$.

A computer algorithm for calculating the block relative acceleration, velocity and displacement is presented in Kafali and Grigoriu (2005). Figure 2 shows the calculated total and relative acceleration and velocity responses of the block, and the acceleration and the velocity of the shake table for μ=0.2, α=0.8, $\upsilon=2\pi T$, T=0.5 sec and t_f=3.1 T, in Eqs. 1 and 2.

The calculated steady state total block acceleration, velocity and displacement responses have zero temporal mean, and are symmetric about the time axis, under the sinusoidal excitation defined in Eq. 2 because of the symmetry of the equation of motion. On the other hand, recorded block responses exhibit drifts since the properties of the block-table interface exhibit spatial variation. To relate calculated results to experimental results, block response records need to be corrected, as shown in the following sections.

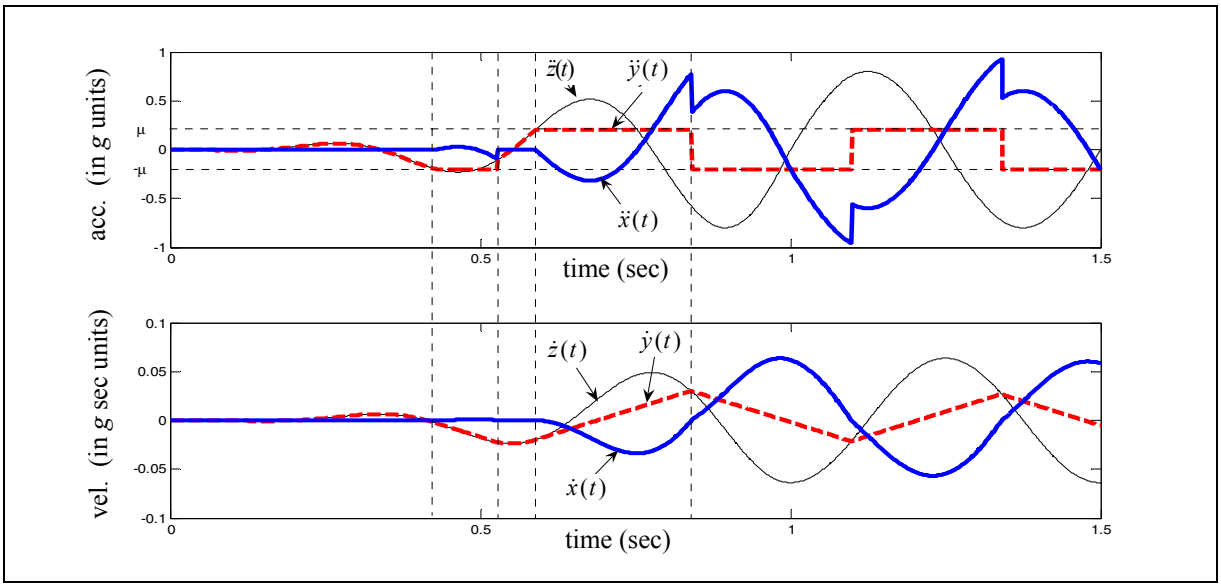

Figure 2. Algorithm

Estimation of Kinetic Friction Coefficient

The coefficient of kinetic friction μ is estimated using the maximum responses of the block obtained through experiments at the University at Buffalo, and a relationship between the maximum responses and the kinetic friction coefficient, obtained at Cornell University using theoretical considerations. The maximum absolute total acceleration response, $\max_t |\ddot{y}(t)|$, of a block subjected to the input acceleration defined by Eq. 2, is obtained using Eq. 1

$$\max_t |\ddot{y}(t)| = \begin{cases} \mu\, g, & \text{sliding condition} \\ \max_t |\ddot{z}(t)| = \alpha\, g, & \text{sticking condition} \end{cases} \tag{3}$$

It is difficult to obtain a relationship in closed form between the maximum absolute displacement response $\max_t |y(t)|$ and the kinetic friction coefficient μ. The algorithm defined in Kafali and Grigoriu (2005) is used to relate $\max_t |y(t)|$ and μ. Figure 3 shows an example of maximum total displacement versus kinetic coefficient friction curve for $\mu \in$ [0.1,0.9], α=0.8, $\upsilon=2\pi T$, T=0.5 sec, t_f=40.2 T.

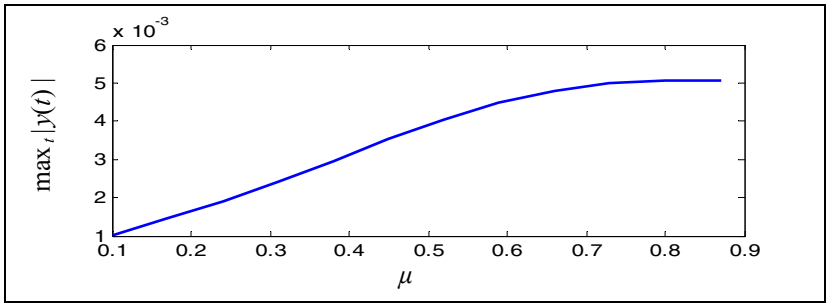

Figure 3. Relation between $\max_t |y(t)|$ and μ

Data Analysis

A series of shake table experiments on rigid blocks have been performed at the University at Buffalo to characterize the kinetic friction coefficient carpet on steel interface (explained in detail in Fathali 2005). The surface of the shake table is steel and the carpet is attached to the bottom of the blocks. The excitations are modulated unidirectional sine waves with different amplitudes and frequencies to account for the uncertainty related to the dependence of the kinetic friction coefficient on the loading. To account for the uncertainty related to the experimental errors, six nominally identical blocks are tested simultaneously for given amplitude, period pair. Two methods are used to estimate the kinetic coefficient of friction. The methods are based on acceleration and displacement records of blocks obtained in Fathali (2005).

Acceleration-Based Estimates of Kinetic Friction Coefficient: Let $a(t)$, $t \in [0,t_f]$, be the recorded acceleration time history of a block in a given test, with respect to a fixed frame. The corresponding block acceleration in calculations is denoted by $\ddot{y}(t)$. The following 4-step procedure was used to find estimates μ_{acc} of μ based on displacement records (details can be found in Kafali and Grigoriu 2005).

- Step-1: The acceleration record $a(t)$ is corrected by subtracting its temporal mean.
- Step-2: The steady state part of the corrected acceleration response record $a_{ss,c}(t)$ is obtained.
- Step-3: The maximum absolute acceleration $\max_t |a_{ss,c}(t)|$, is estimated by its most likely value from the histogram of $|a_{ss,c}(t)|$.
- Step-4: The coefficient of kinetic friction is obtained using Eq. 3.

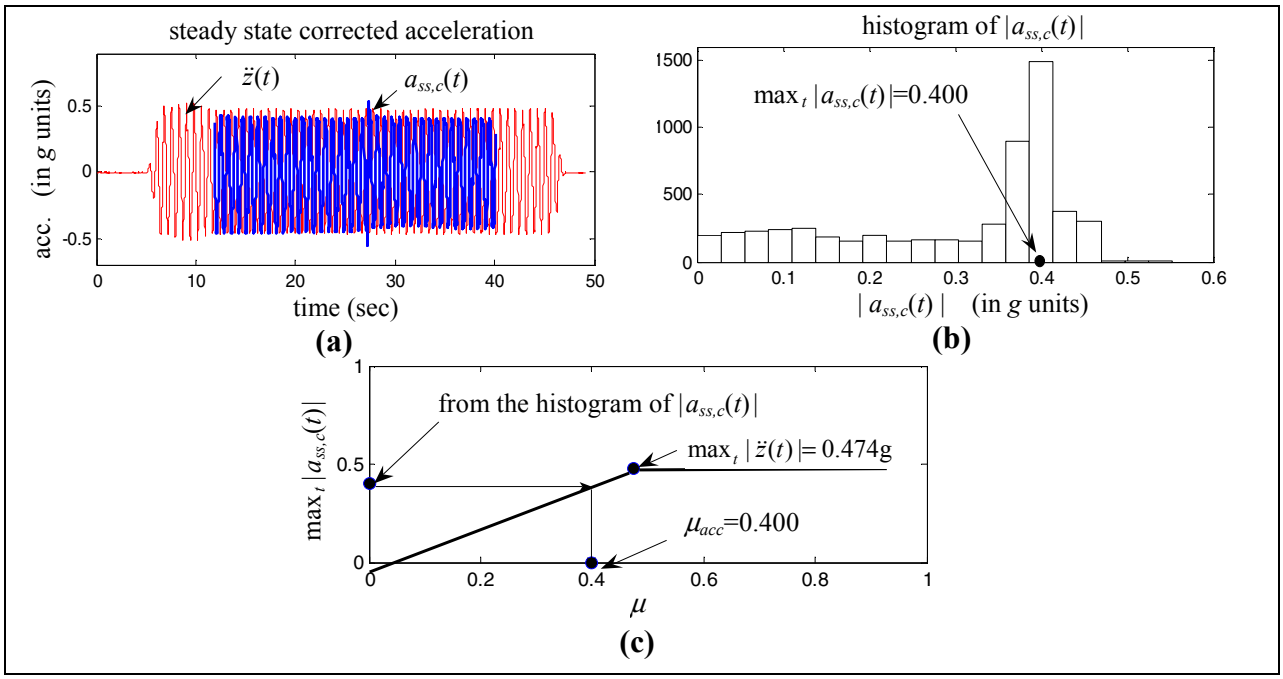

Figure 4. Acceleration-based estimation (test 65, block 1)

Displacement-Based Estimates of Kinetic Friction Coefficient: Let $d(t)$, $t \in [0,t_f]$, be the recorded displacement time history of a block in a given test, with respect to a fixed frame. The corresponding block displacement in calculations is denoted by $y(t)$. The following 4-step procedure was used to find estimates μ_{disp} of μ based on displacement records (details can be found in Kafali and Grigoriu 2005).

- Step-1: The displacement record $d(t)$ is corrected by subtracting its drift.
- Step-2: The steady state part of the corrected displacement response record $d_{ss,c}(t)$ is obtained.
- Step-3: The maximum absolute acceleration $\max_t |d_{ss,c}(t)|$, is estimated by its most likely value from the histogram of $|d_{ss,c}(t)|$.
- Step-4: The kinetic friction coefficient is obtained using the relation between $\max_t |d_{ss,c}(t)|$ and μ.

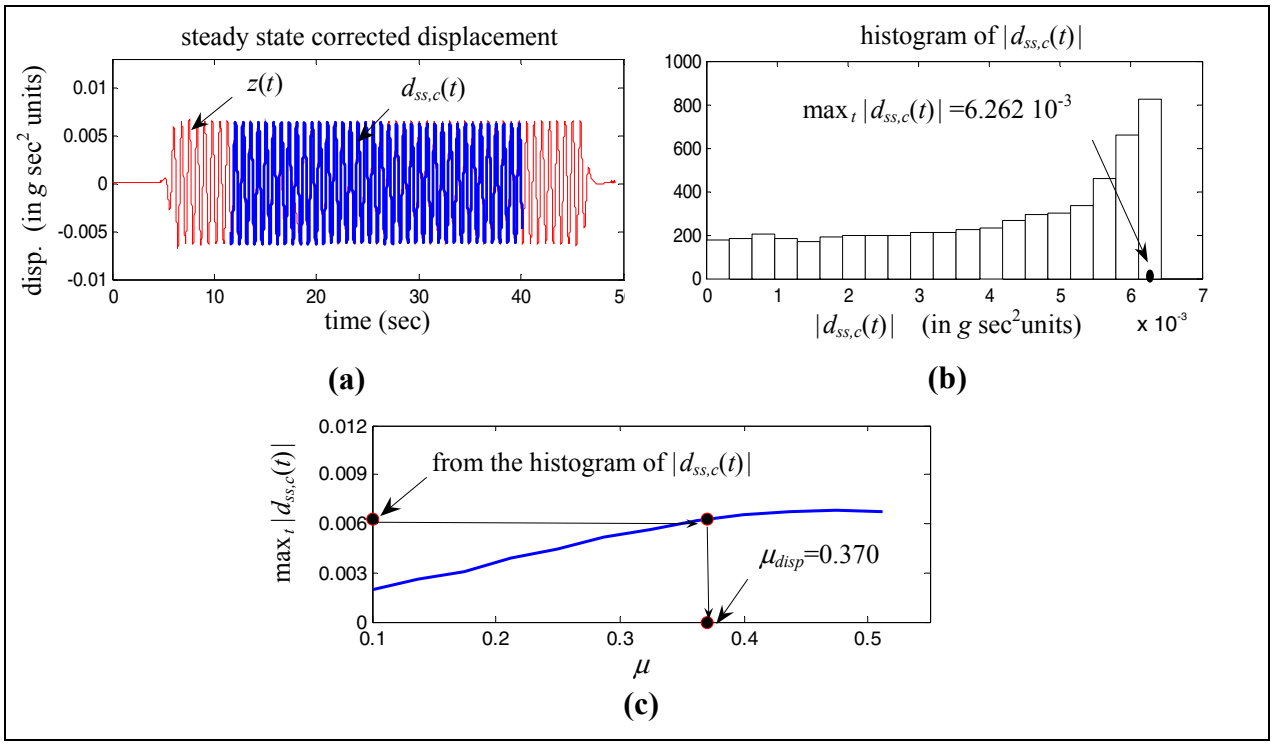

Figure 5. Displacement-based estimation (test 65, block 1)

Results

For a given interface type, the coefficient of kinetic frictions are obtained using the acceleration and displacement responses of all the blocks in each test for that interface type following the procedures described above. Figure 4 shows the (μ_{acc}, μ_{disp}) pairs obtained for carpet-steel interface. Statistics of μ_{acc} and μ_{disp} are calculated using (i) only the small blocks, (ii) only the large blocks, and (iii) all the blocks, are shown in Table 1 for carpet-steel interface.

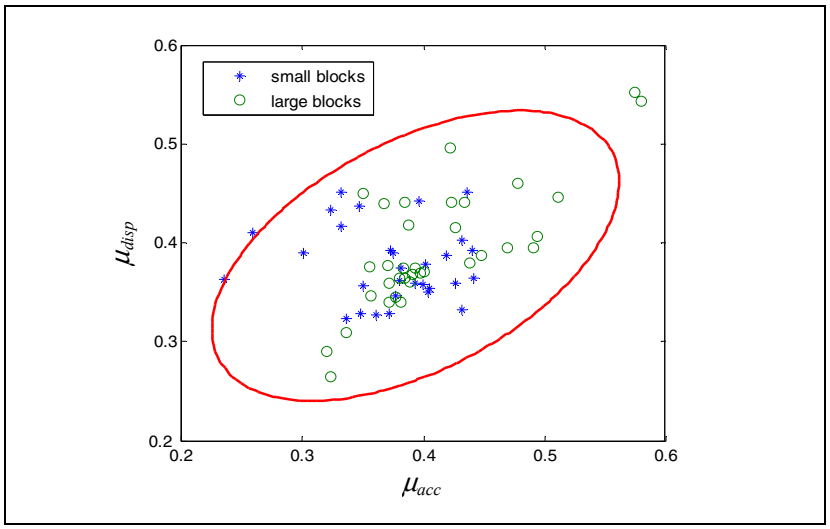

Figure 6. Friction coefficients

It is observed that the correlation between μ_{acc} and μ_{disp} obtained using the large blocks is significantly higher than the correlation obtained using the small blocks. This suggests that the estimates of μ based on small blocks have more noise than those corresponding to large blocks. However, the estimated means and the coefficients of variation are insensitive to block size. It is concluded that there is no apparent size effect in the estimates of μ_{acc} and μ_{disp}.

Table 1. Statistics of kinetic friction coefficient

	Small blocks		Large blocks		All blocks	
	μ_{acc}	μ_{disp}	μ_{acc}	μ_{disp}	μ_{acc}	μ_{disp}
Mean	0.374	0.379	0.410	0.394	0.393	0.387
Standard Deviation	0.051	0.038	0.063	0.062	0.060	0.053
Coefficient of variation	0.137	0.101	0.154	0.157	0.153	0.136
Correlation coefficient	-0.100		0.752		0.509	

Assuming that μ_{acc} and μ_{disp} are correlated Gaussian random variables with means, standard deviations and correlation coefficients given in Table 1, contour lines of the joint probability density function of μ_{acc} and μ_{disp} corresponding to 90% probability are shown in Figure 4. Most of the data points are in the 90% probability contour.

Concluding Remarks

The kinetic friction coefficient between a sliding rigid block and its supporting floor for carpet on steel interface is estimated using experimental results and theoretical considerations. Estimates of the kinetic friction coefficient are obtained using acceleration and displacement-based methods, and

account implicitly for the uncertainty in experimental errors, imperfections in block-floor interfaces, and the relationship between the kinetic friction coefficient and the loading, and the block size. It is shown that most of the pairs of acceleration and displacement-based estimates of the kinetic coefficient of friction are included in the 90% probability contour of these parameters assumed to be Gaussian random variables with the second moment properties estimated from experiments.

Acknowledgements

This research was carried out under the supervision of Dr. Mircea Grigoriu and primarily supported by the Earthquake Engineering Research Centers Program of the National Science Foundation, under award number EEC-9701471 to the Multidisciplinary Center for Earthquake Engineering Research. The author also would like to thank Prof. Harry E. Stewart of Cornell University for the comments and suggestions, and Prof. Andrew Whittaker and Saeed Fathali of University at Buffalo for providing the data.

References

Gould MJ, Griffin NC (2003): The value of seismically installing and strengthening nonstructural equipment and systems to significantly reduce business interruption losses. In *Proceedings of Seminar on Seismic Design, Performance, and Retrofit of Nonstructural Components in Critical Facilities* (*ATC-29-2*), pages 215-226, Newport Beach, CA.

Kircher CA (2003): Make dollars and sense to improve nonstructural system performance. In *Proceedings of Seminar on Seismic Design, Performance, and Retrofit of Nonstructural Components in Critical Facilities* (*ATC-29-2*), pages 109-119, Newport Beach, CA.

Soler AI, Singh KP (1984): Seismic response of a free standing fuel rack construction to 3D floor motion. *Nuclear Engineering and Design*, volume 80, pages 315-329.

Garcia DL, Soong TT (2003): Sliding fragility of block-type nonstructural components. Part 1: Unrestrained components. *Earthquake Engineering and Structural Dynamics*, volume 32, pages 111-129.

Castiglioni CA (2003): Seismic behaviour of steel storage racks. In *Proceedings of the Fourth International Conference on the Behavior of Steel Structures in Seismic Areas* (*STESSA 2003*), Naples, Italy.

Kafali C, Grigoriu M (2005): Estimation of kinetic friction coefficient for sliding rigid block nonstructural components. *Report* (*in preparation*), Multidisciplinary Center for Earthquake Engineering Research, Buffalo, NY.

Fathali S (2005): Fragility evaluation of sliding blocks. *Report* (*in preparation*), Multidisciplinary Center for Earthquake Engineering Research, Buffalo, NY.

8

Liquefaction Assessment by Energy Approach

T. Kanagalingam

Graduate Student, Department of Civil, Structural and Environmental Engineering, University at Buffalo

Research Supervisor: S. Thevanayagam, Associate Professor and MCEER Director of Education

Summary

Soil liquefaction phenomenon involves progressive intergrain contact deformation, slip, reorganization of contacts, and eventual collapse of soil skeleton. During the process leading to liquefaction, energy is continuously lost mainly along frictional contacts. Many researchers identified the cumulative energy lost up to liquefaction as a useful index for liquefaction potential assessment. This paper presents a theoretical framework for estimating the frictional energy loss along contacts. A pore pressure model is presented as a function of dissipated energy. Based on above developments and understanding, a numerical simulation model for liquefaction assessment using finite difference method is developed. The model simulates energy dissipation, pore pressure generation, pore pressure dissipation, and densification in a given soil profile. The simulation results are compared with data from centrifuge model tests.

Introduction

Liquefaction of loose, cohesionless, saturated soil deposits during earthquakes has been the subject of intensive research in geotechnical engineering over the past forty years. A significant amount of laboratory and field research has been focused on identifying the factors and mechanisms causing liquefaction. Soil liquefaction is a process involving structural collapse of the soil skeleton due to shear, with a concurrent loss of energy mainly by frictional mechanisms. The amount of frictional energy loss required to liquefy a soil depends on active intergrain contact density, confining stress, and frictional characteristics of the soil. The cumulative energy loss up to liquefaction (W_L) has been identified as a useful index for liquefaction potential assessment of soils (Nemat-Nasser and Shokooh 1979; Berrill and Davis 1985; Okada and Nemat-Nasser 1994; Figueroa et al. 1994, Thevanayagam et al. 2000; Trifunac 1995). This idea has also led to development of energy based liquefaction potential evaluation procedures (Kayen and Mitchell 1997, Green 2001) based on penetration resistances and arias intensity. This paper presents a coupled numerical model for liquefaction assessment of a saturated soil deposit with due consideration for energy dissipated in the soil due to an earthquake during seismic wave propagation, excess pore pressure generated, and associated consolidation. The results are compared against centrifuge test data.

Theory

Consider a saturated loose granular soil deposit shown in Figure 1 subjected to strong shaking at its base. Propagation of seismic waves through this soil deposit induces shear strains, frictional energy loss, and gradual increase in excess pore pressures. Concurrently, the hydraulic gradients induced by the excess pore pressures cause flow of water and changes in density in the soil layers. The coupled

effect of generation of earthquake-shear-strain-induced excess pore pressures and concurrent soil consolidation may lead to excessive and permanent shear strains and raise the excess pore pressures near the initial effective confining pressures leading to liquefaction at various depths depending on the intensity and duration of shaking, soil density, soil compressibility, and permeability characteristics. Development of a theoretical model and numerical scheme to simulate this process is valuable to study the pore pressure response of saturated soil deposits and in the assessment of its liquefaction potential.

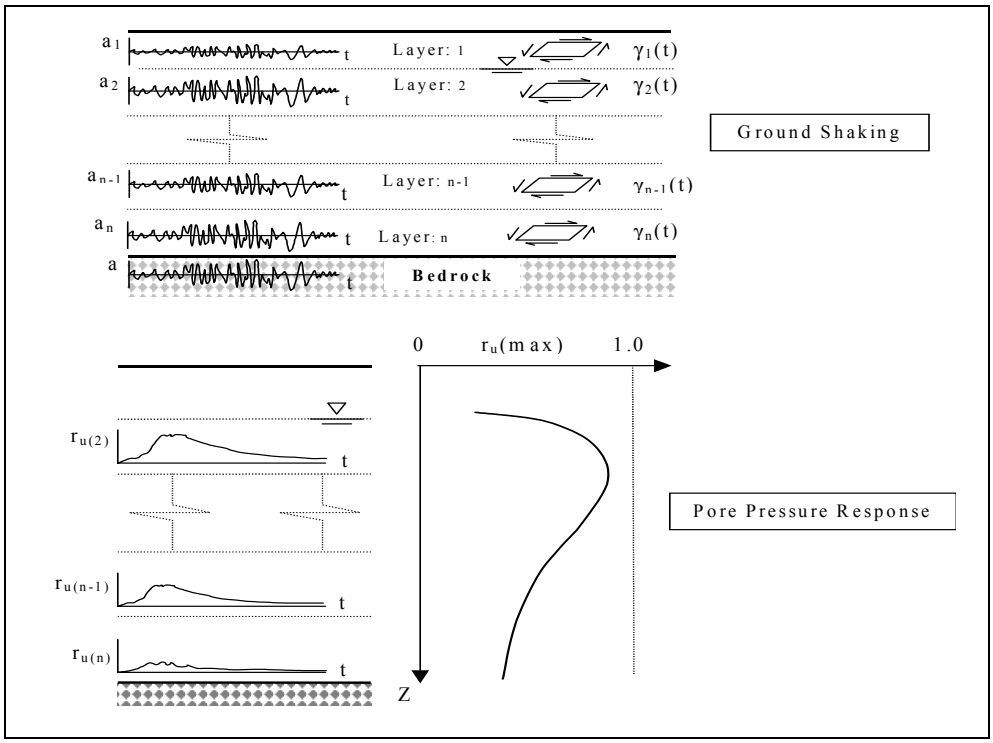

Figure 1. Pore pressure response during earthquake shaking

Wave Propagation

The governing equation for vertical propagation of shear waves through a uniform soil deposit is given by:

$$\rho \partial^2 v / \partial t^2 = G \partial^2 v / \partial z^2 + \eta \partial^3 v / \partial z^2 \partial t \qquad (1)$$

where ρ is the soil density, v is the horizontal displacement, t is time, z is the vertical coordinate, G is shear modulus, $\eta=2G\zeta/\omega$, ζ is the damping ratio, and ω is the angular frequency. For a layered soil system, solution to this equation with an appropriate shear strain dependent modulus reduction and damping relationships and appropriate boundary and soil layer interface conditions provides the strain-time history of the soil deposit at various depths (Schnabel et al. 1972; Idriss and Sun 1992).

Frictional Energy Loss

Based on an analysis of frictional loss of energy along contacts in soil clusters, using the work of Mindlin and Deresiewicz (1953), Thevanayagam et al. (2002) have shown that the incremental frictional energy loss (ΔW) per unit volume of soil due to an incremental shear strain amplitude ($\Delta\gamma$) is given by:

$$\Delta W = 1.5 \sum \mu^* (\sigma'(\Delta\gamma)) \tag{2}$$

where σ' is the current mean effective confining stress $(\sigma_1'+\sigma_2'+\sigma_3')/3$, and μ^* is the mobilized friction coefficient. The mobilized friction coefficient μ^* is given by:

$$\mu^* = \mu\left[1-\left(1-\frac{4G\left[3(1-\nu)/2G\right]^{1/3}}{3(2-\nu)\mu}\left(\frac{\alpha}{\sigma'}\right)^{2/3}\gamma\right)^{3/2}\right] \tag{3}$$

where ν is Poisson's ratio, G is shear modulus of the soil clusters, μ is full-slip contact friction coefficient, α is a packing factor that depends on cluster packing arrangements, α=1, $8^{1/2}$ and $3^{1/2}$ for simple cubic, face centered cubic, and body centered cubic packing, respectively (Thevanayagam et al. 2002). During shear, μ^* increases with increase in shear strain and reaches μ whenever full slip occurs between soil clusters or particles. Typically full slip was found to occur at less than 0.1% shear strain.

Pore Pressure Generation

Based on a large experimental database and theoretical considerations, excess pore water pressure generated due to undrained cyclic loading has been related to frictional energy loss in the soil by Thevanayagam et al. (2002):

$$r_u = 0.5\log_{10}\left(100\frac{W}{W_L}\right), \quad \frac{W}{W_L} > 0.05 \tag{4}$$

where, r_u is the excess pore pressure ratio (u/σ_0'), u is the excess pore pressure, σ_0' is the initial mean effective confining pressure, W is the cumulative energy loss per unit volume of soil under undrained loading, and W_L is the cumulative energy per unit volume required to cause liquefaction.

Coupled Flow

Considering both, the generation of excess pore pressures given by Eq.4 and the concurrent flow due to hydraulic gradients caused by the excess pore pressures, the governing equation for pore pressure distribution across the soil deposit is given by:

$$\frac{\partial u}{\partial t} = \frac{k_v}{\gamma_w m_v}\frac{\partial^2 u}{\partial z^2} + \frac{\partial u_g}{\partial t} \tag{5}$$

where k_v is the hydraulic conductivity of the soil in vertical direction; m_v is the volume compressibility of the soil; u is the excess pore water pressure at coordinate z; u_g is the excess pore pressure generated due to shaking; t=time; γ_w=unit weight of water; respectively. Seed et al. (1975)

suggest that m_v values for sands increase from its initial value m_{vo} according to the following relationship:

$$\frac{m_v}{m_{v0}} = \frac{\exp(y)}{1 + y + y^2/2} \geq 1; \qquad y = a.r_u^b; \qquad a = 5(1.5 - D_r); \qquad b = 3(4)^{-D_r} \tag{6}$$

where, m_{vo} and D_r are initial volume compressibility and relative density of soil, respectively. For silty sands, the above equation is modified by substituting an equivalent relative density $(D_r)_{eq}$ (Thevanayagam et al. 2002, 2003, Shenthan 2005) which accounts for the effect of non-plastic silts on the effective soil skeleton density, for D_r in Eq. 6 to take into account the effects of fines on volume compressibility.

Numerical Simulation

A finite difference numerical scheme was developed to implement the above equations for a level ground site subjected to strong shaking (Kanagalingam 2005). As a first-order approximation, the wave propagation equation was solved using SHAKE software (Schanabel et al. 1972; Idriss and Sun 1992) to obtain shear strain-time history. The results from the numerical simulations were compared with centrifuge test data obtained from VELACS project (Arulanandan and Scott 1993). The VELACS centrifuge test used in this comparison is referred to as Model 1 in VELACS database (Taboada and Dobry 1993; Taboada 1995). The Model 1 test was performed in a 20 cm high laminar box container at Rensselaer Polytechnic Institute (RPI) using Nevada #120 sand at 40-45% relative density and saturated with water, and tested at 50 g (Taboada 1995; Taboada and Dobry 1993). The measured soil response data for this model test are also available elsewhere (Elgamal et al. 2002, *http://geoinfo.usc.edu/gees/velacs*). The index properties of Nevada #120 sand are: e_{max}=0.894, e_{min}=0.516, G_s=2.68 (Arulmoli et al. 1992; Taboada 1995). The simulated prototype soil stratum is 10 m depth with infinite lateral extent, and seismically excited at the bottom by the same base excitation used in Model 1 test.

For numerical wave propagation simulations of the prototype soil strata, G_{max} was estimated using $G_{max}=K_{2max}.1000(\sigma')^{1/2}$. Based on available G_{max} data from resonant column test on Nevada #120 sand (Arulmoli et al. 1992), K_{2max} was calculated to be about 35. Since the centrifuge pore fluid was water, the corresponding prototype soil strata has a permeability of fifty times that of Nevada #120 sand permeated with water. The typical water permeability of Nevada #120 sand at a relative density of 40-45% is about $6.6x10^{-5}$ m/s (Arulmoli et al 1992). Therefore, in the numerical simulations the permeability of the prototype was set at $50x6.6x10^{-5}$ m/s. The m_{vo} values for Nevada sand was not readily available to the authors. Based on other available data for similar sands, m_{vo} was assumed $4x10^{-5}$ kPa^{-1} at an effective confining stress of 100 kPa (Lambe and Whitman 1969; Thevanayagam and Martin 2002). The data for energy required to cause liquefaction in Nevada #120 sand was obtained from Dief and Figueroa (2001) from specimens tested in a range of relative densities at a confining stress of 34 kPa. This data was used to obtain the values of W_L relevant for the relative densities and confining stress relevant for the prototype. Further details of the numerical simulation are presented in Kanagalingam (2005). Two separate analyses were done assuming μ values of 0.25 and 0.4, respectively, to capture the possible variations in soil frictional characteristics.

Figures 2 a-c show the comparison of experimental and numerical results for excess pore pressure-time histories at 1.25, 5.0, and 7.5 m depths, in the prototype, respectively. Results show that the numerical results are comparable to the experimental data at all depths. The numerical simulation

results for μ=0.25 is denoted as 'Analysis-1' and the results for μ=0.4 is denoted as 'Analysis-2', respectively. The numerical simulations tend to capture the measured response in general.

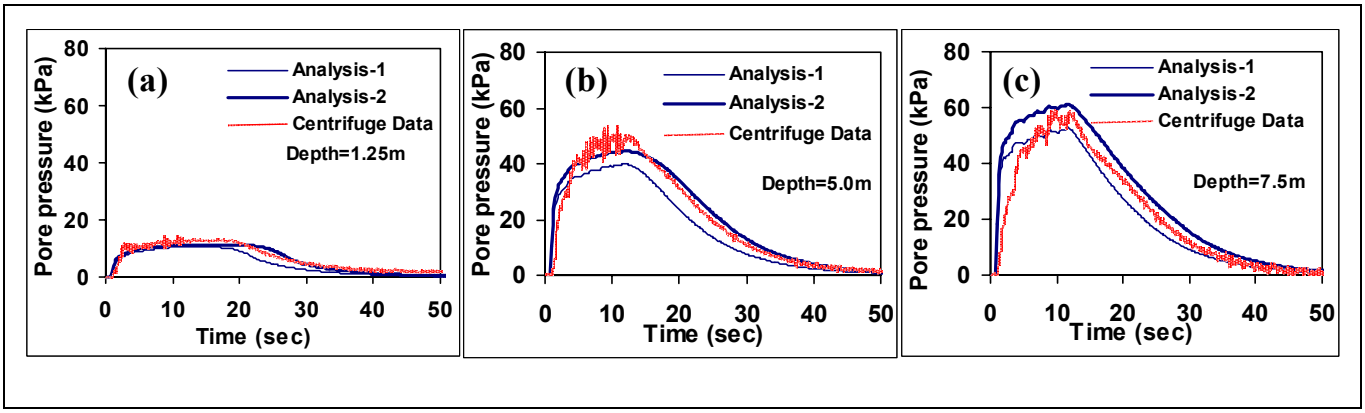

Figure 2. Excess pore pressure time histories (a) depth = 1.25 m, (b) 5.0 m and (c) 7.5 m (Analysis-1:μ=0.25 and Analysis-2: μ=0.40)

Conclusions

A simple theoretical framework for assessment of energy dissipation during seismic wave propagation, excess pore pressure generation, and concurrent consolidation in a given soil deposit due to strong earthquake motion is presented. A finite difference numerical simulation model coupled with estimation of strain-time history based on SHAKE software was developed to simulate the excess pore pressure-time history profile in a flat ground deposit. The model utilizes new developments and findings, and computes pore pressure time history data based on frictional energy loss along active contacts and coupled soil consolidation. The numerical simulation results agree well with prototype data on a 10 m deposit obtained using centrifuge model test. It is expected that the developments presented herein will advance energy based liquefaction potential assessment procedures.

Acknowledgements

This research was carried out under the supervision of Professor S. Thevanayagam, and supported by the Federal Highway Administration, National Science Foundation, United States Geological Survey, and the Multidisciplinary Center for Earthquake Engineering Research. The work was primarily supported by the Federal Highway Administration under contract number DTFH61-98-C-00094 to the Multidisciplinary Center for Earthquake Engineering Research.

References

Arulanandan K, Scott RF (1993): Editors, *Proceedings of Int. Conf. on Verification of Numerical Procedures for the Analysis of Soil Liquefaction Problems*, vol.1, Balkema, Rotterdam, The Netherlands.

Arulmoli K, Muraleetharan KK, Hossain MM, Fruth LS (1992): VALACS Laboratory Testing Program-Soil Data Report. The Earth Technology Corporation, NSF, Washington, D.C.

Berrill JB, Davis RO (1985): Energy dissipation and seismic liquefaction in sands: Revised model. *Soils and Found.*, Tokyo, 25(2), 106-118.

Dief HM, Figueroa JL (2001): Liquefaction assessment by the energy method through centrifuge modeling. *Proc., of NSF Int. workshop on earthquake simulation in Geotech. Eng.,* Xiangwu Zeng, ed., CWRU, Cleveland, OH.

Elgamal A, Yang Z, Parra E (2002): Computational modeling of cyclic mobility and post-liquefaction site response. *Soil Dynamics and Earthquake Eng.*, 22, 259-271.

Figueroa JL, Saada AS, Liang L, Dahisaria MN (1994): Evaluation of soil liquefaction by energy principles. *ASCE, J. Geotech. Eng.*, 120(9),1554-1569.

Green R (2001): Energy based evaluation and remediation of liquefiabe soils. *Ph.D. Dissertation*, Virginia Polytechnic Institute and State University, 397p.

Idriss IM, Sun JI (1992): SHAKE91: A computer program for conducting equivalent linear seismic response analyses of horizontally layered soil deposits. *User's Guide*, University of California, Davis, California.

Kanagalingam T (2005): Liquefaction resistance of granular mixes based on contact density and energy considerations. *Ph.D. Dissertation*, University at Buffalo, Buffalo, NY, *In Review.*

Kayen RE, Mitchell JK (1997): Assessment of liquefaction potential during earthquakes by arias intensity. *ASCE, J. Geotech. & Geoenv. Eng.,* 123(12), 1162-1174.

Lambe TW, Whitman RV (1969): *Soils Mechanics.* John Wiley & Sons, Inc., NY.

Mindlin RD, Deresiewicz H (1953): Elastic spheres in contact under varying oblique forces. *ASME, J. Appl. Mech.*, 327-344.

Nemat-Nasser S, Shokooh A (1979): A unified approach for densification and liquefaction of cohesionless sands in cyclic loading. *Can. Geot. J.,* 16, 659-678.

Okada N, Nemat-Nasser S (1994): Energy dissipation in inelastic flow of saturated cohesionless granular media. *Geotechnique*, 44(1),1-19.

Schnabel PB, Lysmer J, Seed HB (1972): SHAKE: A computer program for earthquake response analysis of horizontally layered sites." *Report No. EERC 72-12*, Earthquake Engineering Research Center, University of California, Berkeley, California.

Seed HB, Martin PP, Lysmer J (1975): The generation and dissipation of pore water pressures during soil liquefaction. Rep. No. UCB/EERC 75-26, Earthq. Eng. Research Ctr., UC Berkely, CA.

Shenthan T (2005): Liquefaction mitigation of silty soils using stone columns. *Ph.D. Dissertation*, University at Buffalo, Buffalo, NY, *In Review.*

Taboada V (1995): Centrifuge modeling of earthquake-induced lateral spreading in sand using a laminar box. *Ph.D. Dissertation*, Rensselaer Polytechnic Institute, Troy, NY.

Taboada VM, Dobry R (1993): Experimental results of Model No 1 at RPI. *Proc., Int. Conf. on Verification of Numerical Procedures for the Analysis of Soil Liquefaction Problems,* K. Arulanandan and R. F. Scott, eds., Balkema, Rotterdam, The Netherlands, 1, 3-17.

Thevanayagam S, Liang J, Shenthan T (2000): A contact index for liquefaction potential analysis of silty/gravely soils. *EM2000, Proc. 14th ASCE EMD Spec. Conf.,* Tassoulas, ed., Austin, Texas.

Thevanayagam S, Martin GR (2002): Liquefaction in silty soils-screening and remediation issues. *Soil Dynamics and Earthq. Eng.,* 22, 1035-1042.

Thevanayagam S, Kanagalingam T, Shenthan T (2002): Contact density – confining stress – energy to liquefaction. *Proc. 15th ASCE Eng. Mech Conf.* Columbia Univ., Paper #428.

Thevanayagam S, Shenthan T, Kanagalingam T (2003): Role of intergranular contacts on mechanisms causing liquefaction and slope failures in silty sands. *Final Report*, USGS Award No. 01HQGR0032 and 99HQGR0021; US Geological Survey, Department of Interior, USA, *http://erp-web.er.usgs.gov/reports/abstract/2001/pt/01hqgr0032-report.pdf*, 396p.

Trifunac M (1995): Empirical criteria for liquefaction in sands via standard penetration tests and seismic wave energy. *J. Soil Dyn. and Earthq. Eng.*, 14, 419-426.

9

A Design Procedure for Liquefaction Mitigation of Silty Soils Using Dynamic Compaction

Rafeek G. Nashed

Ph.D. Candidate, Department of Civil Structural and Environmental Engineering, University at Buffalo

Research Supervisor: S. Thevanayagam, Associate Professor and MCEER Director of Education

Summary

Remediation of liquefiable loose granular sand and non-plastic silty sand deposits during seismic loading is a major problem in geotechnical earthquake engineering. Sand deposits densified by dynamic compaction (DC) are more resistant to liquefaction, and have performed well during earthquakes. Silty sand deposits may also be densified using DC supplemented with pre-installed wick drains. Current design methods of DC depend mainly on expensive field trials. This paper presents a set of simplified design charts and procedures to determine the densification achievable during ground improvement of sands and non-plastic silty sands using DC supplemented with pre-installed wick drains. The methodology is based on a model for performance of soil deposits during dynamic compaction using energy principles governing soil liquefaction and soil densification by consolidation. Design example is also presented.

Introduction

A number of different densification techniques have been developed to mitigate liquefaction in loose saturated granular soils. Dynamic compaction is among the most field proven and commonly used techniques (Figure 1a). The DC technique involves high-energy impacts to the ground surface by systematically dropping heavy weights of 5 to 35 Mg from heights ranging from 10 to 40 m on a pre-designed impact grid at 4 to 15 m spacing to compact the underlying ground using heavy crawler cranes. Soil densification results due to ground vibrations from the application of high-levels of energy at the ground surface (Menard and Broise 1975; Lukas 1995). It also causes an increase in lateral effective stresses. Sand deposits densified by DC are more resistant to liquefaction, and have performed well during earthquakes. Silty sand deposits appear to densify well during DC when supplemented with closely spaced pre-installed wick drains (Dise et al. 1994) (Figure 1b). Based on past experience, the depth of influence d_{max} to impact energy for various soil types (Lukas 1986, 1995) is given by:

$$d_{\max} = n\sqrt{WH} \tag{1}$$

where W is the dropped weight in Mg, and H is the height of drop in meters. The value of n ranges from 0.35 to 0.6 depending on soil type. Higher values are applicable for coarse grain soils with low degree of saturation. Low values are applicable for soils with low permeability and high water content.

Current practice for liquefaction mitigation design, suitability assessment, and determination of optimum field operation parameters for DC technique relies mainly on field pilot tests and past experience based on case histories. In the case of non-plastic silty soils, case histories of successful ground improvement are scarce. In many cases, post-improvement penetration resistance measurements based on field trials are compared against design penetration resistance values required to resist liquefaction to determine the field DC operational parameters and level of treatment required. Attempts have also been made to use energy imparted DC as a basis for ground improvement design (Lukas 1995; Green and Mitchell 2004). Typical average applied energy per cubic meter of soils during ground improvement works by DC is about 200 to 250 kJ/m^3 for pervious coarse grained soils and 250 to 350 kJ/m^3 for semi-pervious soils. This corresponds to about 30 to 60% of the standard proctor energy per cubic meter of soil. For both sands and silty sand sites, at present, there are no detailed analytical procedures available to analyze the effects of field DC operational parameters and soil conditions to determine the densification and the degree of improvement achievable in the field and design against liquefaction.

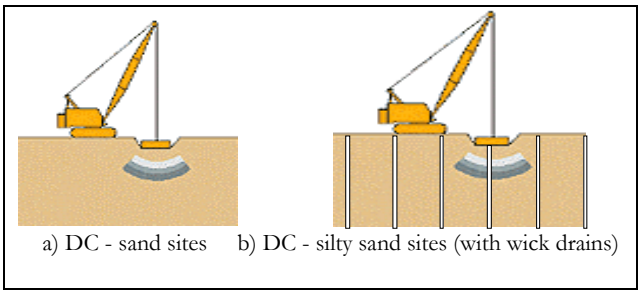

Figure 1. Dynamic compaction

This paper presents the results from a recent numerical simulation tool developed for the analysis of ground performance during DC and a guideline for liquefaction mitigation design using DC in sands and silty sands, supplemented with pre-installed wick drains taking into consideration site-specific soil conditions.

Background

It is recognized in the literature that liquefaction is a process involving energy dissipation due to frictional loss along grain contacts during cyclic loading leading to collapse of the soil structure and that this knowledge can be applied to develop methods for liquefaction mitigation design applications (Berrill, and Davis 1985; Figueroa et al. 1994; Thevanayagam et al. 2000; Green and Mitchell 2004). The energy required to cause liquefaction mainly depends on the density of packing of the grains and confining stress. If the energy delivered to a deposit by an earthquake exceeds the energy required to cause liquefaction per unit volume of soil, the soil liquefies. It is also recognized that during

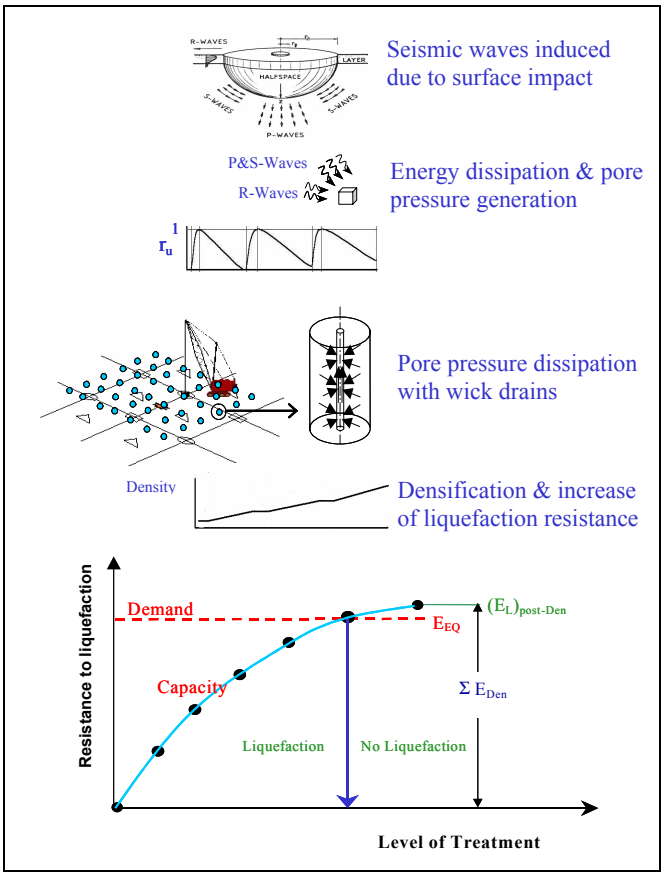

Figure 2. DC densification and design process

ground improvement works repeated ground vibrations induced by DC cause rise in pore water pressures. If the energy delivered by DC exceeds the energy required to cause liquefaction, soil approaches liquefaction. Concurrent soil consolidation results in a highly denser arrangement of particles and the soil resistance to liquefaction increases (Figure 2). Repeated applications of DC may help increase the soil density sufficiently to resist liquefaction due to a given earthquake. The design objective is to determine the level of improvement required to increase the resistance of the soil to a state which requires more energy to induce liquefaction than what might be available throughout a design earthquake.

Numerical Simulation Model

Impact Energy Radiation and Pore Pressure Development

Consider DC impact as shown in Figure 2. The energy delivered at the impact zone by the falling weight propagates through the surrounding soil as body waves and surface waves (Rayleigh waves). It has been shown that, as a first order approximation, the energy loss per unit volume of soil due to these Rayleigh waves w_R and body waves w_B, respectively, are given by (Shenthan et al. 2004):

$$w_R(r,z) = F(0.67WH)\frac{\alpha e^{-2\alpha r}}{\pi r} \quad \text{, and} \quad w_B(r,z) = (0.33WH)\frac{\alpha e^{-2\alpha R}}{\pi R^2} \tag{2}$$

where, α is the attenuation coefficient due to material damping, $R = \sqrt{(r^2+z^2)}$, F is an integral function (Shenthan et al. 2004), and r and z are radial and vertical coordinates from the center of the impact surface, respectively. The cumulative energy loss at any point is given by:

$$w_c = w_R + w_B \tag{3}$$

Based on a large experimental database and theoretical considerations, excess pore water pressure generated due to undrained cyclic loading of saturated sands and non-plastic silty soils has been related to frictional energy loss in the soil (Thevanayagam et al. 2003):

$$r_u = 0.5\log_{10}\left(100\frac{w_c}{w_L}\right), \quad \frac{w_c}{w_L} \rangle 0.05 \tag{4}$$

where, r_u is the excess pore pressure ratio (u/σ_o'), σ_o' is the initial mean effective confining pressure, w_c is the cumulative energy loss per unit volume of soil, and w_L is the energy per unit volume required to cause liquefaction. Assuming this relationship holds true for loading due to Raleigh and body waves as well, impact-induced excess pore pressure at any point in the soil surrounding the impact zone shown in Figure 2 can be obtained by substituting Eq. 3 for w_c in Eq. 4.

Pore Pressure Dissipation and Densification

Impact-induced pore pressure generation, dissipation, and soil densification around the impact zone is a coupled flow problem. The governing equation for pore pressure dissipation in the soil is:

$$\frac{\partial u}{\partial t} = C_r\left[\frac{\partial^2 u}{\partial r^2} + \frac{1}{r}\frac{\partial u}{\partial r}\right] + C_v\frac{\partial^2 u}{\partial z^2} + \frac{\partial u_L}{\partial t} \tag{5}$$

where u is excess pore water pressure, u_I is the instantaneous excess pore pressure due to surface impact and C_r and C_v are the coefficients of consolidation in the radial and vertical directions, respectively. The excess pore pressures due to impact are assumed to be induced instantaneously. Volumetric densification of a soil element due to excess pore pressure dissipation may be obtained by:

$$\varepsilon_v = \int m_v . d\sigma' \tag{6}$$

where, ε_v is the volumetric strain, and σ' is the mean effective confining pressure. Seed et al. (1975) suggest that m_v values for sands increase from its initial value according to the following relationship, and do not decrease from the highest value obtained:

$$\frac{m_v}{m_{v0}} = \frac{\exp(y)}{1+y+y^2/2} \geq 1; \qquad y = a.r_u^b; \qquad a = 5(1.5 - D_r); \qquad b = 3(4)^{-D_r} \tag{7}$$

where, m_v and D_r are initial volume compressibility and relative density of soils, respectively. For silty sands, the above equation is modified by substituting $(D_r)_{eq}$ (Thevanayagam et al. 2003) which accounts for the effect of non-plastic silts on the effective soil skeleton density, for D_r in Eq. 7 to take into account the effects of fines on volume compressibility (Shenthan 2005). Typical values for m_{v0} are adopted from Thevanayagam et al. (2001).

A finite difference scheme was developed to implement the above equations. This simulation model was found to simulate observed ground performance and post-improvement soil densities for a number of DC case histories both in sand deposits (without wick drains) and non-plastic silty soils deposits supplemented with wick drains. Details of these case history comparisons can be found in Nashed et al. (2004).

Simplified Design Charts

Based on the success of the above simulation model, additional studies were conducted to develop simplified design charts to obtain the relationships between pre- and post-improvement soil densities for various uniform soil sites containing sands to non-plastic silty soils improved by DC preinstalled with or without wick drains. For convenient field applications, the results were converted in a form to present them in terms of equivalent pre- and post-improvement normalized clean sand SPT blow counts $(N_1)_{60cs}$ (Nashed 2005). Figure 3 shows an example design chart. For all simulations, the impact grid pattern involved a single pass involving three phases of impact as shown in Figure 4. WH, S, N_I, wick drain spacing S_w, wick drain size d_w,

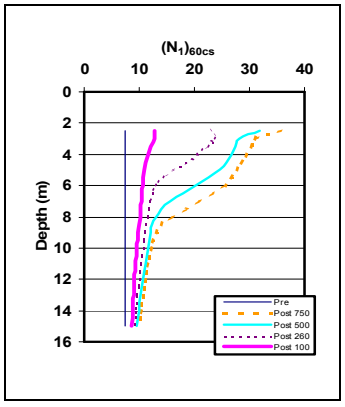

Figure 3. Pre- and post-improvement $(N_1)_{60cs}$

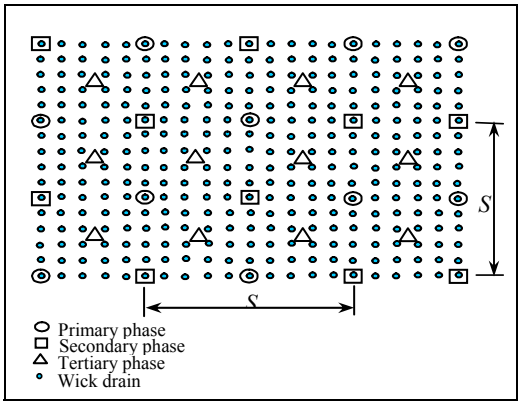

Figure 4. DC impact grid pattern

and time cycle between impacts T were varied for each simulation. Groundwater level was assumed to be at 2.0 m depth from impact surface.

Liquefaction Mitigation Design Example

Consider a silty sand site with a pre-improvement normalized SPT blow count $(N_1)_{60}$ profile as shown in Figure 5a. The soil at this example site has a non-plastic silt content of 25% and hydraulic conductivity (k) of $1x10^{-7}$ m/s. Groundwater level is at 2.0 m below ground surface. The $(N_1)_{60}$ values were corrected to obtain the equivalent clean sand blow count $(N_1)_{60cs}$ using $(N_1)_{60cs}=A+B(N_1)_{60}$, where A = 0.0 and B =1.0 for $FC \leq 5$ % by weight; A =5.0 and B =1.2 for $FC \geq 35$ %. For FC between 5 and 35%, A =exp [1.76-(190/FC^2)] and B =[0.99+($FC^{1.5}$/1000)], where FC =fines content (NCEER 1997). The $(N_1)_{60cs}$ profile is shown in Figure 5b.

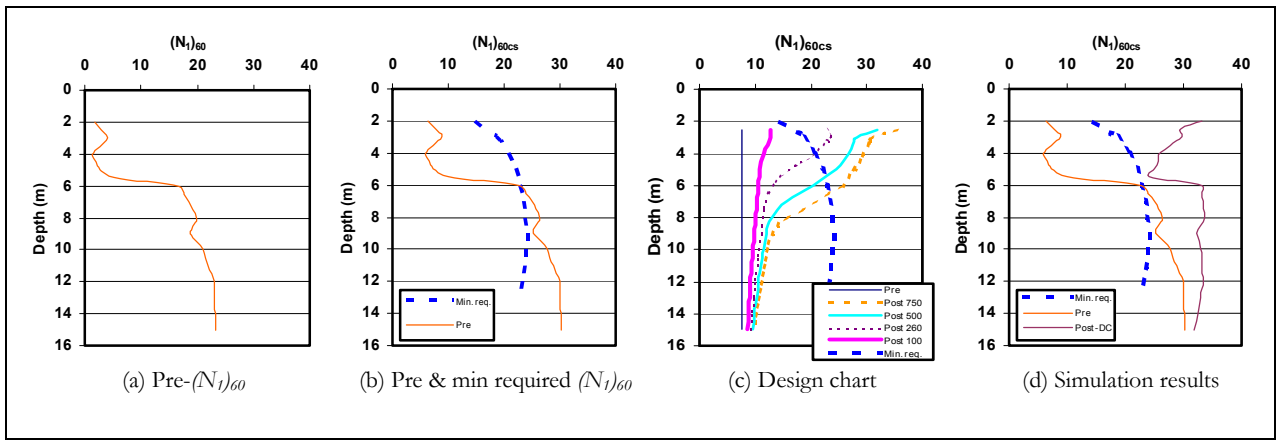

Figure 5. Design example

Based on liquefaction potential analysis of this site using liquefaction screening charts based on SPT blow counts (NCEER 1997), the soil at 2.0 to 6.0 m depth is liquefiable for a design earthquake of M = 7.5 and a_{max} = 0.25g. The minimum required $(N_1)_{60cs}$ profile to resist liquefaction at this site is shown in Figure 5b. For liquefaction mitigation design purposes using the design charts, the average $(N_1)_{60cs}$ for the liquefiable layer from 2 to 6 m depth is estimated to be about 7.5. Figure 5c shows the design chart for post-improvement $(N_1)_{60cs}$ profile for a uniform site with a pre-improvement $(N_1)_{60cs}$ value of 7.5, k = $1x10^{-7}$ m/s, N_I = 12, T = 2 min, S_w = 1.5 m, d_w= 5 cm, and S = 15 m. Also shown in this figure is the minimum required post-improvement $(N_1)_{60cs}$ profile for this site. Based on this figure, DC using 750 Mg.m energy level would increase the post-improvement $(N_1)_{60cs}$ profile of the top 2 to 6 m of soil beyond the minimum required $(N_1)_{60cs}$ to mitigate liquefaction of this liquefiable soil at the site.

Additional numerical simulations were conducted for the site using 750 Mg.m energy level. The post-improvement $(N_1)_{60cs}$ profile is shown in Figure 5d, along with the pre-improvement $(N_1)_{60cs}$ profile and the minimum required $(N_1)_{60cs}$ profile. The post-improvement $(N_1)_{60cs}$ profile exceeds the minimum required $(N_1)_{60cs}$ profile.

Concluding Remarks

A simplified design procedure and design charts for the determination of field operational parameters for liquefaction mitigation of sands and non-plastic silty soils by DC with pre-installed wick drains are presented. These design charts are based on a model for performance of ground during DC using the energy principals governing liquefaction resistance of soils and soil densification by consolidation. The verification of this model using case histories is presented elsewhere. The design procedure is illustrated using an example problem. The design charts and procedure presented herein are expected to advance the use of DC combined with pre-installed wick drains to mitigate liquefaction potential in non-plastic silty soils and help judicial choice of field trials for verification of the design.

Acknowledgements

This research was carried out under the supervision of Professor S. Thevanayagam, and primarily supported by the Federal Highway Administration, under contract number DTFH61-98-C-00094 to the Multidisciplinary Center for Earthquake Engineering Research.

References

Berrill JB, Davis RO (1985): Energy dissipation and seismic liquefaction in sands: Revised model. *Soils and Found.*, Tokyo, 25(2), 106-118.

Dise K, Stevens MG, Von Thun JL (1994): Dynamic compaction to remediate liquefiable embankment foundation soils. *ASCE*, *Geotech. sp. pub.*, No. 45, 1-25.

Figueroa JL, Saada, AS, Liang L, Dahisaria MN (1994): Evaluation of soil liquefaction by energy principles. *ASCE*, *J. Geotech. Eng.*, 120(9), 1554-1569.

Green R, Mitchell JK (2004): Energy-based evaluation and remediation of liquefiable soils. Geotrans 2004, *ASCE*, *Proc. Geotech. Eng. for transportation projects*, 1961-1970.

Lukas RG (1986): Dynamic compaction for highway construction, Vol. 1, Design and construction guidelines. *Rep. No. FHWA/RD86/133*, Federal Highway Admin.

Lukas RG (1995): Dynamic compaction. *Report No. FHWA-SA-95-037,* Federal Highway Admin.

Menard L, Broise Y (1975): Theoretical and practical aspects of dynamic consolidation. *Geotechnique*, 25(1), 3-18.

Nashed R, Thevanayagam S, Martin GR, Shenthan T (2004): Liquefaction mitigation in silty soils using dynamic compaction and wick drains. *Proc. 13th World Conf. on Earthq. Eng.*, Vancouver, Canada, Paper No. 1951.

Nashed R (2005): Liquefaction mitigation of silty soils using dynamic compaction. *Ph.D. Dissertation*, University at Buffalo, Buffalo, NY, In Review.

NCEER (1997): *Technical Report NCEER-97-0022,* Proceedings of the NCEER Workshop on Evaluation of Liquefaction Resistance of Soils, 1-40.

Seed HB, Martin PP, Lysmer J (1975): The generation and dissipation of pore water pressures during soil liquefaction. *Report No. UCB/EERC 75-26*, UC Berkeley Earthq. Engrg. Res. Center.

Shenthan T, Nashed R, Thevanayagam S, Martin G R (2004): Liquefaction mitigation in silty soils using composite stone columns and dynamic compaction. *J. Earthq. Eng. and Eng. Vibr.*, 3 (1).

Shenthan T (2005): Liquefaction mitigation in silty soils using composite stone column. *Ph.D. Dissertation*, University at Buffalo, Buffalo, NY, In Review.

Thevanayagam S, Liang J, Shenthan T (2000): A contact index for liquefaction potential analysis of silty/gravely soils. *ASCE, EM2000*, *Proc. 14th EMD Spec. Conf.,* Tassoulas, ed., Austin, Texas.

Thevanayagam S, Martin GR, Shenthan T, Liang J (2001): Post-liquefaction pore pressure dissipation and densification in silty soils. *Proc. 4th Int. Conf. on Recent Adv. in Geotech. Earthq. Eng. and Soil Dyn.*, San Diego, CA, Paper No. 4.28.

Thevanayagam S, Shenthan T, Kanagalingam T (2003): Role of intergranular contacts on mechanisms causing liquefaction and slope failures in silty sands. *USGS Report*, *http://erp-web.er.usgs.gov/reports/abstract/2001/pt/01hqgr0032-report.pdf*, US Geological Survey.

10

Design Applications for Controlled Rocking System Retrofit Approach

Michael Pollino

Ph.D. Candidate, Department of Civil, Structural and Environmental Engineering, University at Buffalo

Research Supervisor: Michel Bruneau, Professor and MCEER Director

Summary

Other components of this research have shown that allowing rocking of bridge steel truss piers with passive energy dissipation devices implemented at the base can be an effective retrofit approach. However, to ensure that the system's performance meets objectives, a number of constraints must be respected. The constraints include maximum displacements, ductility demands, maximum dynamic forces, and self-centering limits. A systematic, performance based design method is introduced that uses a graphical approach, following capacity design principles. Using the graphical approach, design "solution spaces" are produced that are an effective visual aid showing the trends in system response. Design solution space results are presented for a range of system parameters.

Introduction

Many of the existing steel bridges in the U.S. were built at a time when seismic resistance was not considered in the design or construction of the bridge, or was considered at a level significantly less than adequate by today's standards. Recent earthquakes such as the 1989 Loma Prieta and 1994 Northridge in California, and the 1995 Kobe earthquake in Japan, have demonstrated the need for improved methods for the design and construction of highway bridges to withstand seismic force and displacement demands. These earthquakes, as well as recent research, have exposed several deficiencies in the design and detailing of structural elements in steel bridges to resist earthquake excitation. Deficient elements in existing large steel bridges include the built-up, lattice members (Lee and Bruneau 2004), their connections (Ritchie et al. 1999) and the anchorage connections. Retrofit of these elements to resist seismic demands elastically is an option, but it can be very costly and gives no assurance of performance beyond the elastic limit. Also, span collapses or significant damage from those earthquakes (particularly Kobe) have left many large lifeline bridges unusable until repairs were made, contributing to substantial losses to the local economy. Highway bridges deemed critical in the response and recovery efforts following a major earthquake (a.k.a. lifeline bridges) need to remain operational after an earthquake, requiring the bridge to respond in a mostly elastic manner with little to no residual displacements. Cost effective retrofit techniques that are able to provide desirable seismic performance are needed.

Recent analytical investigations of a seismic retrofit approach that allows bridge steel truss piers to uplift and rock on their foundations have found the system able to provide satisfactory seismic performance in certain cases with a more limited retrofit effort compared to other alternatives

(Pollino and Bruneau 2004). This approach uses specially detailed, steel yielding devices (buckling-restrained braces) implemented at the uplifting location to control the rocking response. A sketch of a retrofitted pier is shown in Figure 1.

These devices can be calibrated (and/or existing pier properties modified) to control pier response and to meet performance objectives. However, to ensure that satisfactory seismic performance is achieved, a number of design constraints must be identified and a systematic design procedure formulated following capacity-based design principles. The design constraints and systematic, graphical design approach are presented here. The graphical design approach establishes boundaries of compliance and non-compliance of the design constraints, with respect to two key design parameters, producing design solution "spaces", similar to that done by Sarraf and Bruneau (1998).

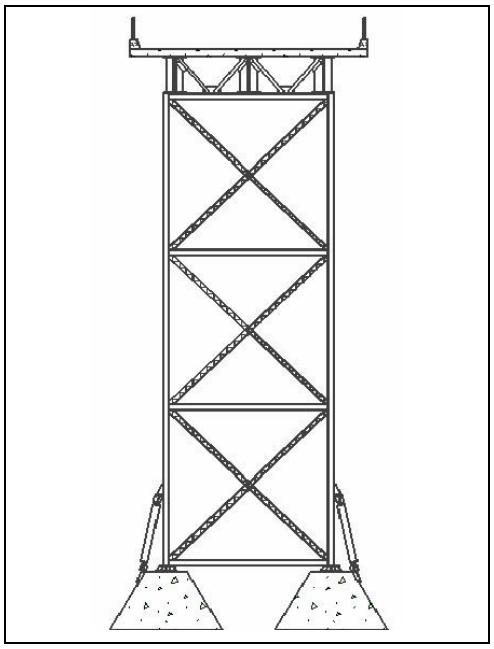

Figure 1. Retrofitted truss pier using controlled rocking approach

Design Constraints and Set-up of Graphical Solution Spaces

Drift, device ductility, strength, velocity, and self-centering limits have been identified as constraints for achieving satisfactory seismic performance. Many system properties (in addition to the buckling-restrained braces) affect the response of the controlled rocking system; including the pier aspect ratio (h/d), lateral stiffness (k_o) and strength, however it is desirable to not modify the existing pier elements to limit the retrofit effort. The buckling-restrained brace's (BRBs) cross-sectional area (A_{brb}) and effective length (L_{brb}) are used as the two key design parameters. They were chosen to limit the retrofit effort and because they control two influential system response parameters, the post-uplift stiffness (k_r) and system strength (P_y). Therefore, each design constraint is written in terms of A_{brb} and L_{brb} to establish each constraint's boundary lines in the design plots.

(1) Pier Drift

To illustrate the design procedure, two displacement limits are imposed here. The first is set to limit undesirable P-Δ effects on seismic behavior. This limit is based on the dynamic analysis of SDOF systems with various hysteretic relationships and is taken from the *NCHRP 12-49 Recommended LRFD Guidelines for the Seismic Design of Highway Bridges* (ATC/MCEER 2003). The second limit, to ensure stability against overturning, is set to prevent displacement of the center of mass from exceeding half of the base width (d/2) with a large factor of safety since this is the point of overturning. A safety factor of 5 is recommended. The smaller one of these limits is used.

Methods for determining the expected lateral pier displacement is discussed in Pollino and Bruneau (2004). Writing this constraint in terms of A_{brb} and L_{brb}, constraint (*1*) boundary line is shown on a typical design plot in Figure 2. Either displacement constraint can typically be satisfied by increasing A_{brb} and/or decreasing L_{brb}, as seen in the figure. This constraint is easily satisfied for the large displacement limits and pier properties considered here.

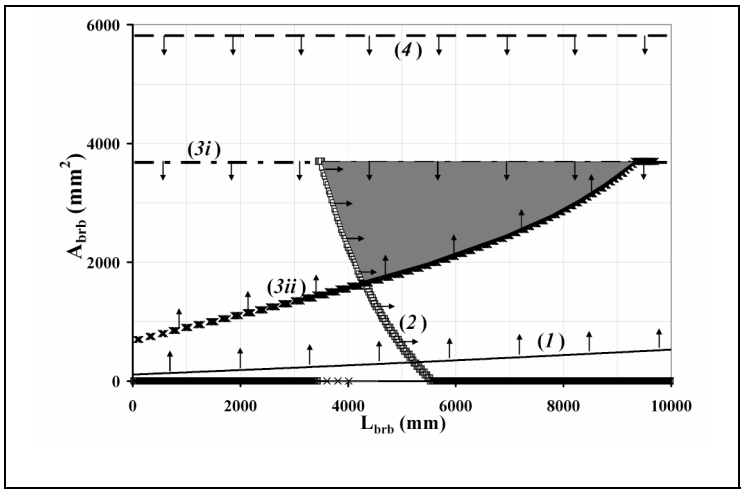

Figure 2. Typical design plot with constraint lines and solution space

at(2) Ductility Demands on Buckling-restrained Brace

Limits on the inelastic strain demands of the buckling-restrained brace are set to ensure that it behaves in a stable, predictable manner. These limits should be based on engineering judgment and experimental test data on the ultimate inelastic cyclic response of the brace. An allowable strain of 1.5% in the buckling-restrained brace is used here corresponding to a seismic demand representing a maximum credible earthquake (MCE) with 3% probability of exceedance in 75 years, as defined by the NCHRP 12-49 document (ATC/MCEER 2003). This is a modest level of strain for most structural steels and some buckling-restrained braces have been shown, through experimental testing, to develop twice this strain level with very stable hysteretic behavior (Iwata et al. 2000). Assuming a rigid foundation, brace elongation is equal to the uplifting displacement of the pier leg. A boundary line for constraint (*2*) is shown in Figure 2 and this constraint can be satisfied most effectively by increasing L_{brb}, as seen in the figure.

(3) Maximum Dynamic Forces in Existing Members and Connections

The capacity of steel truss bridge piers, in terms of maximum allowable forces, can be limited by many mechanisms discussed previously. Capacity design procedures and conservative estimates of maximum force demands are needed to ensure that non-ductile elements can remain elastic and that all inelastic action occurs in the specially detailed, ductile structural elements. A method is proposed here that creates an "effective" static base shear that can be used to evaluate the adequacy of the pier's lateral bracing members followed by a method to determine the ultimate demands placed on the pier legs and foundation. For each case, dynamic amplification factors are introduced as a result of the excitation of the pier's vertical modes of vibration during impact to and uplift from the foundation. The dynamic amplification factors depend on the impulsive nature of the transfer of loads during pier rocking and a procedure to calculate these factors is presented in Pollino (2004).

Strength of existing bridge elements will vary from bridge-to-bridge and partial strengthening may be required in some cases.

(i) Effective Lateral Shear Demand

The effective base shear caused by the earthquake is determined by the static yield force amplified to account for the increased demand caused by dynamic effects as a result of uplift from the foundation. The transfer of lateral and gravitational loads through the truss pier is depicted in Figure 3. The maximum allowable base shear ($P_{u,allow}$), is taken here to equal 0.5w. Limiting the buckling-restrained brace strength, $A_{brb}F_{ybrb}$, to an acceptable level or strengthening of the weak

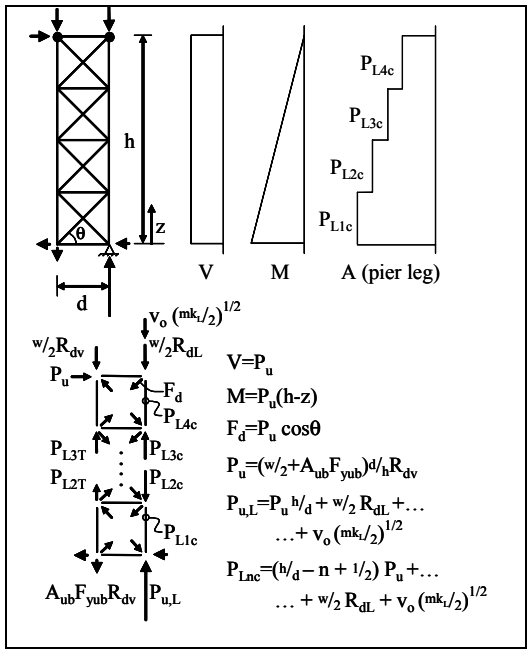

Figure 3. Transfer of lateral and gravitational loads through truss pier

elements along the lateral load path (increasing $P_{u,allow}$) can satisfy this constraint. Thus this constraint line is seen in Figure 2 to be independent of L_{brb}. Decreasing the dynamic amplification factor, R_{dv}, is possible however may be difficult, requiring significant modification to the existing pier.

(ii) Pier Leg Demands

Conservatively estimating the ultimate load on the pier legs is essential because they resist gravity loads of the bridge. The maximum base shear defined above imposes demands to the pier legs, however the pier legs must also resist gravity loads and additional dynamic demands. The demands to the impacting pier leg include a velocity upon impact followed by the transfer of gravitational and device forces vertically through the truss pier to the compressed leg (as shown in Figure 3). To conservatively estimate demands, the maximum response of each action individually is summed, thus assuming the dynamic effects to be in-phase. In the perspective of seismic retrofit, the buckling-restrained brace strength, $A_{brb}F_{ybrb}$, and the impact velocity, v_o, are the primary parameters influencing demands to the pier legs. Assuming that a value of A_{brb} is established during the design process to satisfy constraint (3i) or constraint (4), this constraint can be written in terms of a limiting impact velocity, v_o. The maximum allowable leg force, $P_{uL,allow}$, controlled by either the strength of the pier leg or foundation is arbitrarily taken here to equal 3w. Other limits may need to be defined to prevent foundation settlement and/or other serviceability requirements. Limiting v_o is typically achieved by increasing A_{brb} and decreasing L_{brb} (as seen in Figure 2) however increasing the allowable impact velocity of the pier leg, $v_{o,max}$, is most effectively done by decreasing A_{brb}. Methods to predict the maximum impact velocity have been proposed in Pollino (2004).

(4) Self-centering

The final constraint places an upper-bound on the buckling-restrained brace strength to ensure the self-centering ability of the system. Assuming the buckling-restrained brace's behavior to be elasto-plastic, its strength to simply equal $A_{brb}F_{ybrb}$ and ignoring any second order effects then limiting the local strength ratio to less than unity ($\eta_L<1$) will satisfy this constraint. Thus this constraint is independent of L_{brb}, as seen in Figure 2.

Design Solution Space Results

Results obtained from the graphical design procedure are shown in Figure 4 for aspect ratio of 4 and seismic demands characterized by a design spectrum, defined in NCHRP 12-49, with 1-second spectral accelerations (S_1) of 0.25g, 0.5g and 0.75g (with $S_s=2.5S_1$). Relevant pier properties for each aspect ratio, assumed to be representative of bridge steel truss piers, are also given in the figures. While parameters such as the existing pier stiffness and strength, among others, can be modified to provide the desired performance, ideally, these existing properties should remain unchanged to limit

the retrofit effort. However, in some cases, pier stiffening and/or strengthening may be required. The required strength and stiffness of the retrofitted pier to satisfy all constraints are expressed as a normalized quantity with respect to the existing pier strength (η_R/η_o) and stiffness (k_R/k_o). It is seen in Figure 4 that no strengthening or stiffening is required for h/d=4 to satisfy the constraints however the solution space shrinks as the seismic demand increases.

Design plots for an aspect ratio of 3 are shown in Figure 5. For larger seismic demands, the applicability of the retrofit strategy for a pier with an aspect ratio of 3 begins to diminish due to the required level of strengthening and stiffening. For an aspect ratio of 2, extensive strengthening and/or stiffening would be required for the pier properties and demands considered here.

Thus it becomes clearer that using the base overturning moment as the force limiting mechanism requires relatively slender piers in order to provide an efficient retrofit using this method. More squat piers require significant strength and stiffness to resist demands including dynamic effects and may experience only a few excursions beyond the point of uplift, forcing the pier to resist and dissipate seismic energy in a mostly elastic manner.

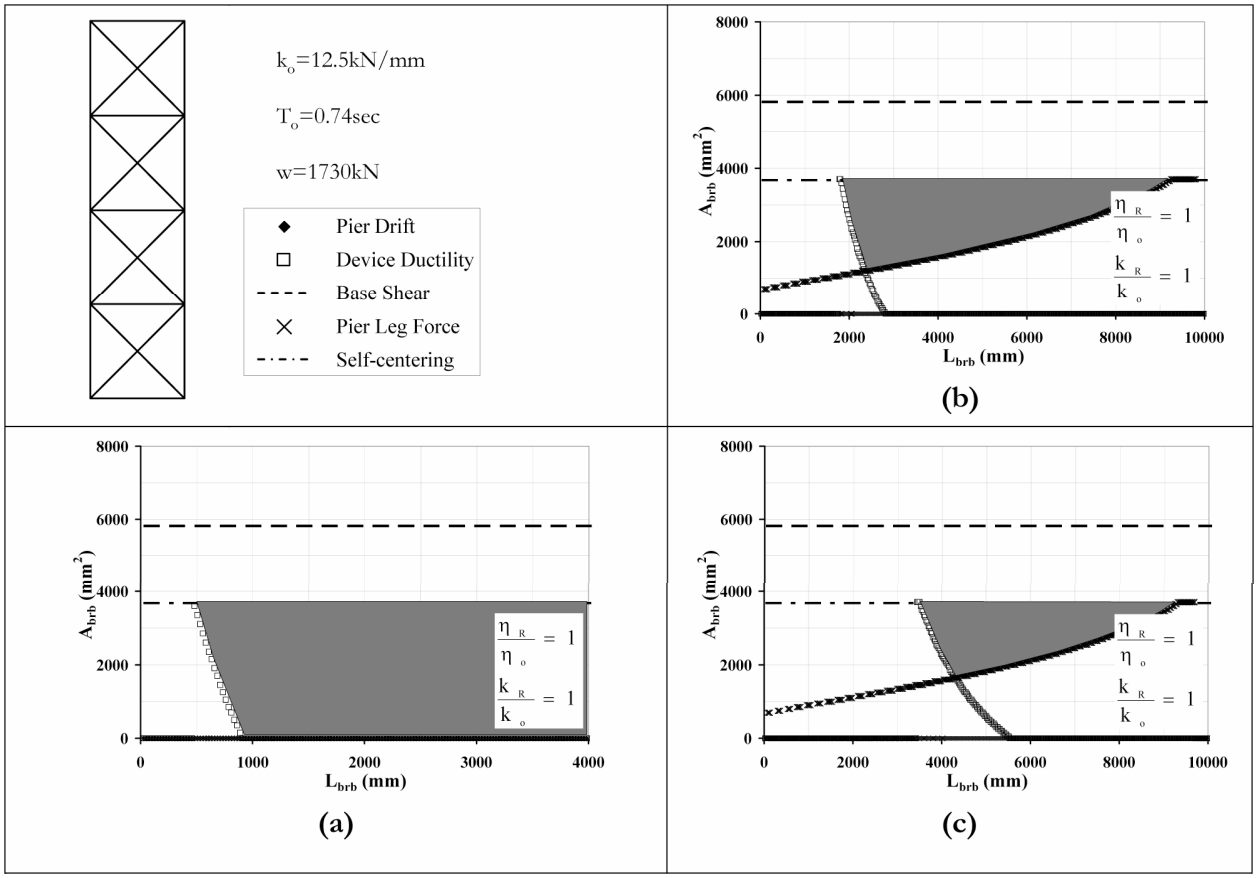

Figure 4. Design solution spaces for h/d=4 (a) S_1=0.25g, (b) S_1=0.5g, and (c) S_1=0.75g

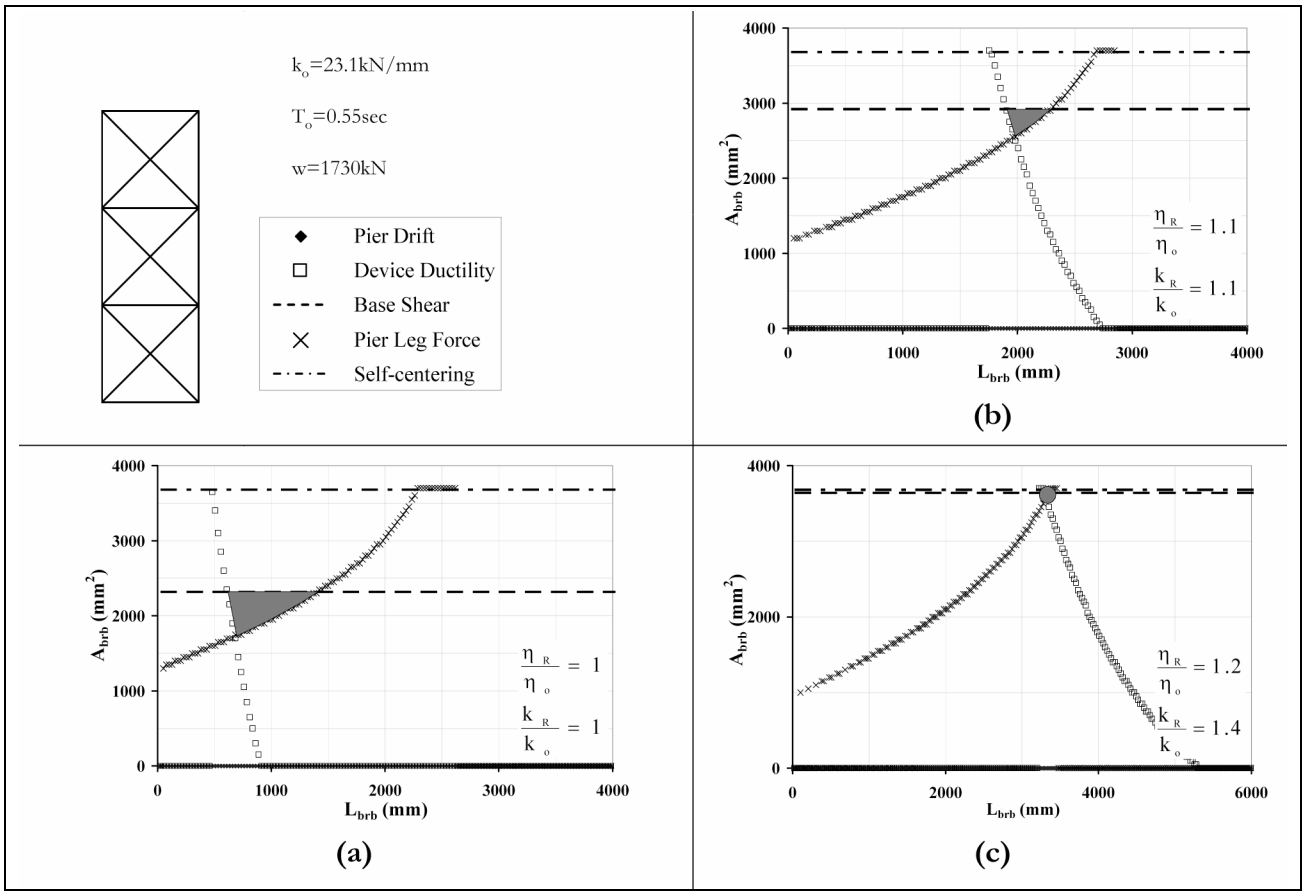

Figure 5. Design solution spaces for h/d=3 (a) S_1=0.25g, (b) S_1=0.5g, and (c) S_1=0.75g

Conclusions

The complex behavior of a proposed controlled rocking system requires the use of a number of design constraints to control the dynamic response of the system to within the established limits. The performance based, graphical design approach is able to take into account each constraint with respect to key design parameters providing a design tool that can effectively guide the design toward a satisfactory solution.

Future Research

Future research plans include investigating the effects of vertical, soft soil and near-field ground motions on the seismic performance of the controlled rocking system. Also, the effects of bi-directional ground motions on the response of 4-legged piers are to be investigated. The use of other types of passive energy dissipation devices could also be explored. Finally, dynamic experimental testing of a controlled rocking pier is expected in the near future, using three components of excitation.

Acknowledgements

This research was carried out under the supervision of Dr. Michel Bruneau and was supported in part by the Federal Highway Administration under contract number DTFH61-98-C-00094 to the Multidisciplinary Center for Earthquake Engineering Research. However, any opinions, findings,

conclusions, and recommendations presented in this paper are those of the author and do not necessarily reflect the views of the sponsors.

References

ATC/MCEER (2003): *NCHRP 12-49 Recommended LRFD Guidelines for the Seismic Design of Highway Bridges, Part I: Specifications*. ATC/MCEER Joint Venture.

Iwata M, Kato T, Wada A (2000): Buckling-restrained braces as hysteretic dampers. *Behavior of Steel Structures in Seismic Areas, STESSA 2000*, pp. 33-38.

Lee K, Bruneau M (2004): Seismic Vulnerability Evaluation of Axially Loaded Steel Built-Up Laced Members. *Technical Report MCEER-04-0007*, Multidisciplinary Center for Earthquake Engineering Research, The State University of New York at Buffalo, Buffalo, NY.

Pollino M, Bruneau M (2004): Seismic Retrofit of Bridge Steel Truss Piers Using a Controlled Rocking Approach: Hysteretic Behavior and Analysis Methods. *J. Struct. Eng.*, (submitted for review, Feb. 2004).

Pollino M (2004): Seismic Retrofit of Bridge Steel Truss Piers Using a Controlled Rocking Approach. *MS Thesis*, The State University of New York at Buffalo, Buffalo, NY.

Ritchie P, Kauhl N, Kulicki J (1999): Critical Seismic Issues for Existing Steel Bridges. *Technical Report MCEER-99-0013*, Multidisciplinary Center for Earthquake Engineering Research, The State University of New York at Buffalo, Buffalo, NY.

Sarraf M, Bruneau M (1998). Ductile Seismic Retrofit of Steel Deck-Truss Bridges. II: Design Applications. *J. Struct. Eng.*, ASCE, Vol. 124, No. 11, pp. 1263-1271.

Production Staff

- Jane E. Stoyle, Managing Editor
- Michelle A. Zuppa, Layout and Design
- David Pierro, Graphics and Cover Design

Cover Images

Cover Images (from top left, then clockwise): Group photo taken at the 2005 MCEER Student Leadership Council retreat in Tallahassee, Florida; two graphs, (top) showing general pushover curve for effective stiffness and period and (bottom) showing schematic representation of inertial, viscous and metallic damper forces from Ramiro Vargas' winning paper, "Seismic Response of Hybrid Systems with Metallic and Viscous Dampers," along with a photo of Ramiro presenting his research at the 2004 MCEER Site Review; photo of the University at Buffalo's Structural Engineering and Earthquake Simulation Laboratory (SEESL) with testing areas labeled; photo from the 2005 MCEER Field Mission to Greece showing three columns standing from ancient times (right) and two recently reconstructed columns at Nemea; group photo of MCEER 2005 Field Mission participants, showing (left to right) Marlon Hill, Daniel Fenz, Swagata Banerjee and Michael Pollino, at the shake table facilities of the National Technical University in Athens; graphic showing ideal responses of elasto-plastic and self-centering systems from Dong Wang's honorable mention paper, "Seimsic Response of Steel Framed Hospital Buildings with Self-Centering Systems;" graphic showing vibro-stone columns with or without wick drains from Thevachandran Shenthan's honorable mention paper "Soil Densification Using Vibro-Stone Columns Supplemented with Wick Drains;" photo of a small bearing testing machine from Daniel Fenz's paper, "The Double Concave Friction Pendulum Bearing;" and figure showing evaluation of limit rotation from Jeffrey Berman's paper "Finite Element Parametric Study of Hybrid Rectangular Links for Eccentrically Braced Frames."

Acknowledgements

This work was supported primarily by the Earthquake Engineering Research Centers Program of the National Science Foundation under NSF Award Number EEC-9701471.

Any opinions, findings and conclusions or recommendations expressed in this material are those of the author(s) and do not necessarily reflect those of the National Science Foundation.

MULTIDISCIPLINARY CENTER FOR EARTHQUAKE ENGINEERING RESEARCH

A National Center of Excellence in Advanced Technology Applications

University at Buffalo, State University of New York
Red Jacket Quadrangle ■ Buffalo, New York 14261
Phone: (716) 645-3391 ■ Fax: (716) 645-3399
E-mail: *mceer@mceermail.buffalo.edu* ■ WWW Site *http://mceer.buffalo.edu*

University at Buffalo *The State University of New York*